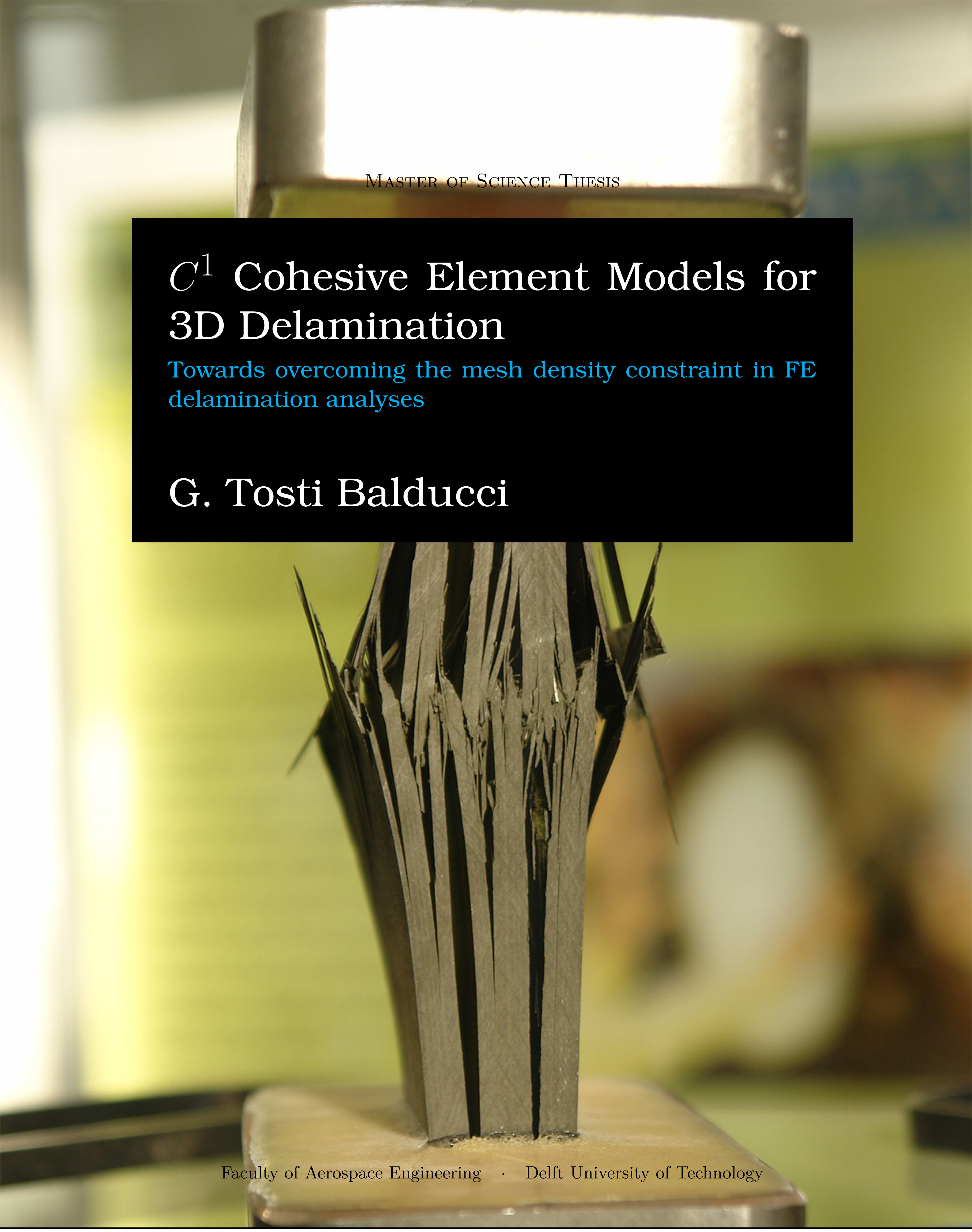

MASTER OF SCIENCE THESIS

C^1 Cohesive Element Models for 3D Delamination

Towards overcoming the mesh density constraint in FE delamination analyses

G. Tosti Balducci

Faculty of Aerospace Engineering · Delft University of Technology

C^1 Cohesive Element Models for 3D Delamination

Towards overcoming the mesh density constraint in FE delamination analyses

MASTER OF SCIENCE THESIS

For obtaining the degree of Master of Science in Aerospace Engineering
at Delft University of Technology

G. Tosti Balducci

24/05/2019

Faculty of Aerospace Engineering · Delft University of Technology

Delft University of Technology
Faculty of Aerospace Engineering
Department of Aerospace Structures and Materials

GRADUATION COMMITTEE

Dated: 24/05/2019

Chair holder:

Prof. Dr. C. Kassapoglou

Committee members:

Dr. B. Chen

Prof. Dr. C. Kassapoglou

Dr. D. Zarouchas

Abstract

The wide adoption of composite structures in the aerospace industry asks for reliable numerical methods to account for the effects of damage, among which delamination. Cohesive elements (CEs) are a versatile and physically representative way of reproducing delamination, but, using their standard form, at least 3 elements are required in the narrow cohesive zone, hindering the applicability in practical scenarios. This limitation is due to the inability of current models to capture the deformation of the delaminating substrates. The present work focuses on the implementation and testing of triangular thin plate substrate elements and compatible cohesive elements, which satisfy C^1-continuity at their boundary. The improved regularity meets the continuity requirement coming from the Kirchhoff Plate Theory and the triangular shape allows for conformity to complex geometries. After verification of plate and cohesive element singularly, the overall model is validated for mode I delamination. Very accurate predictions of the limit load and crack propagation phase are found, using CEs as large as 11 times the cohesive zone.

Table of Contents

List of Figures

List of Tables

Foreword

The computer and its incredible power are the curse and blessing of the 21^{st} century engineer. The once unachievable has been achieved. Incredibly complex phenomena, ranging from a full scale plane crash to an earthquake, can be now reproduced (safely) and studied from an office desk, having incredible levels of detail. Also, software for numerical analyses is nowadays user-friendly, offering colorful interfaces and tons of tools accessible with a click of the mouse. One could literally train a 10 years old kid to run a moderately complex simulation. So is there still room left for engineering in this triumph of parallel processing and scenographic output? Well, there should be.

Finite element analyses much too often are used to justify a blind approach to solving structural problems. Going back to the origins of the finite element method, however, this was devised by engineers, scientists and theoreticians with immense knowledge of mathematics and of structural theories. The framework they set up is a beautiful theory in numerical analysis that can be written down on paper. The milestones in FEM were reached not by adding more elements to a grid, but thinking to the deformation of the structure and translating it in formulas which would then shape the theory. This is what Boyang, Raffaele and me tried to remember when looking at mesh density constraint of cohesive elements.

I thank Boyang Chen for being the best supervisor I could wish for. He always treated me like a peer and kept my opinion in the highest regard. I indeed felt this thesis not like my final ordeal as a student, but as an amazing collaboration with him, in which we both shared curiosity, excitement and, at times, a tad of frustration. I also would like to thank Raffaele Russo, as a friend and as a ‘technical consultant’, who had been through most of my same struggles before and gave my priceless advice on FORTRAN, Abaqus and the subtleties of delamination.

I dedicate this thesis to my parents, Alessandra and Massimo as I bothered them so much with it that they probably know it better than I do. I thank both of them immensely for giving me their unconditional trust and for supporting me morally (not to mention financially) in every decision I’ve made so far.

I cannot look back to my university years, without thinking to all the people who have been alongside me, head bent on their books or laptops and praying for the next exam session or for their simulations not to crash. Back to my bachelor in Milan, I want to thank Andrea, Angelo, Francesco, Jacopo and Michele, who made a great team in the years of Politecnico. Here in Delft, I would like to thank the colleagues and friends of the office in the ASCM depatment, Evgenios, Lander, Nicolas, Steven, Tara, Tom, Vanessa and Vlad for engaging in interesting conversation, at times also serious and for being such a great support group for all the headaches in our thesis projects.

Although I didn't share the pains and glories of a study room with them, thinking back to my student years will always remember me of my housemates in Milan, Luca, Nicola e Stefano, my friends from 'Il Teatro delle Biglie', the Roman crew, Flavia, Valentina, Veronica and Valerio and my climbing circle with Philipp and Sergio. Special mentions go dutifully to the friends in my homeland, 'la Maremma' and in particular Mr. Lee, Mr. T, Mastro, Noemi and Rocco, to La Tata e Andrea, who have been almost like second parents to me, to Alessandro Alterio, who introduced me to the marvels of mathematics and to my dog and cat, Ruffo and Emma, who never failed in cheering me up.

Delft, University of Technology G. Tosti Balducci
24/05/2019

“Simplicity is the ultimate sophistication”
— *Leonardo da Vinci*

Chapter 1

Introduction

Context and Motivation

Composite materials constitute the current paradigm for efficient structural solutions. Their anisotropic architecture can guarantee an optimal distribution of strength and stiffness properties, while ensuring low weight of the final product. The laminated layout of composite structures allows for versatility in tuning the mechanical properties, but inevitably introduces weak interfaces between adjacent layers or *plies*, known as *resin rich regions*. Whenever the out-of-plane or transverse shear stresses exceed the material strength at these locations, a *delamination* forms, which can grow upon further loading and eventually lead to structural failure. Delamination is only one of the possible damage mechanisms in composite laminates, but it manifests in a large number of circumstances (Figure 1.1), indicating the need for reliable techniques to predict this failure mode.

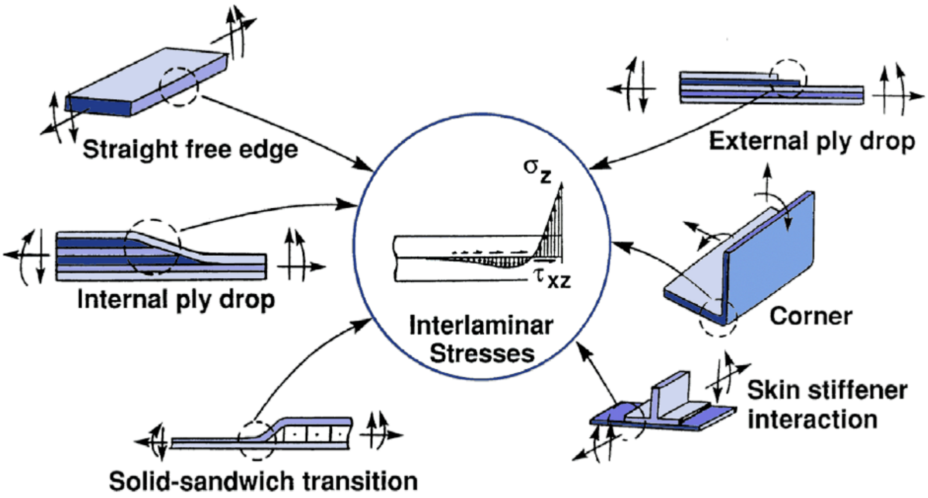

Figure 1.1: Examples of delamination-critical regions [1].

Although analytical solutions can be used during preliminary design when it is customary to make simplifying assumptions, numerical methods become necessary for accurately capturing the structural deformation. The dominant practice in computational mechanics is to perform a *Finite Element* (FE) analysis to study complex structural behaviours. In this context, *cohesive elements* (CEs) can be used in the numerical model to study the interface degradation.

The ability of cohesive elements to predict crack onset and propagation for both ductile and brittle materials has made them an appealing tool in delamination analysis. However this technology is prevented from the adoption in the industrial practice due to a stringent mesh density requirement. A minimum number of elements, ranging in literature from 3 to 10 [2–6] is in fact needed in the so-called *cohesive zone*, which generally extends ahead of the crack tip for few millimeters, if not tenths of millimeters. This requirement, known as the *mesh density constraint* (MDC), arises from the inability of standard CEs to reproduce the steep stress gradients in the cohesive zone, except when extremely small elements are used.

Research Objective and Questions

Damage and stresses at the interface are determined by its opening during delamination. A finite element model must then be able to reproduce accurately the deformation of the sublaminates if fracture onset and progression are to be predicted. The delaminating parts of a composite usually show small ratios between thickness and planar dimensions, thus the Kirchhoff Plate Theory can provide a meaningful description of their deformation. The aim of the present research is to implement a thin plate element, satisfying the C^1-continuity requirement proper of the Kirchhoff model, along with a compatible cohesive element. Their use in delamination FE analyses will show if the mesh density constraint has in fact been alleviated. Also, the two elements will be required to have triangular support, since this can conform to complex geometries, object of possible future studies.

The research objective for this work can be formally stated as follows:

The objective of the research is to assess the mesh density constraint, as well as the accuracy and computational performances proper of a C^1 triangular plate element and its compatible cohesive element, by implementing them as user subroutines for a commercial FE platform and by testing them in delamination FE analyses

To achieve this goal, a set of research questions is formulated, which will find their answers at different stages of the report.

1. What is a suitable triangular thin plate element which ensures a C^1 displacement field?
2. What is the formulation of a cohesive element compatible with the plate element developed and able to capture pure-mode delamination?
3. Is the implementation of the above elements correct and what series of tests can assess this?
4. Is the final model accurate and does it improve in terms of mesh size and CPU times, when compared to the current standard in delamination modeling?

Report Structure

The contents of this report are organized as follows. Chapter 2 presents the formulation of the standard CE, discusses the mesh density constraint and the state-of-the-art in terms of strategies adopted to overcome it. Chapter 3 goes through the implementation of the C^1 triangular plate element and associated cohesive element, which are both verified in Chapter 4. Chapter 5 means to answer to the core research question, validating the proposed model against a benchmark delamination problem. Finally, Chapter 6 summarizes the work performed, draws conclusions based on the results obtained and discusses possible future developments.

Chapter 2

Cohesive Elements and the Mesh Density Constraint

The present chapter provides the theoretical background to correctly frame and understand the novelty of this research. Following a general-to-detail approach, the two main theories in fracture mechanics to model delamination are presented, along with the numerical methods that derive from them. Afterwards, the cohesive element is introduced by description of its kinematics and constitutive law, followed by a discussion on the essence and the origins of the mesh density constraint. Finally, the state-of-the-art solutions to the MDC are outlined and classified based on the regularity of the proposed solution field, which is the discriminant investigated in this work.

2.1 LEFM and CZM

The two main groups of numerical methods in fracture mechanics are based on the theories of *Linear Elastic Fracture Mechanics* (LEFM) and *Cohesive Zone Modelling* (CZM).

2.1.1 Linear Elastic Fracture Mechanics and VCCT

Linear Elastic Fracture Mechanics is based on the theory developed by Griffith in the 1920's [7] to predict fracture in brittle media. The central idea of LEFM is that crack propagation occurs as soon as the energy release rate, namely the elastic energy required to extend the crack of a unit area, reaches the fracture toughness of the material in one of the three failure modes (Figure 2.1). The propagation condition for LEFM is then

$$G = G_c \tag{2.1}$$

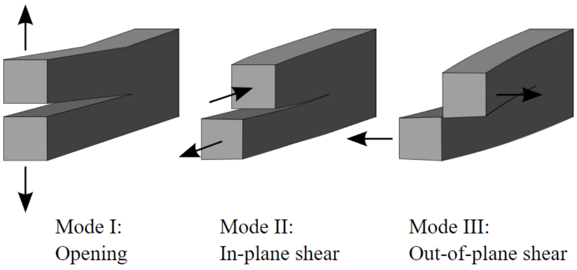

Figure 2.1: Fracture opening modes.

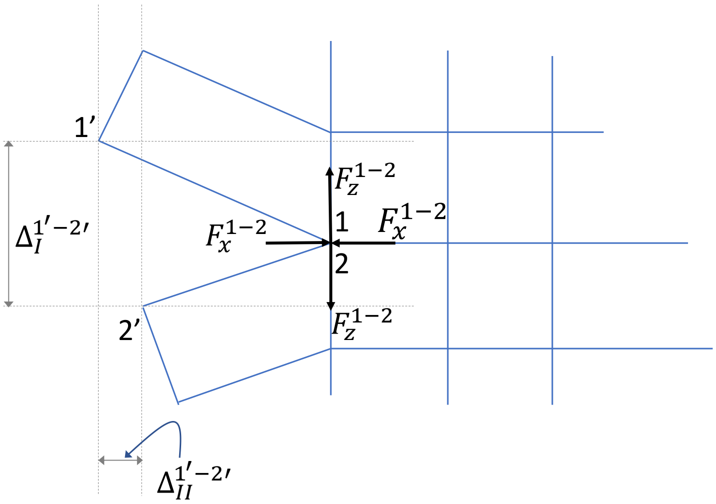

Figure 2.2: Forces and openings in 2D VCCT.

According to pure LEFM, a solid is in its linear elastic field until the crack propagates. Irwin [8] extended the theory to account for the presence of a plastic region ahead of the crack tip. In all cases where the plastic region is much smaller than the structural dimensions and crack length, the plastic energy dissipation can be added to the energy balance in Equation (2.1) and LEFM would still accurately predict the crack propagation.

Whenever LEFM is applicable, it is reasonable to assume that the work required to extend the crack of a given area is the same as that needed to close it by the same area. The latter is the pivotal assumption of the *Virtual Crack Closure Technique* (VCCT), that is the finite element implementation of LEFM. In the form suggested by Rybicki and Kanninen [9], VCCT makes the additional assumption that the crack propagates in a self-similar manner. Therefore at each increment of a FE analysis, the energy release rate is computed by multiplying the separations of the nodes immediately ahead of the crack tip and the nodal forces at the crack tip, as shown in Figure 2.2. It follows that the crack advances of an element length, as soon as, for openings in mode I and II respectively,

$$\begin{aligned} G_I &= \frac{1}{2b\,\mathrm{d}a} F_z^{1-2}\,\Delta_I^{1'-2'} = G_{I,c} \\ G_{II} &= \frac{1}{2b\,\mathrm{d}a} F_x^{1-2}\,\Delta_{II}^{1'-2'} = G_{II,c} \end{aligned} \tag{2.2}$$

Figure 2.3: Separated-to-intact transition for delaminated composite specimen [10]. Fibers bridging opposite surfaces are observed approaching the crack tip.

where da is the crack increment, b is the width of the plate, F^{1-2} is the force exchanged either in the x or z direction between nodes 1 and 2, which still have to separate. $\Delta^{1'-2'}$ refers to the opening between the nodes ahead of the crack tip.

2.1.2 Cohesive Zone Modelling and CEs

LEFM is a straightforward model of fracture but it comes with the physical paradox of infinite stresses at the crack tip. Introducing a plastic region, where the material is under yield stress, Irwin's theory managed to remove this inconsistency. A different theory, known as Cohesive Zone Modelling, was proposed by Dugdale and Barenblatt [11,12] still with the intention to remove the stress singularity at the crack tip. These authors suggested that the stresses are null at the crack tip and that they progressively develop in a region of partially damaged material, known as the cohesive zone. A physical manifestation of this transition region can be seen when fibers of delaminating plies bridge opposite crack surfaces, such as in Figure 2.3. Fiber bridging is a complex phenomenon, that has not been modelled in this work, however it is illustrative of the cohesive zone concept.

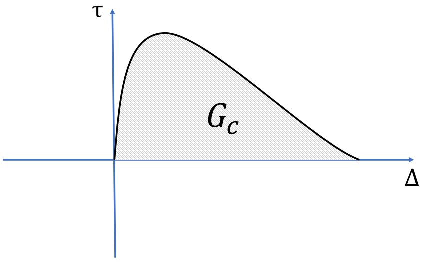

Figure 2.4: Generic cohesive law.

Cohesive zone modeling is traditionally implemented in a FE context through elements placed along the fracture path, known as cohesive elements, that will be the focus of Section 2.2. The characterization of a cohesive element consists of its kinematics, which describes the openings and to esabilish a constitutive relation, which links openings and stresses in the three loading modes. The shape of the constitutive relation is given by a *cohesive law* (CL), generically represented in Figure 2.4, while a damage onset and a damage evolution criteria determine the limit and failure opening.

2.1.3 Differences between VCCT and CEs

Although VCCT has been lately extended to allow for multiple nodal releases and to model crack onset (*Enhanced VCCT* in [13]), CEs still remain a more general and physically representative approach to crack propagation modeling. This is understood, considering the following differences between these two techniques.

1. VCCT requires an *a-priori* knowledge of the crack path, whereas cohesive elements can be placed at all the required element interfaces to allow for crack branching in generic directions.
2. Crack propagation in VCCT occurs through one or multiple nodal releases. In case of relevant mesh sizes, the overall stiffness loss per-release can be large, leading to numerical oscillations around the equilibrium path.
3. VCCT is based on the assumption of self-similar crack propagation. In a 3D space, where the interface is represented by a surface, this assumption constraints the crack front to be straight throughout the entire propagation. Self-similarity of crack propagation does not usually occur in practice and it is not a fundamental assumption of CE models.
4. VCCT is based on pure LEFM and therefore can predict fracture accurately only for brittle materials. On the other hand, CZM introduces the presence of a process zone and allows CEs to model also large degrees of ductility during cracking.
5. If the constitutive relation of CEs is defined by a stress-strain tensor, instead of a traction-separation law, this technique can also model adhesives of finite thickness. This is not the case for VCCT, since this method does not account for the deformation of the interface.

2.2 Cohesive Elements

As any other finite element, a cohesive element is defined by its stiffness matrix and residual vector. The expressions of these arrays are derived directly from the the element's kinematics and constitutive relation.

The following discussion introduces the standard cohesive element as devised by Camanho *et al.* [3, 4], represented in Figure 2.5 with its nodes and connectivity. The matrices expressing the kinematics and constitutive law are outlined and finally built into the element's stiffness matrix and residual vector. The same process is followed in Chapter 3 to characterize the CE proposed in this work.

2.2.1 Kinematics

The kinematics of a cohesive element is the relation between the openings $\boldsymbol{\Delta}$ and the nodal degrees of freedom (DOFs) $\boldsymbol{U}$. To express the CE openings, the displacements of the element's bottom and top surfaces (respectively nodes 1 to 4 and 5 to 8 in Figure 2.5) have to be

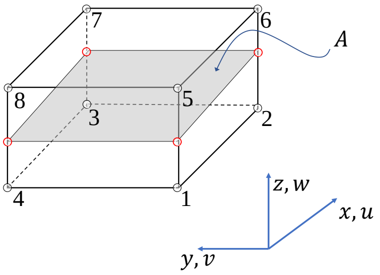

Figure 2.5: Standard 3D CE: scheme.

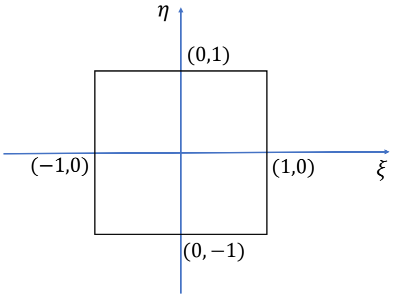

Figure 2.6: Standard 3D CE: parent domain.

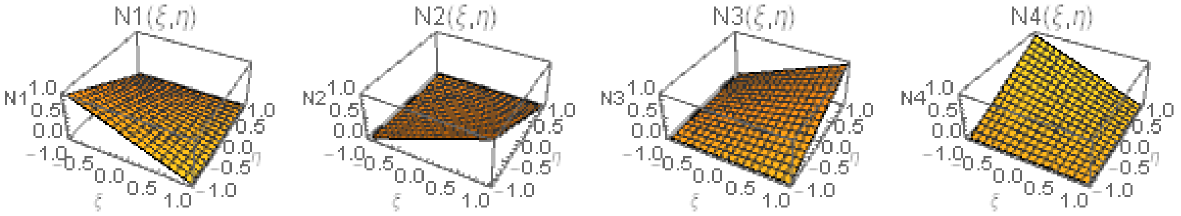

Figure 2.7: Bilinear shape functions in the parent domain Ξ.

defined. The components of $\mathbf{\Delta}$ along the three loading modes are defined for every point $\boldsymbol{x} = (x(\xi,\eta), y(\xi,\eta))$ of the mid-surface A (grey-coloured in figure) and read

$$\mathbf{\Delta} = \begin{bmatrix} \Delta_{II} \\ \Delta_{III} \\ \Delta_{I} \end{bmatrix} = \begin{bmatrix} -u^{btm}(\boldsymbol{x}(\xi,\eta)) + u^{top}(\boldsymbol{x}(\xi,\eta)) \\ -v^{btm}(\boldsymbol{x}(\xi,\eta)) + v^{top}(\boldsymbol{x}(\xi,\eta)) \\ -w^{btm}(\boldsymbol{x}(\xi,\eta)) + w^{top}(\boldsymbol{x}(\xi,\eta)) \end{bmatrix} \tag{2.3}$$

The mid-surface of a cohesive element in the Cartesian space is generally mapped to a reference domain of coordinates ξ and η, also called the *parent domain*, taken as the unit square (Figure 2.6):

$$\Xi = \{(\xi,\eta) \in [-1,1] \times [-1,1]\} \tag{2.4}$$

In its standard version, the initially overlapping upper and lower faces of the CE displace compatibly with continuum elements that are interpolated linearly. The shape functions are then bilinear in the 2D parent domain, as shown in Figure 2.7 and read

$$N_1(\xi,\eta) = \frac{1}{4}(1-\xi)(1-\eta) \tag{2.5}$$

$$N_2(\xi,\eta) = \frac{1}{4}(1+\xi)(1-\eta) \tag{2.6}$$

$$N_3(\xi,\eta) = \frac{1}{4}(1+\xi)(1+\eta) \tag{2.7}$$

$$N_4(\xi,\eta) = \frac{1}{4}(1-\xi)(1+\eta) \tag{2.8}$$

The displacements of both faces of the CE can be written isolating the degrees of freedom as

$$u(\xi,\eta) = [N_1(\xi,\eta)\ N_2(\xi,\eta)\ N_3(\xi,\eta)\ N_4(\xi,\eta)]\boldsymbol{u} = \boldsymbol{N}^T\boldsymbol{u} \tag{2.9}$$

$$v(\xi,\eta) = [N_1(\xi,\eta)\ N_2(\xi,\eta)\ N_3(\xi,\eta)\ N_4(\xi,\eta)]\boldsymbol{v} = \boldsymbol{N}^T\boldsymbol{v} \tag{2.10}$$

$$w(\xi,\eta) = [N_1(\xi,\eta)\ N_2(\xi,\eta)\ N_3(\xi,\eta)\ N_4(\xi,\eta)]\boldsymbol{w} = \boldsymbol{N}^T\boldsymbol{w} \tag{2.11}$$

where $\boldsymbol{u}$, $\boldsymbol{v}$, $\boldsymbol{w}$ are the nodal displacements in respectively the x, y and z directions:

$$\boldsymbol{u}^T = [u_1\ u_2\ u_3\ u_4] \tag{2.12}$$

$$\boldsymbol{v}^T = [v_1\ v_2\ v_3\ v_4] \tag{2.13}$$

$$\boldsymbol{w}^T = [w_1\ w_2\ w_3\ w_4] \tag{2.14}$$

From Equations (2.12) to (2.14) the DOFs vector of the cohesive element can be built as

$$\boldsymbol{U}^T = [\, -u_1^{btm}\ \ -v_1^{btm}\ \ -w_1^{btm}\ \ \ldots\ -u_4^{btm}\ \ -v_4^{btm}\ \ -w_4^{btm}\ \ u_1^{top}\ v_1^{top}\ w_1^{top}\ \ \ldots\ u_4^{top}\ v_4^{top}\ w_4^{top}\,]$$

The degrees of freedom with the ‘btm’ superscript refer to nodes 1 to 4 in Figure 2.5, while the ‘top’ DOFs belong to nodes 5 to 8.

The above definitions can be used to finally express the openings in terms of the CE’s nodal displacements as

$$\boldsymbol{\Delta} = \boldsymbol{B}^T\boldsymbol{U} \tag{2.15}$$

where the $\boldsymbol{B}$ matrix is

$$\boldsymbol{B}^T = \begin{bmatrix} -N_1 & 0 & 0\ldots-N_4 & 0 & 0 & N_1 & 0 & 0\ldots N_4 & 0 & 0 \\ 0 & -N_1 & 0\ldots0 & -N_4 & 0 & 0 & N_1 & 0\ldots0 & N_4 & 0 \\ 0 & 0 & -N_1\ldots0 & 0 & -N_4 & 0 & 0 & N_1\ldots0 & 0 & N_4 \end{bmatrix}$$

The above is the final expression of the CE’s $\boldsymbol{B}$-matrix only if geometrical non-linearities are neglected, hence when no changes in configuration are accounted for.

2.2.2 Constitutive relation

The constitutive relation of a cohesive element, or, equivalently, its cohesive law, links stresses $\boldsymbol{\tau}$ and openings $\boldsymbol{\Delta}$ for each of the three fracture modes. In finite element terms, this relation is what defines the constitutive matrix $\boldsymbol{D}$, such that

$$\boldsymbol{\tau} = \boldsymbol{D}\boldsymbol{\Delta}$$

The literature abounds of cohesive law models, each requiring a different number of parameters. Two-parameters cohesive relations are, for example, those of Xu-Needleman [14] and Camacho-Ortiz [15], who proposed respectively an exponential and linear CL. Tvergaard *et al.* [16] formulated instead a 5-parameter trapezodial CL, from degeneration of which, the well-known 3-parameters bilinear model is derived, as discussed in [17].

Different studies investigated the effect of the CL shape on various quantities, such as the crack initiation load, the shape of the crack front and the extent of the cohesive and plastic

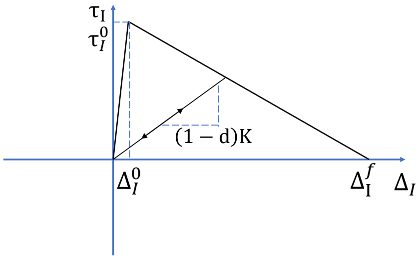

Figure 2.8: Bilinear CL, mode I.

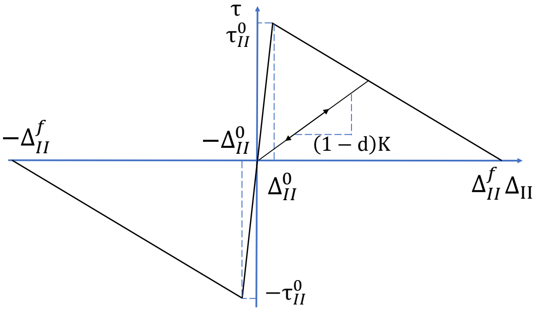

Figure 2.9: Bilinear CL, shear modes.

regions. In particular, Shet and Chandra [18] compared the three mostly used models, meaning the exponential, bilinear and trapezoidal ones and noticed that the parameters shaping the different CL curves indeed affect how the energy is redistributed between plastic and cohesive fracture dissipation. However, Yang and Cox [5], among others, confirmed that when the process zone is small compared to the crack size, LEFM accurately describes the fracture process, regardless of the CL shape.

The bilinear cohesive law (Figures 2.8 and 2.9) was used in the work at hand to model the CE's constitutive response. This choice was made to keep the same constitutive law used in Abaqus CZM implementations, which were taken as the standard during validation of the proposed method. A sensitivity study on the CL shape was not in the scope of this research, since for the test-case considered in Chapter 5 and generally for composite panels with large initial cracks, the effect of the process zone can be overlooked.

Linear response

The first trait of the cohesive law is linear and its slope is given by the so-called *penalty stiffness* K. This parameter has no direct physical meaning and it is introduced to avoid sudden material damaging for extremely small openings. The value of K has to be high enough not to introduce a large compliance in the system before material degradation, but also small enough to avoid sudden stiffness drops at every extension of the crack front.

In compliance with the above requirements, Turòn *et al.* [19] suggested the following relation

$$K = 50\,\frac{E_3}{t} \tag{2.16}$$

where E_3 is the out-of-plane material modulus of the lamina and t is the thickness of the laminate.

The same research group also noticed in [20] that differentiating between the penalty stiffnesses in mode I and shear modes could ensure the thermodynamical validity of the constitutive model. In particular, they demonstrated that a positive energy dissipation is granted, if

$$\frac{K_{sh}}{K_I} = \frac{G_{I,c}}{G_{II,c}}\left(\frac{\tau_{sh}^0}{\tau_I^0}\right)^2 \tag{2.17}$$

where K_{sh} and K_I indicate the shear and mode I penalty stiffnesses and K_I can be taken equal to K in Equation (2.16). $\tau^0_{sh} = \tau^0_{II} = \tau^0_{III}$ is the material shear strength, while τ^0_I is the strength in mode I.

Also, instead of keeping two separate penalty stiffnesses, Turòn *et al.* [21] recently suggested a unique mode-dependent expression of K. Defining the mode-mixity ratio B as

$$B = \frac{G_{II} + G_{III}}{G_I + G_{II} + G_{III}} \tag{2.18}$$

where G_I, G_{II} and G_{III} are the energy release rates in the three modal directions, the overall K can be given as a weighted average of K_I and K_{sh}, hence

$$K = K_I\,(1 - B) + B\,K_{sh} \tag{2.19}$$

Damage

In case of isotropic damage, where the same degradation is applied in all directions, reduction of the material pristine stiffness is defined by a scalar, known as the *damage variable*.

In [22], Turòn *et al.* proposed a damage model accounting for mixed-mode loading and able to ensure a monotonically increasing damage variable. This constitutive model represents a standard in the computational CZM literature and it is briefly outlined here to derive the expression of the damage variable for the bilinear cohesive law.

Firstly, a general definition of the interface opening is necessary. In mixed mode loading, the opening is defined as the vector norm of its pure mode components, such that

$$\Delta_m = \sqrt{\langle \Delta_I^2 \rangle + \Delta_{shear}^2} \tag{2.20}$$

where $\langle - \rangle$ are the MacAulay brackets, defined as

$$\langle x \rangle = \begin{cases} x & \text{if } x > 0 \\ 0 & \text{if } x \leq 0 \end{cases} \tag{2.21}$$

The shear opening Δ_{shear} accounts for the both modes II and III separations and it is expressed as

$$\Delta_{shear} = \sqrt{\Delta_{II}^2 + \Delta_{III}^2} \tag{2.22}$$

A constitutive damage model needs to include the conditions for damage propagation and onset. Propagation, hence an increase in crack surface, occurs as soon as

$$G = G_c \tag{2.23}$$

In mixed-mode delamination, the energy release rate G is obtained from its contributions in the three modal directions, thus

$$G = G_I + G_{II} = G_{III} = G_I + G_{shear} \tag{2.24}$$

The critical energy release rate G_c also depends on the mode mixity and can be defined by means of the Benzeggagh-Kenane criterion (B-K) [23] as

$$G_c = G_{I,c} + (G_{II,c} - G_{I,c}) \left(\frac{G_{shear}}{G} \right)^{\eta} \tag{2.25}$$

where η is a material parameter found by curve-fitting of experimental data.

If G_I and G_{shear} are expressed using the the bilinear cohesive law, Equations (2.23) to (2.25) allow to write the failure opening as

$$\Delta^f = \frac{\Delta_I^0 \Delta_I^f + (\Delta_{shear}^0 \Delta_{shear}^f - \Delta_I^0 \Delta_I^f) B^{\eta}}{\Delta^0} \tag{2.26}$$

where B was defined in Equation (2.18) The terms Δ_I^0, Δ_I^f in Equation (2.26) are the onset and failure opening for pure mode I and Δ_{shear}^0, Δ_{shear}^f are the shear modes equivalents. These quantities are found from the bilinear cohesive law in the pure mode directions as

$$\Delta_I^0 = \frac{\tau_I^0}{K} \tag{2.27}$$

$$\Delta_I^f = \frac{2G_{I,c}}{\tau_I^0} \tag{2.28}$$

$$\Delta_{shear}^0 = \frac{\tau_{II}^0}{K} \tag{2.29}$$

$$\Delta_{shear}^f = \frac{2G_{II,c}}{\tau_{II}^0} \tag{2.30}$$

Still to be determined is the mixed-mode limit opening Δ^0, found choosing a damage onset criterion. Usually, this has been proposed in literature as separated from the propagation condition. However, Turòn *et al.* noticed that a change in mode-mixity during delamination may lead to a spurious recovery of the intact damage state, if the two criteria for damage propagation and onset are inconsistent with each other. Therefore the authors defined damage initiation starting from the B-K equation in the limit case of $d = 0$, obtaining

$$(\Delta^0)^2 = (\Delta_I^0)^2 + \left[(\Delta_{shear}^0)^2 - (\Delta_I^0)^2 \right] B^{\eta} \tag{2.31}$$

Using the quantities just outlined, the damage variable for the bilinear cohesive law is finally

$$d = \begin{cases} 0 & \text{if } \Delta_m < \Delta^0 \\ \frac{\Delta^f(\Delta_m - \Delta^0)}{\Delta_m(\Delta^f - \Delta^0)} & \text{if } \Delta^0 \leq \Delta_m < \Delta^f \\ 1 & \text{if } \Delta_m \geq \Delta^f \end{cases} \tag{2.32}$$

where the three conditions of intact, partially damaged and failed material are distinguished, depending on the mixed-mode opening.

At every iteration of a non-linear FE analysis, Δ_m, Δ^f and Δ^0 are computed depending on B and d is updated only if the value obtained with Equation (2.32) is higher than the one at the previous load increment.

2.2.3 Constitutive matrix

The updated damage variable is used to compute the $\boldsymbol{D}$-matrix of the CE as follows

$$\boldsymbol{D} = \begin{bmatrix} (1-d_I)K & 0 & 0 \\ 0 & (1-d)K & 0 \\ 0 & 0 & (1-d)K \end{bmatrix} \tag{2.33}$$

The constitutive matrix in Equation (2.33) is diagonal, thus no cross-sensitivities between openings and stresses along different modes are taken into account. The damage variable in mode I is distinguished from d, in order to avoid interpenetration of opposite crack surfaces

$$\begin{cases} d_I = d & \text{if } \Delta_I > 0 \\ d_I = 0 & \text{if } \Delta_I \leq 0 \end{cases} \tag{2.34}$$

In all locations where the mode I opening is negative, the penalty stiffness is restored along this direction, so that only minimal interpenetration is allowed.

2.2.4 Stiffness matrix and residual vector

The stiffness matrix of the cohesive element can be written in the classic form as

$$\boldsymbol{K} = \iint_A \boldsymbol{B}\boldsymbol{D}\boldsymbol{B}^T \mathrm{d}A \tag{2.35}$$

where A is mid-surface of the CE.

The integral in Equation (2.35) is mostly computed numerically. The quadrature scheme and the number of integration points (IPs) used depend on the element type. Generally, Gaussian schemes are preferred to Newton-Cotes ones, as the former ensure higher degrees of accuracy (order of the polynomial integrated exactly) for the same amount of IPs. However, for cohesive elements, the integrand sampled with Gaussian IPs can show fictitious material interpenetration, when the element is in an intermediate damage state. Despite this should favour Newton-Cotes quadrature for CEs integration, the debate is still open on which scheme is better suited for this application [3, 24–27].

An incremental-iterative analysis is usually employed to solve the non-linear system of equations of the finite element model. Depending on the solution technique adopted, $\boldsymbol{K}$ can be re-computed at each iteration (Full/Quasi Newton-Raphson methods), once at the each increment (Modified Newton-Raphson method) or only at the beginning of the first increment (Linear Elastic Stiffness method). The choice of the method also affects the magnitude of the residual vector, which represent the unbalance between external and internal forces for each degree of freedom of the FE model. The general form of the residual vector $\boldsymbol{f}$ for a surface-defined element is

$$\boldsymbol{f} = \boldsymbol{f_{ext}} - \boldsymbol{f_{int}} = \iint_A \boldsymbol{N}\boldsymbol{t}\,\mathrm{d}A - \iint_A \boldsymbol{B}\boldsymbol{\tau}\,\mathrm{d}A \tag{2.36}$$

The first integral in Equation (2.36) expresses the nodal forces due to the external applied loads, while the second term includes the internal reactions at each node. Making the assumption that external loads are not directly applied on interface elements, only the internal

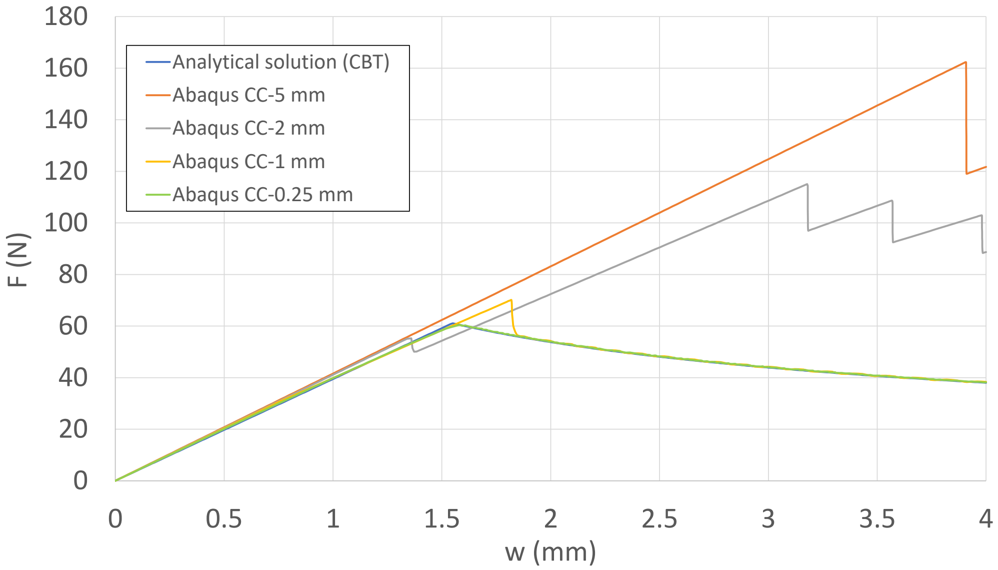

Figure 2.10: Load displacement curves for a DCB specimen, obtained with Abaqus CC analyses for different element sizes in the fracture region. The CBT solution is used as analytical reference.

force term contributes to the residual. Recalling Equation (2.15), $\boldsymbol{f}$ can be expressed as

$$\boldsymbol{f} = -\iint_A \boldsymbol{B}\boldsymbol{D}\boldsymbol{B}^T \,\mathrm{d}A\, \boldsymbol{U} = -\boldsymbol{K}\boldsymbol{U} \tag{2.37}$$

Thus, as long as $\boldsymbol{K}$ and $\boldsymbol{U}$ are updated for the current iteration, the residual vector $\boldsymbol{f}$ is obtained by simple matrix multiplication.

2.3 The Mesh Density Constraint

Figure 2.10 shows different numerical load displacement curves for a double cantilever beam (DCB) unidirectional composite specimen. The analytical solution obtained with the Corrected Beam Theory (CBT, Appendix E) is also plotted for reference. All the numerical curves derive from Abaqus Cohesive Contact (CC) analyses, where CC is a CZM-based contact relation between a master and a slave surface. If the same cohesive law, onset and propagation criteria are used, results obtained with CEs and CC usually show little difference, especially for very small interface thicknesses.

Different curves in Figure 2.10 correspond to different element sizes in the region involved by fracture. The chart clearly represents the essence of the mesh density constraint. Only the model with a 0.25 mm element size complies to the requirement of having at least 3 elements in the 0.875 mm cohesive zone length, hence the corresponding curve is the sole matching the analytical solution. Meshes of 1 mm, 2 mm and 5 mm overshoot the limit load by 15%, 88% and 163% respectively. Also they show a fictitious unstable crack growth after the limit

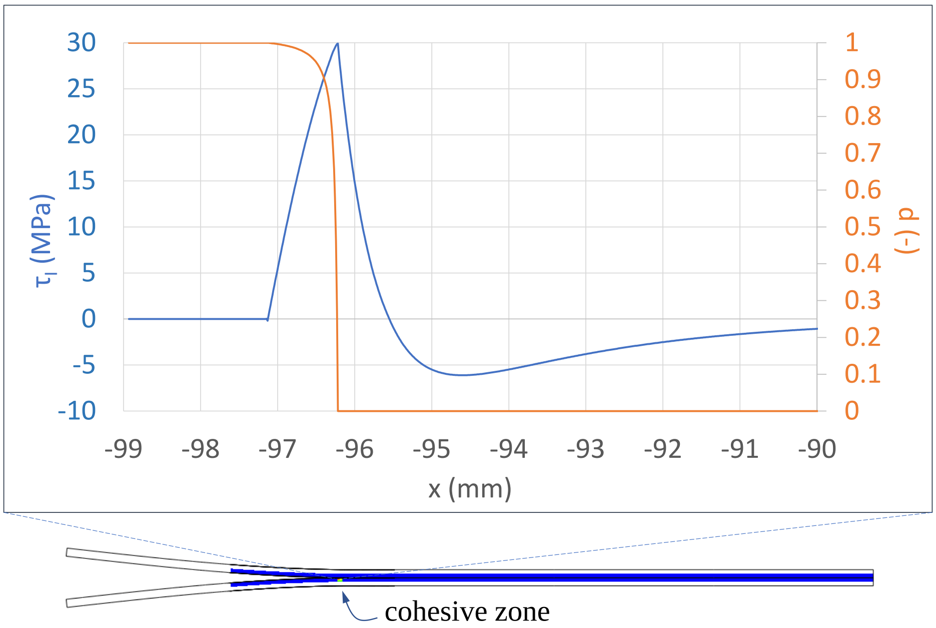

Figure 2.11: Stress and damage profiles in the CZL of a 2D DCB specimen, obtained with Abaqus CC analysis. The element length is 0.0125 mm in the propagation region.

point and for the 2 and 5 mm cases the propagation branch is completely missed. Considering that the length of the specimen is 150 mm, one can easily figure how the need of a 0.25 mm element size translates in excessive computational costs.

The mesh density constraint arises from the limited interpolation power of linear bulk and cohesive elements. If the displacements of the separating specimen's arms are not captured accurately, neither are the damage and traction gradients present in the short cohesive zone (Figure 2.11) and the structural response can greatly differ from the true one.

2.3.1 Cohesive Zone Length

Knowledge of the length of the cohesive zone, abbreviated as CZL, is necessary whenever working with CZM-based methods. With linear CEs/CC, this dimension dictates the maximum element size for accurate predictions, but, more in general, the CZL is a characteristic dimension of nearly every fracturing continuum (exceptions are the purely brittle materials, where the process zone is smaller than the continuum scale). Therefore, every numerical method that is not based on pure linear elastic fracture mechanics must take the CZL into account in its implementation.

The size of the cohesive zone in a fracturing structure shows several sensitivities. Material properties, geometry and opening mode are all physical factors which influence the CZL and to these adds the shape of the cohesive law.

The first attempts in literature to estimate the CZL made the assumption of an infinite body, in order to exclude the effects of the geometry. The general expression for the CZL in this case is [19]

$$l^{\infty}_{cz,i} = M^{\infty}_{i} \frac{E_i G_{i,c}}{(\tau^0_i)^2}, \qquad i=1,\ 2,\ m \tag{2.38}$$

with

$$E_m = E_I(1-B) + E_{II} \tag{2.39}$$

E_i is the Young modulus along the i^{th} mode, while $G_{i,c}$ and τ^0_i are respectively the critical energy release rate and the strength of the material for the same mode. As observed by Soto [28], M^{∞}_i is a factor that, for a given mixity ratio, solely depends on the cohesive law of choice. A set of values for M^{∞}_i in pure mode I loading are given in Table 2.1. The CZL for this opening mode is usually smaller than for any other mode-mixity, making this loading case the most critical in terms of MDC.

Reference	$\mathbf{M^{\infty}_{I}}$
Hui et al. [29]	$\frac{2}{3}\pi$
Irwin [8]	$\frac{1}{\pi}$
Dugdale [11]	$\frac{\pi}{8}$
Rice [30], Falk et al. [31]	$\frac{9}{32}\pi$
Hillerborg et al. [32]	1.0

Table 2.1: M_I values in literature.

Later models for the CZL also accounted for the problem's geometry, particularly considering thin structures. Two relevant solutions from Smith [33] for pure mode I and Massabò-Cox [34] for mode II, are respectively

$$l^0_{cz,I} = M^0_I \, (l^{\infty}_{cz,I})^{\frac{1}{4}} \, t_a^{\frac{3}{4}} \tag{2.40}$$

$$l^0_{cz,II} = M^0_{II} \sqrt{l^{\infty}_{cz,II} \, t_a} \tag{2.41}$$

where t_a is the thickness of the delaminating arm and $l^{\infty}_{cz,i}$ is the CZL for an infinite body taking M^{∞}_i=1. As in the case of an infinite body, the coefficients M^0_I and M^0_{II} depend exclusively on the cohesive law used.

Authors such as Turòn *et al.* [35] and Harper *et al.* [2] demonstrated that Equations (2.40) and (2.41) overestimate the length of the cohesive zone and some researchers proposed their own models. In particular Turòn and co-workers suggested a formulation that also covers mixed-mode openings, while Soto *et al.* [28] proposed to use a weighted average between the CZL for infinite bodies and that for thin structures. Though both of these formulations can achieve accurate predictions of the CZL, they are only semi-analytical, since some of their parameters are found by curve-fitting of experimental data.

2.3.2 Solutions to the MDC

The mesh density constraint imposes a minimum number of CEs in the cohesive zone length. However, the models developed so far to estimate this dimension are either inaccurate or of limited applicability. Without confidence in the CZL measure, two choices are left to the analyst for having precise delamination predictions. The first one is using an extremely fine mesh, so to comply doubtlessly with the MDC. The second alternative requires to follow a coarse-to-fine approach to mesh sensitivity, until convergence of the sought-for results. Clearly, both methods are inefficient and would generate a bottleneck during structural design.

If the time between the creation of the first FE delamination model and the achievement of converged results is to be minimized, the mesh density constraint must be alleviated, if not completely removed. In agreement with the theme of this research, the next sections discuss some remarkable methods for MDC reduction, dividing them in two categories. The first group gathers all the works where the FE solution is globally C^0-continuous, while the remaining strategies use approximations with higher regularity.

C^0 solutions

Material strength reduction The expression of the CZL in Equation (2.38) is inversely proportional to the square of the material strength. This relation was exploited by Turòn *et al.* [19] to adopt a somehow counter-inuitive approch to the MDC problem, that is to allow for larger CE dimensions by extension of the CZL itself.

Choosing *a-priori* the length of the CEs (l_{el}) in the CZL and prescribing the number of elements N_{el} that this has to contain, the strength of the material is uniquely determined by Equation (2.38). For pure mode I loading, using $M_I^\infty = \frac{9}{32}\pi$ (see Table 2.1)

$$\tau_I^0 = \sqrt{\frac{9\pi E_I G_c}{32 N_{el} l_{el}}} \tag{2.42}$$

Keeping 5 elements in the cohesive zone and allowing τ_I^0 to decrease, the authors of the study showed DCB test results with limited error on the peak load, using up to 2.5 mm element lengths. Although local stresses and damage distributions obtained with this expedient are not realistic, the method well captures the global response for mode I delamination, ensuring limited CPU times.

The strength reduction strategy is not as powerful when applied in mode II delamination. This was noticed by Harper and Hallet [2], who showed how in a pure mode II End-Notched-Flexure (ENF) test, reducing the material strength resulted in lower peak loads and flattening of the load-displacement curve (Figure 2.12). In fact, large mode II strength reductions can greatly increase the extent of the process zone, causing global softening and a plastic-like behaviour. Also, the authors showed that increasing the CE length always altered the load-displacement curves, except for low values of the interface strength, which anyway give inaccurate results.

Enriched displacement field Another class of methods dealing with the mesh density requirement is based on enriching the solution's space of both bulk and cohesive elements. The idea is to add new shape functions or to modify the existing ones, using the analytical solutions of simplified fracture models.

Guiamatsia *et al.* used the beam on elastic foundation solution as enrichment function. They initially tested their element implementation only in mode I [36] and then presented examples also for mixed mode delamination [37]. The expression of the out-of-plane displacement was

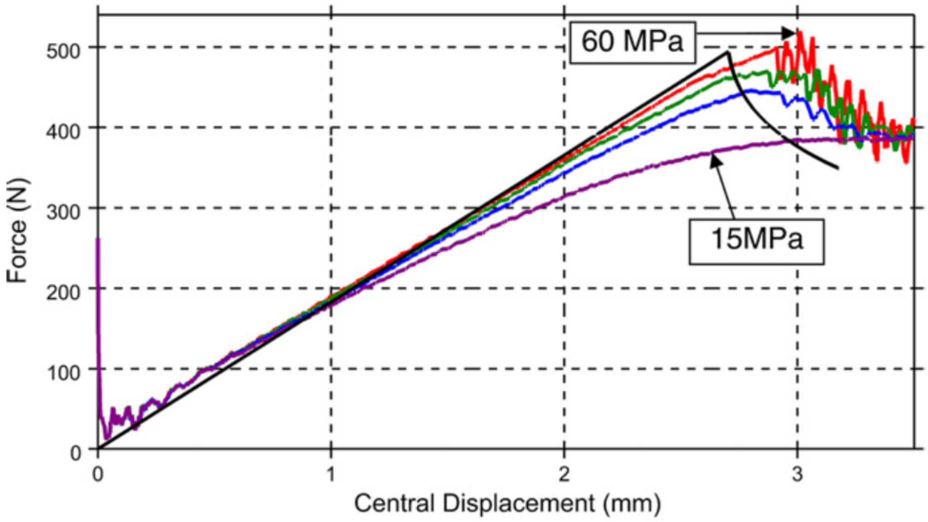

Figure 2.12: Effect of strength reduction for a ENF test [2].

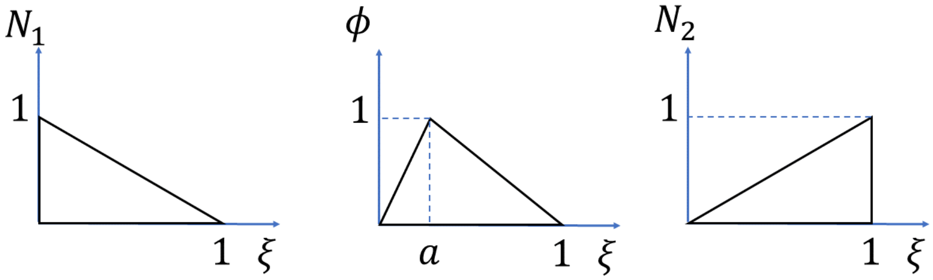

Figure 2.13: Enriched shape functions space proposed by Samimi *et al.* in [39].

based on the partition of unity method [38], in order to maintain an interpolative approximation. This reads, for a 2D element

$$w(x) = N_i(x)(w_i + \overline{w_{ij}}\phi_j(x)), \qquad i{=}1{:}M,\ j{=}1{:}J(i) \tag{2.43}$$

where terms with repeated indices are summed together. A total of $J(i)$ degrees of freedom $\overline{w_{ij}}$ and enrichment functions $\phi_j(x)$ are added for each node i. M is the total number of nodes. None of the articles mentions the CZL, nor they provide data to derive it. However the authors give indications about the minimum element length. For the DCB specimen in [36], the linear CEs solution requires a 0.5 mm CE size to obtain converged results, whereas enriched elements as long as 5 mm can correctly predict the delamination length. In case of a 2 mm mesh, also the load-displacement curve is reproduced accurately. Using this element size, a 37% CPU time reduction is achieved with respect to the 0.5 mm linear CE solution. However in [37], the authors mention that for elements larger than 3 mm, the enrichment could lead to inaccuracies in interpolating the degrees of freedom. Also, despite MDC alleviation is also reported for mixed mode, improvements for pure mode II are not discussed and they are likely not achievable, since the beam on elastic foundation problem only models mode I fracture.

A different approach to element enrichment was proposed by Samimi *et al.* [39–41]. These authors augmented the solution space of both substrate and cohesive elements in a hierarchical manner, by adding a bilinear function, solution of a peel-off problem. The complete set of shape functions for a univariate interface element is represented in Figure 2.13 and reads

$$N_1(\xi) = \xi \tag{2.44}$$

$$N_2(\xi) = 1 - \xi \tag{2.45}$$

$$\phi(\xi) = \frac{1}{a}\xi - \frac{1}{a(1-a)}\mathcal{R}(\xi - a) \tag{2.46}$$

where $\phi(\xi)$ is the enrichment function, a is the unknown position of the opening peak and $\mathcal{R}$ simply reads

$$\mathcal{R}(\xi - a) = \begin{cases} 0 & \text{if } \xi \leq a \\ \xi - a & \text{if } \xi > a \end{cases}$$

The hierarchical enrichment with the bilinear shape function in Equation (2.46) adds three degrees of freedom for each cohesive element, the peak position a and two scaling factors for top and bottom sides of the interface. The method was tested for both a 2D and 3D version of the peel-off problem. The numerical solution was compared with the analytical one, but no considerations on the ratio between element size and cohesive zone length were done. However the results showed that the enrichment permitted a partially damaged state of the element. This translated in limited numerical oscillations of the load-displacement curve upon propagation, using mesh sizes which are prohibitive for linear CEs.

Sub-domain integration and level set Recalling Figure 2.11, if a cohesive elements is larger than the cohesive zone, thus has to contain it, stress and damage distributions in the non-separated portion of its domain will be strongly non-linear. The research groups of Yang [26] and Do [42] demonstrated that larger element dimensions can be achieved, provided that enough integration points are placed in the moving cohesive zone.

These authors used a mixed integration scheme, combining Gaussian Integration (GI) and Sub-Domain Integration (SDI). Intact cohesive elements are integrated with the standard Gaussian quadrature and failed CEs do not require any integration of the stresses. However, for partially bonded CEs containing the cohesive zone, the crack front has to be fist identified, using a *level-set* and while the failed part is not integrated, a Gaussian scheme is used for the partially damaged one. Thus, quadrature in the last case is performed only on the non-failed sub-domain. Figure 2.14 illustrates the differences between a full-GI and a GI-SDI scheme and how the crack front is located in the latter case.

Simulating fracture in a Double Cantilever Beam (DCB) specimen, the method accurately predicted peak load and propagation phase for CE dimensions up to 1.43 times the estimated CZL, and achieved convergence for a ratio of 2.14. Even larger meshes meant however increasingly severe oscillations during crack propagation and an over-prediction of the limit load.

Quadratic CEs and IPs density A different approach towards relaxing the MDC is to increase the order of interpolation of the displacement fields of bulk and cohesive elements. This idea was pursued by Álvarez *et al.* [43], who developed a quadratic CE and also added the

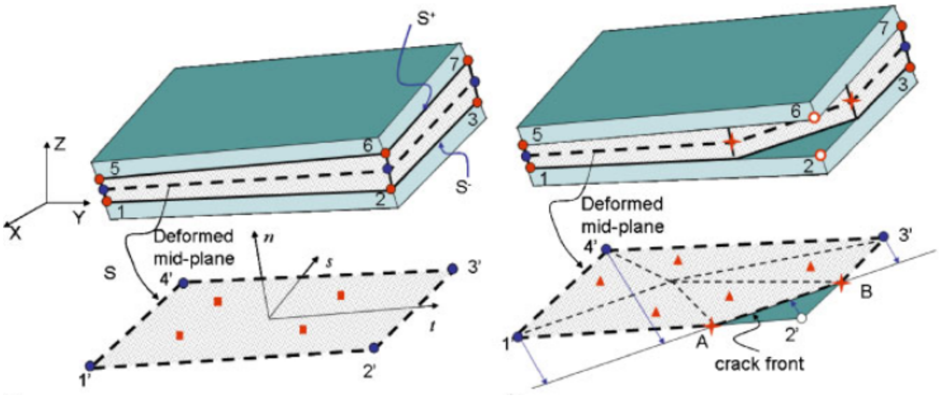

Figure 2.14: Sub-domain integration with crack front tracking [26].

possibility to increase the number of integration points used. A quadratic interpolation can more precisely reproduce small curvature radii due to bending, hence it better captures the interface opening. More IPs mean less damage accumulation and release at each increment, thus smaller fluctuations of the solution during propagation.

The results achieved with this method for a 2D DCB test with an adhesive interface are visible in Figure 2.17. Convergence, accuracy on the peak load values and limited oscillations were obtained with CEs twice as long (20 mm) the CZL (10 mm), which translated in CPU time savings of 69.5% with respect to the standard linear CE solution.

Despite the remarkable performances of the method, it is doubtful whether this is actually an ultimate solution to the MDC. In fact, looking at the thinnest DCB specimen geometry analyzed by Álvarez and co-workers (Figure 2.15), it is noticed how the pre-cracked portion has a thickness-to-length ratio larger than $\frac{1}{10}$. Also, the load is not applied in a concentrated manner, but through a lug. Such a configuration does not have the bending compliance of a thin beam, meaning that the FE approximation of it does not have to fulfill the stringent C^1-continuity requirement proper of thin models. Given that the order of this method is C^0, it is likely that the improvements observed in this study would not hold for slender geometries with concentrated loads.

The previous considerations on geometry and loading are credible when looking at the results obtained by Russo [44]. Quadratic cohesive elements were also used to model the thin specimen shown in Figure 2.16, for which a CZL of 0.825 mm was computed. The load-displacement curves for different mesh sizes, reported in Figure 2.18, indicate a threshold for the CE size of 1 mm, meaning a CE length to CZL ratio of 1.21, before unacceptable accuracy loss. Such observations demonstrate how quadratic interpolation without higher continuity is an improvement although not a solution to the MDC.

Thick level set Several authors investigating delamination chose to describe either the crack front or the damage zone with level sets. A pioneering work in this sense, although not based on CZM, is that of van der Meer *et al.* [46], who used LEFM to describe the motion of the crack front. The method achieved accurate matching of the analytical solutions in a number of benchmark tests, but it is limited to single delamination scenarios.

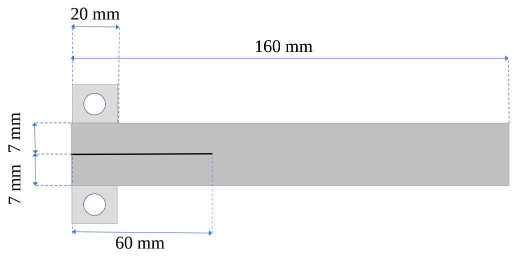

Figure 2.15: DCB specimen geometry studied by Álvarez [43].

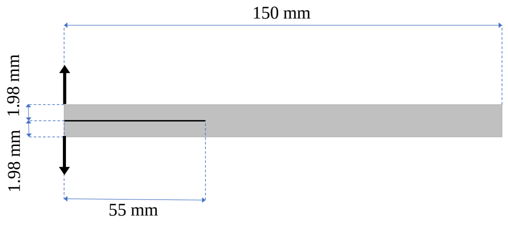

Figure 2.16: DCB specimen geometry studied by of Russo [44].

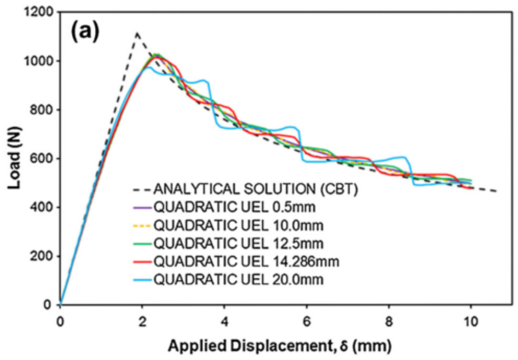

Figure 2.17: DCB Load-displacement curves obtained by Álvarez [43].

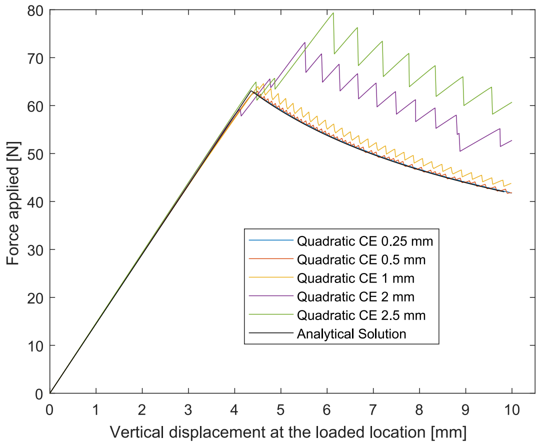

Figure 2.18: DCB Load-displacement curves obtained by Russo [44].

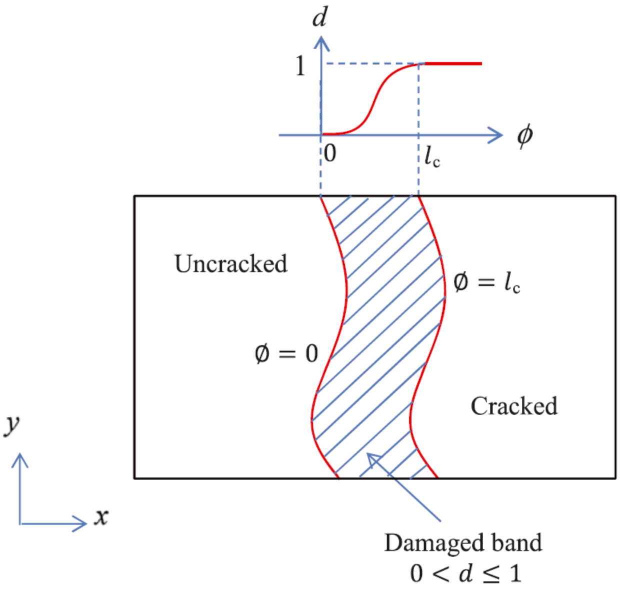

Figure 2.19: Level set field and damage function [45].

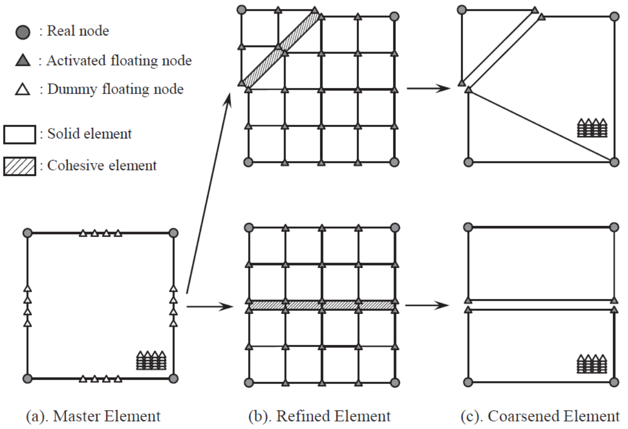

Figure 2.20: The adaptive floating node element in its three versions [47].

Working with some of the same authors, Latifi [45] generalized the approach, introducing the cohesive zone and modelling it through a thick level set $\phi(x, y)$ (Figure 2.19). Damage is described as a given function of ϕ and the damage zone is delimited by two lines where the level set field is constant. The openings and stresses are computed at the beginning of the increment, allowing to determine the energy release rate. Up until reaching the critical energy release rate, the expansion of the damage region is dictated by damage mechanics. When $G = G_c$ and the length of the cohesive zone becomes fully developed, propagation develops as described by fracture mechanics.

As the method allows for the choice of the cohesive zone length l_c, this can be extended to fit the minimum number of CEs for stable and accurate simulations. However, no sensitivity study on the CE size is presented in the article and the simulations are all conducted with fine meshes, preventing from drawing conclusions about the MDC.

Adaptive floating node method Recently, Lu *et al.* [47] proposed a version of the Floating Node Method (FNM) [48] capable of adaptivity (A-FNM) and tested it in terms of minimum CE size. Thanks to the essence of FNM, the method avoids global remeshing and mapping of nodal/element variables required to adaptive mesh refinement schemes.

Each original element is attributed a set of real nodes, which define the initial mesh and floating nodes for their edges and area. Before any damage occurring, the floating nodes are inactive and the element is in its master configuration, as shown in Figure 2.20. A refinement zone of three times the length of the cohesive zone is located ahead of the crack tip. As soon as one element enters the refinement region, the floating nodes are activated to form a grid, such that three sub-elements cover the cohesive zone (refined configuration). Sub-cohesive elements are inserted in between the bulk ones just defined. If one master element is fully separated, a check on its strain energy is done to see if the grid can be coarsened by leaving only the floating nodes defining the crack (coarsened configuration).

The benchmark problems analyzed proved the superiority of this method as compared to the standard CEs schemes. For instance, for the 2D DCB specimen case, an initial coarse mesh of 3 mm could be used, against a mesh of 0.2 mm element size needed for the standard FEM model. The method succeeded to achieve CPU time savings up to 47% in DCB simulations.

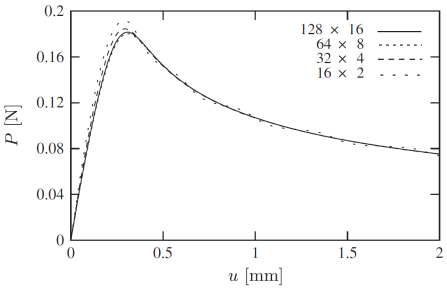

Figure 2.21: DCB in [53]: load-displacement curve.

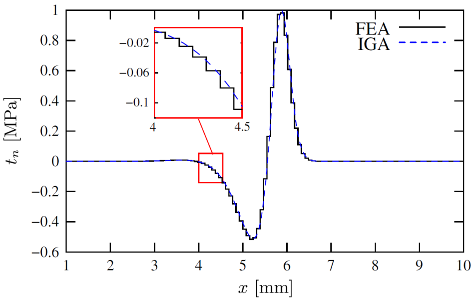

Figure 2.22: DCB in [53]: transverse stress profile.

Higher regularity solutions

Isogeometric Analysis Mid-way during the last decade, Hughes *et al.* [49, 50] developed the concept of Isogeometric Analysis (IgA). The original aim was to remove the lengthy step of creating the FE mesh, by using the anyway necessary geometrical mesh modelled in a Computer Aided Design (CAD) platform.

All the different functions available in CAD modelling offer a large flexibility on their continuity. Regularity can be tuned both by changing the order of interpolation and by adding or removing *knots*, the IgA equivalents of the FE nodes. These processes are known respectively as p-refinement and knot-insertion.

The applicability of IgA to fracture mechanics has been investigated thoroughly over the present decade. In particular, not only IgA grants the appealing features of modelling the structure's geometry exactly and the possibility of having regular solutions, but it also allows to create discontinuities through knot-insertion. Moreover, since the studies of Borden, Scott *et al.* [51, 52] IgA implementations could be made compatible with the available FE codes, thanks to the process of *Bézier Extraction*.

Examples of delamination analyses with isogeometric shape functions are given in the works of Irzal [53], Nguyen [54] and Hosseini [55] either for two or three-dimensional problems. None of these studies though examines on purpose the element density in the cohesive zone. However, considering the DCB example in [53] and using the data provided, the element length for the coarser mesh is found equal to 0.625 mm and Equation (2.40) gives a CZL value of 0.63 mm. Despite the element length-to-CZL ratio being greater than the recommended $\frac{1}{3}$ to $\frac{1}{10}$ values, the simulations show convergence and smoothness, as it can be observed in Figures 2.21 and 2.22.

3rd order CEs and adaptive integration In his work, Russo [44, 56] adopted C^1-continuous substrates and cohesive elements to study 2D delamination. The faces of the CE share the nodes of the Euler-Bernoulli beam elements used for modeling the sublaminates. Figure 2.23 shows however that the actual upper and lower sides of the CE have an offset of half the substrate thickness from the neutral axes of the beams. The presence of the beam's thickness also affects the displacement field of the CE faces, written as, respectively for horizontal and

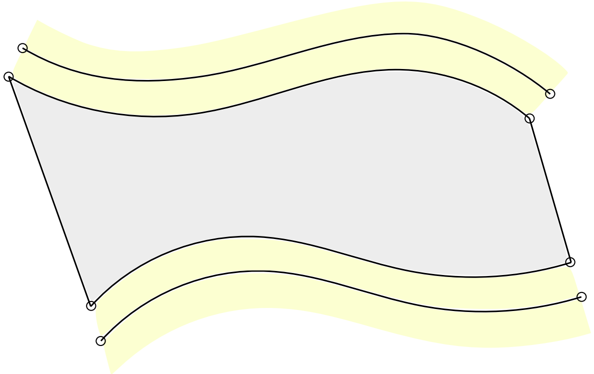

Figure 2.23: Configuration of the CE implemented by Russo [44].

vertical components and for bottom and top face

$$\begin{cases} u_{CE_b}(\xi) = & u_{B_b}(\xi) + \frac{t}{2}\sin\theta_{B_b}(\xi) \\ w_{CE_b}(\xi) = & v_{B_b}(\xi) - \frac{t}{2}(1-\cos\theta_{B_b}(\xi)) \end{cases} \tag{2.47}$$

$$\begin{cases} u_{CE_t}(\xi) = & u_{B_t}(\xi) - \frac{t}{2}\sin\theta_{B_t}(\xi) \\ w_{CE_t}(\xi) = & v_{B_t}(\xi) + \frac{t}{2}(1-\cos\theta_{B_t}(\xi)) \end{cases} \tag{2.48}$$

The CE and B subscripts in Equations (2.47) and (2.48) refer to quantites of the beam and of the cohesive element respectively, t is the substrate's thickness and θ_B is the beam's rotation for a given value of the parent coordinate ξ.

Russo also implemented a co-rotational formulation for his CE model, so to account for large displacements and rotations in computing the openings. In addition, these CEs can be adaptively integrated. Simlarly, to Yang's SDI scheme [26], but refining over the entire element domain, partially debonded elements are given a large number of integration points, while the fully intact or failed ones are integrated with just 3 IPs.

The DCB load displacement curves obtained by Russo are compared with different references in Figure 2.24. Different mesh sizes are shown both for the high order adaptively integrated CEs and the linear ones. The CZL was predicted to be 0.825 mm. For a 2.5 mm mesh, meaning an element size-to-CZL ratio of 3, the Abaqus solution with linear CEs over-predicted the limit load by 85% the experimental value, while Russo's cohesive elements were accurate up to a 4% deviation. Using a 5 mm mesh, the novel method missed the limit load by only 8%, whereas linear CEs did not predict delamination in the displacement range examined. Spurious oscillations were kept low in magnitude thanks to the high number of IPs in the moving cohesive zone. The CPU time required by the new cohesive element models with a 2.5 mm mesh was of 47 seconds, against the 43 minutes and 24 seconds needed by the Abaqus standard, meaning a 98% saving.

The captivating performances of this method are motivated by the use of Euler-Bernoulli beam elements together with C^1 CEs. High order and regularity of this scheme ensure that the bending deformation of the specimen's arms, hence the interface opening, is accurately reproduced even with few elements. Since damage and stresses depend on the openings through the cohesive law, also these quantities are well predicted, as are the onset and progression of the interface failure.

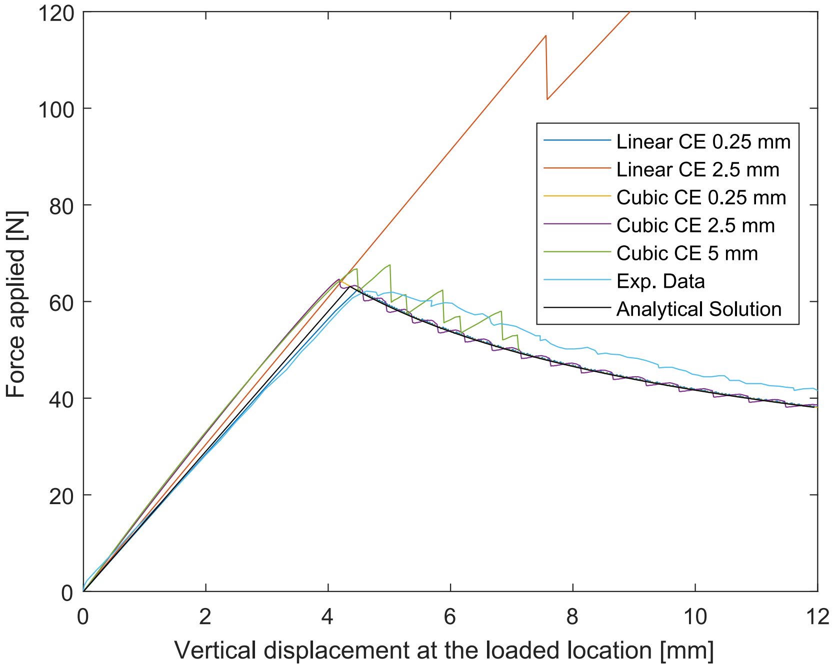

Figure 2.24: DCB load-displacement curves obtained with Russo's method [44]. Standard CE results, analytical solution and experimental data are also reported.

The binomial of accuracy and minimal CPU times obtained by Russo expresses the importance of basing a numerical model on the mechanics of the physical problem. This idea is what motivated the present research to test thin structural theories for reproducing delamination in three-dimentional analyses.

Chapter 3

Proposed Solution

The results from IgA and the 3$^{\text{rd}}$ order C^1 cohesive elements show that not only the order, but also the regularity of the numerical solution is key for accurate and efficient delamination analyses. The reason for this is that the separating arms of a delaminating composite are slender elements that, under the applied load, deform either as Euler-Bernoulli beams in two dimensions or as Kirchhoff plate/shells in a 3D space. As it will be soon discussed, these structural theories require the solution to be at least C^1-continuous over the entire problem's domain.

The present chapter is structured as follows. First, the strong and weak forms of the Kirchhoff equation for plates in bending are derived, from which the C^1-continuity requirement will be expressed in formulas. Following, the triangular thin-plate element, known as TUBA3 or Bell's triangle [57] is discussed and its stiffness matrix and residual vector are built. Finally, the same fundamental arrays are derived for the TUBA3-compatible cohesive element (TUBA3-CE).

Both plate element and compatible CE were implemented as Abaqus user-element subroutines [13] and written in the FORTRAN95 programming language.

3.1 C^1-continuity in the thin plate model

The regularity condition for thin plates is better understood starting from the more general Reissner-Mindlin (R-M) theory. In this model, two main assumptions are done regarding the plate's deformation. First, sections that are straight in the reference configuration remain straight in the deformed one. Moreover, out-of-plane stresses and strains are neglected, thus

$$\sigma_z = \varepsilon_z = 0 \tag{3.1}$$

In agreement with the previous assumptions, the displacement of each point is described only by the out-of-plane deflection w and by the θ_x and θ_y rotations of the plate's mid-plane. No in-plane deformations are considered and all displacements are assumed to be small. Figure 3.2

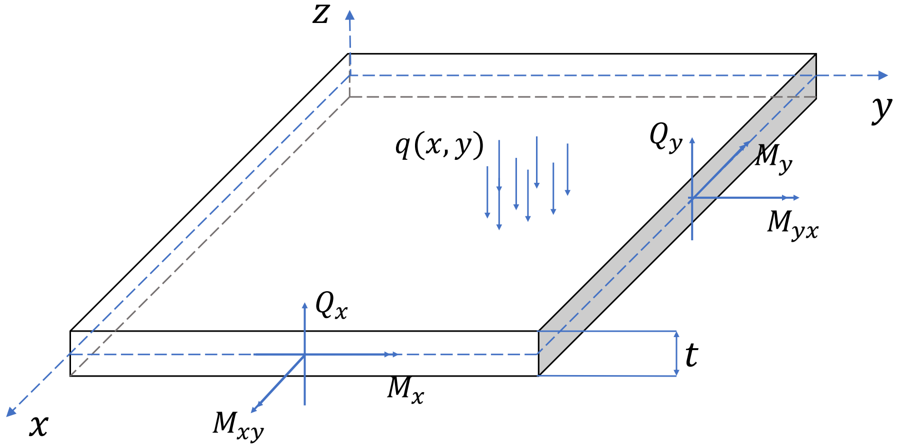

Figure 3.1: First order shear plate model. Out-of-plane load and internal forces and moments are evidenced.

shows the plate's kinematics in the xz-plane. Deformations in the yz-plane are equivalent, if θ_y is considered in place of θ_x. Altogether, the displacements in bending are expressed as

$$\begin{cases} u(x,y,z) = & z\theta_x(x,y) \\ v(x,y,z) = & z\theta_y(x,y) \\ w(x,y,z) = & w(x,y) \end{cases} \tag{3.2}$$

Following the derivations and part of the notation in [58], the in-plane strains follow from Equation (3.2) and are written in vector notation as

$$\boldsymbol{\varepsilon} = \begin{bmatrix} \varepsilon_x \\ \varepsilon_y \\ \gamma_{xy} \end{bmatrix} = \begin{bmatrix} \frac{\partial u}{\partial x} \\ \frac{\partial v}{\partial y} \\ \frac{\partial v}{\partial x} + \frac{\partial u}{\partial y} \end{bmatrix} = z \begin{bmatrix} \frac{\partial}{\partial x} & 0 \\ 0 & \frac{\partial}{\partial y} \\ \frac{\partial}{\partial y} & \frac{\partial}{\partial x} \end{bmatrix} \begin{bmatrix} \theta_x \\ \theta_y \end{bmatrix} = z\boldsymbol{S}\boldsymbol{\theta} \tag{3.3}$$

Similarly, the transverse shear strains read

$$\boldsymbol{\gamma} = \begin{bmatrix} \gamma_{xz} \\ \gamma_{yz} \end{bmatrix} = \begin{bmatrix} \frac{\partial}{\partial z} & 0 & \frac{\partial}{\partial x} \\ 0 & \frac{\partial}{\partial z} & \frac{\partial}{\partial y} \end{bmatrix} \begin{bmatrix} z\theta_x \\ z\theta_y \\ w \end{bmatrix} = \begin{bmatrix} \theta_x + \frac{\partial w}{\partial x} \\ \theta_y + \frac{\partial w}{\partial y} \end{bmatrix} = \boldsymbol{\theta} + \nabla w \tag{3.4}$$

Imposing zero out-of-plane strains and stresses implies that each layer of the plate is in a plane stress condition, even though τ_{xz} and τ_{yz} are generally non-zero. In case of an isotropic material, the plane stress constitutive relation links stresses and strains as

$$\begin{bmatrix} \sigma_x \\ \sigma_y \\ \tau_{xy} \end{bmatrix} = \frac{E}{1-\nu^2} \begin{bmatrix} 1 & -\nu & 0 \\ -\nu & 1 & 0 \\ 0 & 0 & \frac{1-\nu}{2} \end{bmatrix} \begin{bmatrix} \varepsilon_x \\ \varepsilon_y \\ \gamma_{xy} \end{bmatrix} = \boldsymbol{C}\boldsymbol{\varepsilon} \tag{3.5}$$

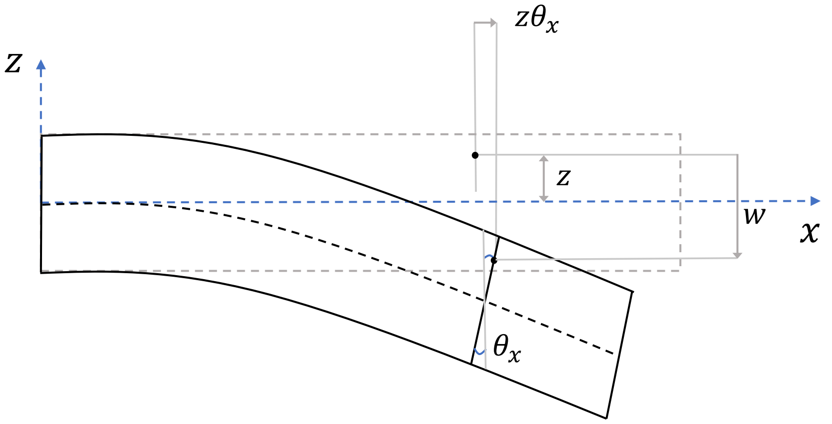

Figure 3.2: R-M plate kinematics in the xz-plane.

In Equation (3.5), the expression of the shear modulus in terms of Young's modulus and Poisson's ratio was used

$$G = \frac{E}{2(1+\nu)}$$

The transverse shear stresses also need to be determined in the R-M theory. These are obtained multiplying γ_{xz} and γ_{yz} by the shear modulus G, hence

$$\begin{bmatrix} \tau_{xz} \\ \tau_{yz} \end{bmatrix} = G \begin{bmatrix} \gamma_{xz} \\ \gamma_{yz} \end{bmatrix} \tag{3.6}$$

Integrating the stresses along the plate's thickness allows to find the moments and shear forces per unit length as

$$\boldsymbol{M} = \begin{bmatrix} M_x \\ M_y \\ M_{xy} \end{bmatrix} = \int_{-t/2}^{t/2} \begin{bmatrix} \sigma_x \\ \sigma_y \\ \tau_{xy} \end{bmatrix} z \, \mathrm{d}z = \boldsymbol{D S \theta} \tag{3.7}$$

$$\boldsymbol{Q} = \begin{bmatrix} Q_x \\ Q_y \end{bmatrix} = \int_{-t/2}^{t/2} \begin{bmatrix} \tau_{xz} \\ \tau_{yz} \end{bmatrix} \mathrm{d}z = k \, G \, t \, (\boldsymbol{\theta} + \nabla w) \tag{3.8}$$

The matrix $\boldsymbol{D}$ is the bending stiffness matrix of the isotropic plate and reads

$$\boldsymbol{D} = \frac{Et^3}{12(1-\nu^2)} \begin{bmatrix} 1 & \nu & 0 \\ \nu & 1 & 0 \\ 0 & 0 & \frac{1-\nu}{2} \end{bmatrix} \tag{3.9}$$

The factor k in Equation (3.8) is the so-called *shear correction factor* and compensates for assumption of constant shear stresses along the thickness. For an assumed parabolic distribution of τ_{xz} and τ_{yz}, k=5/6.

With the above assumptions and definitions, the equilibrium equations for a generic continuum can be integrated along the thickness to obtain the plate's differential equations of equilibrium with respect to vertical translations and x, y-rotations. These are, ultimately

$$\begin{bmatrix} \frac{\partial}{\partial x} & \frac{\partial}{\partial y} \end{bmatrix} \begin{bmatrix} Q_x \\ Q_y \end{bmatrix} + q(x,y) = 0 \tag{3.10}$$

$$\begin{bmatrix} \frac{\partial}{\partial x} & 0 & \frac{\partial}{\partial y} \\ 0 & \frac{\partial}{\partial y} & \frac{\partial}{\partial x} \end{bmatrix} \begin{bmatrix} M_x \\ M_y \\ M_{xy} \end{bmatrix} - \begin{bmatrix} Q_x \\ Q_y \end{bmatrix} = 0 \tag{3.11}$$

where $q(x,y)$ is an out-of-plane load per unit surface, acting on the top of the plate (Figure 3.1). Using the differential operators ∇ and $\boldsymbol{S}$ Equations (3.10) and (3.11) can be rewritten as

$$\nabla^T \boldsymbol{Q} + q(x,y) = 0 \tag{3.12}$$

$$\boldsymbol{S}^T \boldsymbol{M} - \boldsymbol{Q} = 0 \tag{3.13}$$

In case the plate's thickness is smaller than the in-plane dimensions of at least an order of magnitude, the Kirchhoff assumption applies to the kinematics. This establishes that every cross section normal to the mid-plane in the reference configuration is still normal to the mid-plane after the deformation. In first order approximation, the rotations are then related to the displacement gradient as follows

$$\theta_x = -\frac{\partial w}{\partial x} \tag{3.14}$$

$$\theta_y = -\frac{\partial w}{\partial y} \tag{3.15}$$

or in vector form

$$\boldsymbol{\theta} = -\nabla w \tag{3.16}$$

Substitution of Equation (3.16) in (3.4) turns the transverse shear strains to zero. The in-plane strains can instead be written as

$$\boldsymbol{\varepsilon} = z\boldsymbol{S}\boldsymbol{\theta} = -z\boldsymbol{S}\nabla w = -z \begin{bmatrix} \frac{\partial^2 w}{\partial x^2} \\ \frac{\partial^2 w}{\partial y^2} \\ 2\frac{\partial^2 w}{\partial x \partial y} \end{bmatrix} = -z\boldsymbol{\mathcal{L}} w \tag{3.17}$$

with

$$\boldsymbol{\mathcal{L}} = \boldsymbol{S}\nabla = \begin{bmatrix} \frac{\partial^2}{\partial x^2} & \frac{\partial^2}{\partial y^2} & 2\frac{\partial^2}{\partial x \partial y} \end{bmatrix}^T$$

In case of a thin plate, the distributed bending moments become

$$\boldsymbol{M} = \boldsymbol{D}\boldsymbol{S}\boldsymbol{\theta} = -\boldsymbol{D}\boldsymbol{\mathcal{L}} w \tag{3.18}$$

The two equilibrium conditions in Equations (3.12) and (3.13) can be combined by multiplying (3.13) by ∇^T and using Equation (3.18). This allows to write the strong form of the equilibrium equation for thin plates as

$$-\boldsymbol{\mathcal{L}}^T \boldsymbol{D}\boldsymbol{\mathcal{L}} w + q = 0 \tag{3.19}$$

Equation (3.19) requires the existence of the 4th derivatives of w, which is a strong regularity condition for the solution. However the FE discretization of a partial differential equation is derived by first obtaining its weak form, which, in mechanics, is equivalent to imposing the principle of virtual work. Starting from Equation (3.19), written as

$$\boldsymbol{\mathcal{L}}^T \boldsymbol{M} + q = 0 \tag{3.20}$$

the weak form is obtained by multiplying (3.20) by a virtual variation of the unknown w and integrating over the mid-plane A, thus

$$\iint_A \delta w \, (\boldsymbol{\mathcal{L}}^T \boldsymbol{M} + q) \, \mathrm{d}A = 0 \tag{3.21}$$

Integrating twice by parts, the weak form becomes

$$\iint_A \delta w \, q \, \mathrm{d}A + \iint_A (\boldsymbol{\mathcal{L}} \delta w)^T \boldsymbol{M} \, \mathrm{d}A + \int_{\Gamma_n} \delta\theta_n \, \bar{M}_n \, \mathrm{d}\Gamma + \int_{\Gamma_s} \delta\theta_s \, \bar{M}_{ns} \, \mathrm{d}\Gamma + \int_{\Gamma_q} \delta w \, \bar{Q}_n \, \mathrm{d}\Gamma = 0 \tag{3.22}$$

The indices n and s indicate respectively the normal and tangent directions to a plate's edge. $\Gamma_n \cup \Gamma_s \cup \Gamma_q$ is the part of the boundary where the natural boundary conditions are imposed and $\bar{M}_n$, $\bar{M}_{ns}$, $\bar{Q}_n$ are the prescribed forces and moments in the respective portions of the boundary. Since the rotations θ_n and θ_s are related to the gradient of w, through Equation (3.16), the weak form can still be reduced. Integrating by parts once more, the last two terms in Equation (3.22) can be re-written as

$$\int_{\Gamma_s} \delta\theta_s \, \bar{M}_{ns} \, \mathrm{d}\Gamma + \int_{\Gamma_q} \delta w \, \bar{Q}_n \, \mathrm{d}\Gamma = \int_{\Gamma_q} \delta w \, \bar{V}_n \, \mathrm{d}\Gamma + \sum_i \delta w \, R_i \tag{3.23}$$

with $\bar{V}_n = \bar{Q}_n + \frac{\partial \bar{M}_{ns}}{\partial s}$ representing an overall *pseudo-shear* boundary term and R_i being the concentrated forces at the plate's corners.

Substituting Equation (3.18) into (3.23), the irreducible weak form of the thin plate bending equation is finally

$$\iint_A (\boldsymbol{\mathcal{L}} \, \delta w)^T \boldsymbol{D} \boldsymbol{\mathcal{L}} \, w \, \mathrm{d}A + \int_{\Gamma_n} \frac{\partial \delta w}{\partial n} \bar{M}_n \, \mathrm{d}\Gamma + \int_{\Gamma_q} \delta w \, \bar{V}_n \, \mathrm{d}\Gamma + \sum_i \delta \, w R_i = 0 \tag{3.24}$$

The first term in Equation (3.24) indicates that the second derivative of w must be square-integrable over the mid-plane of the plate. This is possible only if $\nabla w(x, y)$ is continuous over A or, equivalently, if $w(x, y)$ is C^1-continuous.

3.2 Plate and shell elements in commercial FE codes

All the major FE programs offer several plate and shell elements for the sake of modeling thin or thick shell structures. The documentations of four widely adopted finite element codes were considered with the aim to find a pre-implemented triangular C^1 plate element.

The software NASTRAN, in its several versions, proposes four shell elements, two of which are triangular, namely CTRIA3 (linear) and CTRIA6 (quadratic) [59]. Both these elements are isoparametric (same interpolation for the geometry and the unknown fields) and based on the Reissner-Mindlin plate theory. Because of this, the fields w, θ_x and θ_y are interpolated separately and they are not related by the Kirchhoff assumption (Equation (3.16)). For this reason, CTRIA3 and CTRIA6 are both C^0.

The elements SHELL181 and SHELL281 offered by Ansys Mechanical [60] are the equivalents of the NASTRAN ones just presented. The nomenclature refers to both quadrilateral and triangular shapes. The triangular version is obtained from degeneration of the quadrilateral one, so they share the same geometrical parametrization. Again, these elements are based on the Reissner-Mindlin theory and are both C^0-continuous.

Abaqus implements a plethora of plate and shell elements, each one also defined on a triangular support [13]. Most of the alternatives are based on the Reissner-Mindlin model, thus they don't enforce the Kirchhoff assumption. However, this software also offers a plate element, named STRI3, inspired by the work of Batoz *et al.* [61], which is not strictly based on the R-M theory. In particular, STRI3 implements the Discrete Kirchhoff Theory (DKT), which imposes the Kirchhoff assumption between the nodal degrees of freedom. Despite DKT elements proved to converge quadratically to the Kirchhoff solution, STRI3 is still C^0-continuos.

Finally, the element library of LS-Dyna also presents a wide selection of plates and shells [62]. Again, for most cases the solution fields are interpolated separately, agreeing with the R-M model. However, the Type 17 and Type 18 shells are exceptions, as they implement the DKT. Remarkably, LS-Dyna recently also added isogeometric shell elements [63], which, as discussed in Section 2.3.2, can deliver high orders of regularity.

This brief outline showed that, except for the isogeometric alternative in LS-Dyna, no FE software offers plate or shell elements with continuity higher than C^0. However, the IgA shells of LS-Dyna are based on non-uniform rational B-splines (NURBS), which are defined over a quadrilateral domain. It follows that no C^1 triangular plate element is currently available 'off-the-shelf', choosing from the main FE codes. Thus, an element of such features had to be searched in literature and implemented as a user-defined subroutine compatible with a given software. For this research, Abaqus was chosen as the FE platform of use.

3.3 The C^1 TUBA3 plate element

A notorious class of triangular plate bending elements is the so-called TUBAn family, first proposed by Argyris *et al.* [64]. Each TUBAn element has n nodes and presents the following features

1. The out-of-plane displacement w and its gradient are continuous inside the element and at its boundary. In other words, all the TUBAn elements are of class C^1.
2. Among the DOFs of these elements are the bending and twisting curvatures at the corner nodes

$$\boldsymbol{k_i} = \left[\frac{\partial^2 w}{\partial x^2}|_i \quad \frac{\partial^2 w}{\partial y^2}|_i \quad 2\frac{\partial^2 w}{\partial x \partial y}|_i\right]^T \qquad i = 1,2,3 \tag{3.25}$$

The second point translates in another interesting property of TUBAn elements, besides their C^1-continuity. Having the curvatures defined at the nodes, at these points, they are continuous

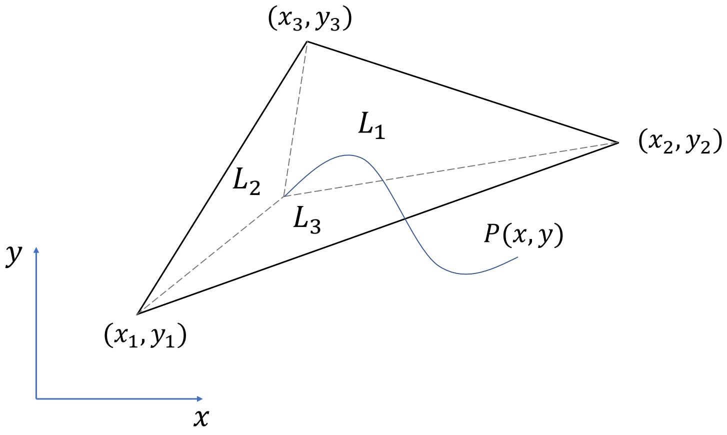

Figure 3.3: Area coordinates of a point in the generic triangle.

between neighbouring elements. It follows that stresses and strains are also continuous at the nodes, since

$$\boldsymbol{\varepsilon} = -z\boldsymbol{k}$$
$$\boldsymbol{\sigma} = \boldsymbol{C}\boldsymbol{\varepsilon}$$

3.3.1 TUBA3: DOFs and shape functions

The TUBAn element chosen for this work is the three-noded TUBA3, also known as Bell's triangle [57]. This element will be presented by deriveing it from the renown TUBA6, or Argyris triangle.

The interpolation of the geometry and displacement field for a triangular element is often done in terms of area coordinates (Figure 3.3). These relate to the Cartesian ones in the following way

$$\begin{cases} x = & L_1x_1 + L_2x_2 + L_3x_3 \\ y = & L_1y_1 + L_2y_2 + L_3y_3 \\ 1 = & L_1 + L_2 + L_3 \end{cases} \tag{3.26}$$

where (x_1, y_1), (x_2, y_2) and (x_3, y_3) are the triangle's corners in the Cartesian reference. The mapping in Equation (3.26) can be inverted to obtain the area coordinates as

$$\begin{cases} L_1 = & \frac{1}{2A}(a_1 + b_1x + c_1y) \\ L_2 = & \frac{1}{2A}(a_2 + b_2x + c_2y) \\ L_3 = & 1 - L_1 - L_2 \end{cases} \tag{3.27}$$

The coefficients a_i, b_i and c_i read

$$\begin{aligned} a_i &= x_jy_k - x_ky_j \\ b_i &= y_j - y_k \\ c_i &= x_k - x_j \end{aligned} \tag{3.28}$$

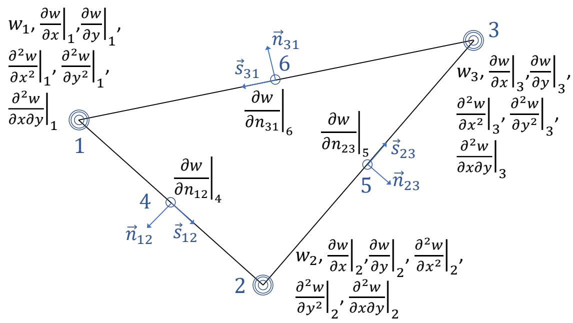

Figure 3.4: Argyris triangle (TUBA6).

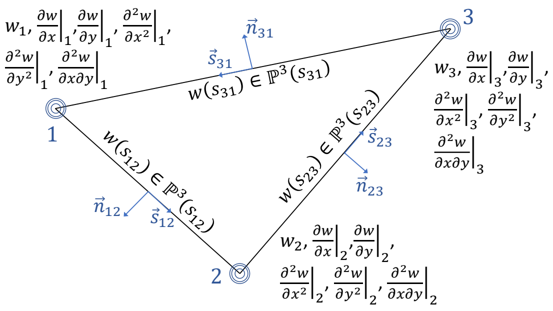

Figure 3.5: Bell triangle (TUBA3).

where the indices i,j and k are cyclic permutations of 1, 2 and 3. The term A in Equation (3.27) is the triangle's area, computed from the corners coordinates as

$$A = \frac{1}{2}\left|\det\begin{bmatrix}1 & x_1 & y_1\\ 1 & x_2 & y_2\\ 1 & x_3 & y_3\end{bmatrix}\right| \tag{3.29}$$

The Argyris triangle or TUBA6, exactly interpolates a 5th order polynomial in area coordinates, which contains all the $L_1^\alpha L_2^\beta L_3^\gamma$ products, such that $\alpha + \beta + \gamma = 5$. The out-of-plane displacement is then [65]

$$\begin{aligned} w =& \alpha_1 L_1^5 + \alpha_2 L_2^5 + \alpha_3 L_3^5 + \alpha_4 L_1^4 L_2 + \alpha_5 L_1^4 L_3 \\ &+ \alpha_6 L_2^4 L_1 + \alpha_7 L_2^4 L_3 + \alpha_8 L_3^4 L_1 + \alpha_9 L_3^4 L_2 \\ &+ \alpha_{10} L_1^3 L_2^2 + \alpha_{11} L_1^3 L_3^2 + \alpha_{12} L_2^3 L_1^2 + \alpha_{13} L_2^3 L_3^2 \\ &+ \alpha_{14} L_3^3 L_1^2 + \alpha_{15} L_3^3 L_2^2 + \alpha_{16} L_1^3 L_2 L_3 + \alpha_{17} L_2^3 L_1 L_3 \\ &+ \alpha_{18} L_3^3 L_1 L_2 + \alpha_{19} L_1 L_2^2 L_3^2 + \alpha_{20} L_2 L_1^2 L_3^2 + \alpha_{21} L_3 L_1^2 L_2^2 \end{aligned} \tag{3.30}$$

As represented in Figure 3.4, the Argyris triangle has 6 nodes and 21 degrees of freedom, so all the coefficients in (3.30) can be determined uniquely.

The Bell triangle is obtained by removing the mid-edge nodes in TUBA6, which greatly enlarge the dimension of the global stiffness matrix [57], and by imposing a cubic variation of $\partial w/\partial n$ along each edge, such that

$$\frac{\partial w}{\partial n_{ij}} \in \mathbb{P}^3(s_{ij}) \qquad i,j = 1,2,3;\ i \neq j \tag{3.31}$$

In Equation (3.31), s_{ij} is the ij^{th} edge's coordinate (Figures 3.4 and 3.5) and $\mathbb{P}^3(s_{ij})$ is the space of the cubic polynomials along s_{ij}. Three of the coefficients in Equation (3.30) can thus be expressed in terms of the other 18, by enforcing Equation (3.31) for each edge. The remaining coefficients are found by imposing the expression of w or one of its derivatives equal to the nodal quantities

$$\boldsymbol{U_i^T} = \begin{bmatrix} w|_i & \frac{\partial w}{\partial x}|_i & \frac{\partial w}{\partial y}|_i & \frac{\partial^2 w}{\partial x^2}|_i & \frac{\partial^2 w}{\partial x \partial y}|_i & \frac{\partial^2 w}{\partial y^2}|_i \end{bmatrix} \qquad i = 1,2,3 \tag{3.32}$$

The components in Equation (3.32) represent the degrees of freedom of the Bell triangle, which can be grouped in the overall DOFs vector as

$$\boldsymbol{U}^T = \begin{bmatrix} \boldsymbol{U}_\mathbf{1}^T & \boldsymbol{U}_\mathbf{2}^T & \boldsymbol{U}_\mathbf{3}^T \end{bmatrix}_{1\times 18} \tag{3.33}$$

The out-of-plane displacement can then be written, highlighting the DOFs vector, as

$$w = \begin{bmatrix} N_1 & N_2 & N_3 & \dots & N_{18} \end{bmatrix} \boldsymbol{U} = \boldsymbol{N}^T\boldsymbol{U} \tag{3.34}$$

In Equation (3.34), N_1 to N_{18} are the TUBA3 shape functions, reported explicitly in Appendix A.

3.3.2 TUBA3: stiffness matrix and residuals vector

Also in the case of TUBA3, the derivation of stiffness matrix and residual vector first requires to determine the $\boldsymbol{B}$ and $\boldsymbol{D}$ matrices.

Aligning to the finite element terminology, the strain vector is redefined for a plate as

$$\boldsymbol{\varepsilon}^T = \begin{bmatrix} \frac{\partial^2 w}{\partial x^2} & \frac{\partial^2 w}{\partial y^2} & 2\frac{\partial^2 w}{\partial x \partial y} \end{bmatrix} \tag{3.35}$$

Since

$$\boldsymbol{\varepsilon} = \boldsymbol{B}^T\boldsymbol{U} \tag{3.36}$$

the $\boldsymbol{B}$-matrix contains the derivatives of the shape functions with respect to x and y. Following the procedure carried out by Dasgupta and Sengupta [65], $\boldsymbol{B}$ can be expressed as the matrix product of other two matrices $\boldsymbol{F}$ and $\boldsymbol{Q}$, such that

$$[B]^T_{3\times 18} = \frac{1}{4A^2}[F]_{3\times 30}[Q]_{30\times 18} \tag{3.37}$$

The matrix $\boldsymbol{F}$ only contains terms in the area coordinates and reads

$$[F]_{3x30} = \begin{bmatrix} [L]^T & [0]_{1\times 10} & [0]_{1\times 10} \\ [0]_{1\times 10} & [L]^T & [0]_{1\times 10} \\ [0]_{1\times 10} & [0]_{1\times 10} & [L]^T \end{bmatrix} \tag{3.38}$$

with

$$[L]^T = \begin{bmatrix} L_1^3 & L_2^3 & L_3^3 & L_1^2L_2 & L_1^2L_3 & L_2^2L_1 & L_2^2L_3 & L_3^2L_2 & L_3^2L_2 & L_1L_2L_3 \end{bmatrix} \tag{3.39}$$

$\boldsymbol{Q}$ is a matrix which ultimately contains the corners coordinates multiplied together. It can be expressed in terms of three sub-matrices, relatively to the x, y and mixed curvatures as

$$\boldsymbol{Q} = \begin{bmatrix} [Q_{xx}]_{10\times 18} \\ [Q_{yy}]_{10\times 18} \\ [Q_{xy}]_{10\times 18} \end{bmatrix} \tag{3.40}$$

The FORTRAN95 code used for deriving the components of $\boldsymbol{Q}$ is reported in Appendix B.

If the stress vector is also redefined as

$$\boldsymbol{\sigma}^T = \begin{bmatrix} M_x & M_y & M_{xy} \end{bmatrix} \tag{3.41}$$

then the $\boldsymbol{D}$ matrix relates the generalized stresses and strains as

$$\boldsymbol{\sigma} = \boldsymbol{D}\boldsymbol{\varepsilon} \tag{3.42}$$

It is clear that, in this case, $\boldsymbol{D}$ corresponds to the plate bending stiffness matrix. For an isotropic material,

$$\boldsymbol{D} = \frac{Et^3}{12(1-\nu^2)} \begin{bmatrix} 1 & \nu & 0 \\ \nu & 1 & 0 \\ 0 & 0 & \frac{1-\nu}{2} \end{bmatrix}$$

As indicated in Figure 3.6, the configuration of a TUBA element in the physical space is parametrized in the parent domain of the area coordinates. The mapping is expressed by Equation (3.26) and its Jacobian $\boldsymbol{J_L}$ is the gradient of the physical coordinates with respect to the parent ones. Integration of the element's stiffness matrix requires the existence of the Jacobian's determinant, which is only possible if $\boldsymbol{J_L}$ is a square matrix. For this sake, the area coordinates are reduced from 3 to 2, to match the number of physical coordinates. This is easily achieved, since

$$L_3 = 1 - L_1 - L_2 \tag{3.43}$$

Substituting Equation (3.43) in the first two equations of (3.26), allows to have x and y as functions of the sole L_1 and L_2. The Jacobian is then

$$\boldsymbol{J_L} = \begin{bmatrix} \frac{\partial x}{\partial L_1} & \frac{\partial x}{\partial L_2} \\ \frac{\partial y}{\partial L_1} & \frac{\partial y}{\partial L_2} \end{bmatrix} = \begin{bmatrix} x_1 - x_3 & x_2 - x_3 \\ y_1 - y_3 & y_2 - y_3 \end{bmatrix} \tag{3.44}$$

and the determinant follows as

$$\det(\boldsymbol{J_L}) = (x_1 - x_3)(y_2 - y_3) - (y_1 - y_3)(x_2 - x_3) = 2A \tag{3.45}$$

Equations (3.9) and (3.37) define the TUBA3 stiffness matrix, written as

$$\boldsymbol{K} = \iint_A \boldsymbol{B}\boldsymbol{D}\boldsymbol{B}^T \, \mathrm{d}A \tag{3.46}$$

However, $\boldsymbol{B}$ contains the shape functions and their derivatives written in area coordinates, therefore the integral over the generic triangle $\mathcal{T}$ is performed instead on the parent triangle $\mathcal{T}_L$. Since

$$\mathrm{d}A = \mathrm{d}x\,\mathrm{d}y = \det(\boldsymbol{J_L})\,\mathrm{d}L_1\,\mathrm{d}L_2 \tag{3.47}$$

the integral in Equation (3.46) becomes

$$\boldsymbol{K} = \int_0^1 \int_0^{1-L_1} \boldsymbol{B}\boldsymbol{D}\boldsymbol{B}^T \det(\boldsymbol{J_L})\,\mathrm{d}L_1\,\mathrm{d}L_2 \tag{3.48}$$

If Equation (3.37) is substituted in the expression of $\boldsymbol{B}$, the integration restricts to the term $\boldsymbol{F}\boldsymbol{F}^T$, which is a banded matrix, built repeating the following sub-matrix

$$\boldsymbol{R} = \iint_A \boldsymbol{L}\boldsymbol{L}^T dA \tag{3.49}$$

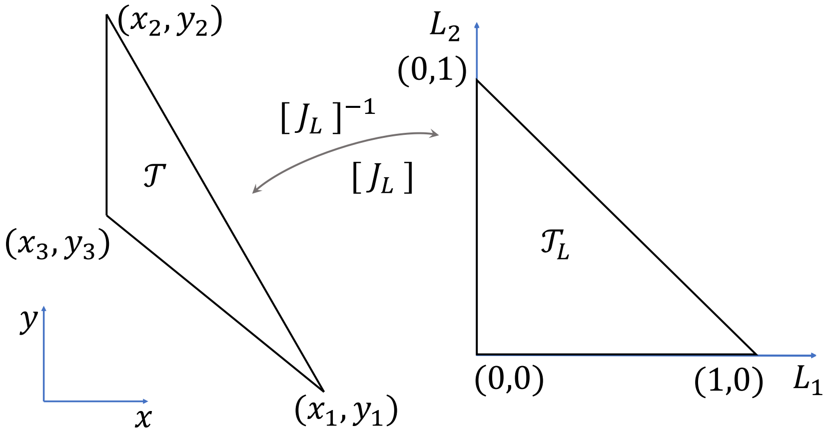

Figure 3.6: Mapping between a triangle in the physical domain and in the parent triangle.

three times along the main diagonal.

$\boldsymbol{K}$ can be finally written as

$$\boldsymbol{K} = \frac{1}{8A^3}\Big[D_{11}\boldsymbol{Q}_{\boldsymbol{xx}}^T\boldsymbol{R}\boldsymbol{Q}_{\boldsymbol{xx}} + D_{12}\boldsymbol{Q}_{\boldsymbol{xx}}^T\boldsymbol{R}\boldsymbol{Q}_{\boldsymbol{yy}} + D_{12}\boldsymbol{Q}_{\boldsymbol{yy}}^T\boldsymbol{R}\boldsymbol{Q}_{\boldsymbol{xx}} + D_{22}\boldsymbol{Q}_{\boldsymbol{yy}}^T\boldsymbol{R}\boldsymbol{Q}_{\boldsymbol{yy}} + D_{33}\boldsymbol{Q}_{\boldsymbol{xy}}^T\boldsymbol{R}\boldsymbol{Q}_{\boldsymbol{xy}}\Big] \quad (3.50)$$

Numerical integration of $\boldsymbol{R}$ can be avoided, by noticing that every integrand in $\boldsymbol{R}$ has the form $L_1^a L_2^b L_3^c$. These terms can be integrated in closed form by means of the Eisenberg-Malvern formula [66], which reads

$$\iint_A L_1^a L_2^b L_3^c \,\mathrm{d}A = \frac{a!b!c!}{(a+b+c+2)!}2A \quad (3.51)$$

Analytical integration of the stiffness matrix greatly reduces the CPU time required per-element, making TUBA3 appealing not only due to its regularity but also from an efficiency point of view.

The residual vector is again expressed as the difference between the external and internal nodal forces, therefore

$$\boldsymbol{f} = \boldsymbol{f_{ext}} - \boldsymbol{f_{int}} = \iint_A \boldsymbol{N}\boldsymbol{t}\,\mathrm{d}A - \iint_A \boldsymbol{B}\boldsymbol{\tau}\,\mathrm{d}A$$

A plate element can be subject to distributed surface loads, for which $\boldsymbol{f_{ext}} \neq 0$. As an example, Dasgupta and Sengupta derived this vector for a constant applied load [65]. The internal force vector has the usual form

$$\boldsymbol{f_{int}} = \boldsymbol{K}\boldsymbol{U}$$

and it is computed by matrix multiplication at each FE iteration.

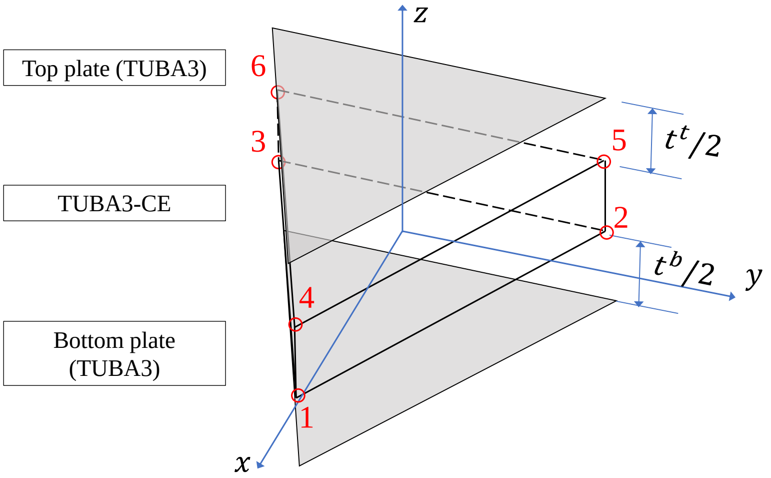

Figure 3.7: TUBA3 plates and TUBA3-CE: initial configuration.

3.4 The TUBA3-compatible cohesive element

Having described TUBA3 in terms of its degrees of freedom and characteristic arrays, the same is done here for the compatible cohesive element (TUBA3-CE).

3.4.1 TUBA3-CE: DOFs and kinematics

The undeformed configuration of TUBA3-CE is illustrated in Figure 3.7. It must be clarified that this representation gives just a physical idea of how two plates and their interface are disposed. The FE arrangement differs in the following aspects

1. The initial opening of the CE is zero
2. The nodes of the CE are exactly those of the mid-planes of the plates

The second point also implies that the CE DOFs vector is obtained stacking those of the bottom and top plates. The ordering of the nodes goes from bottom to top, following the right hand rule with respect to the element's normal, that in Figure 3.7 is parallel to z and directed upwards. Referring to Equations (3.32) and (3.33), the DOFs vector $\boldsymbol{U}$ for TUBA3-CE can be written as

$$\begin{aligned}\boldsymbol{U}^T &= \begin{bmatrix} U_1 & U_2 & \dots & U_{18} & U_{19} & \dots & U_{36} \end{bmatrix} \\ &= \begin{bmatrix} w|_1 & \frac{\partial w}{\partial x}|_1 & \dots & \frac{\partial^2 w}{\partial y^2}|_3 & w|_4 & \frac{\partial w}{\partial x}|_4 & \dots & \frac{\partial^2 w}{\partial y^2}|_6 \end{bmatrix}\end{aligned} \tag{3.52}$$

The $\boldsymbol{B}$-matrix is found from the expression of the openings in the three modes. These have first to be written in terms of the vertical displacements and rotations of top and bottom plates. Normal and shearing modes will be treated separately.

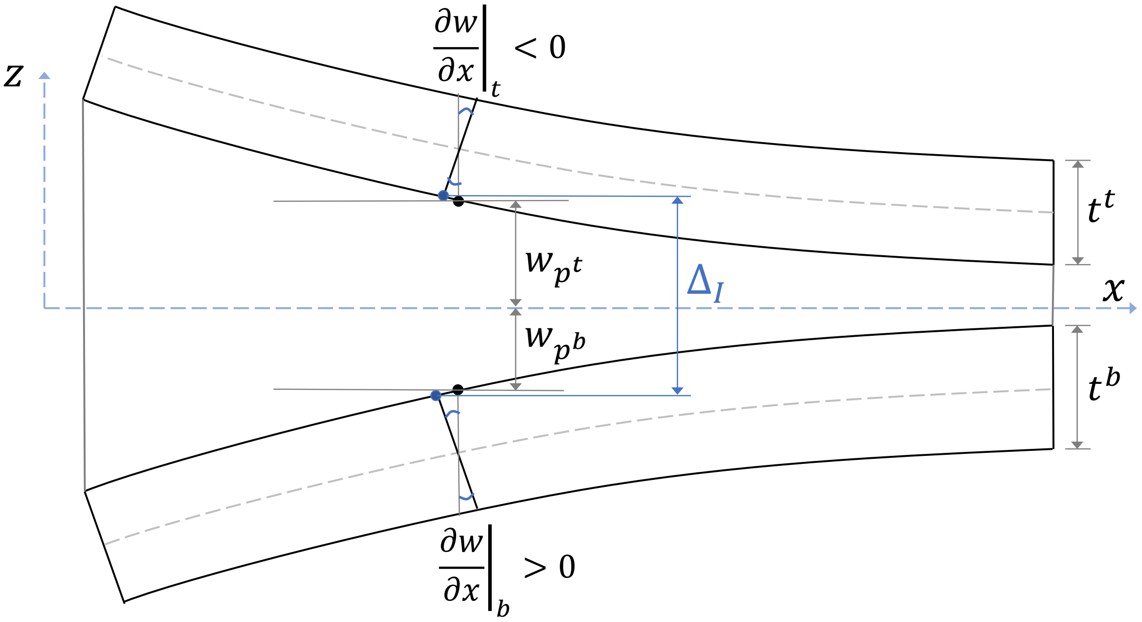

Figure 3.8: Mode I opening. The undeformed CE initially coincides with the x-axis.

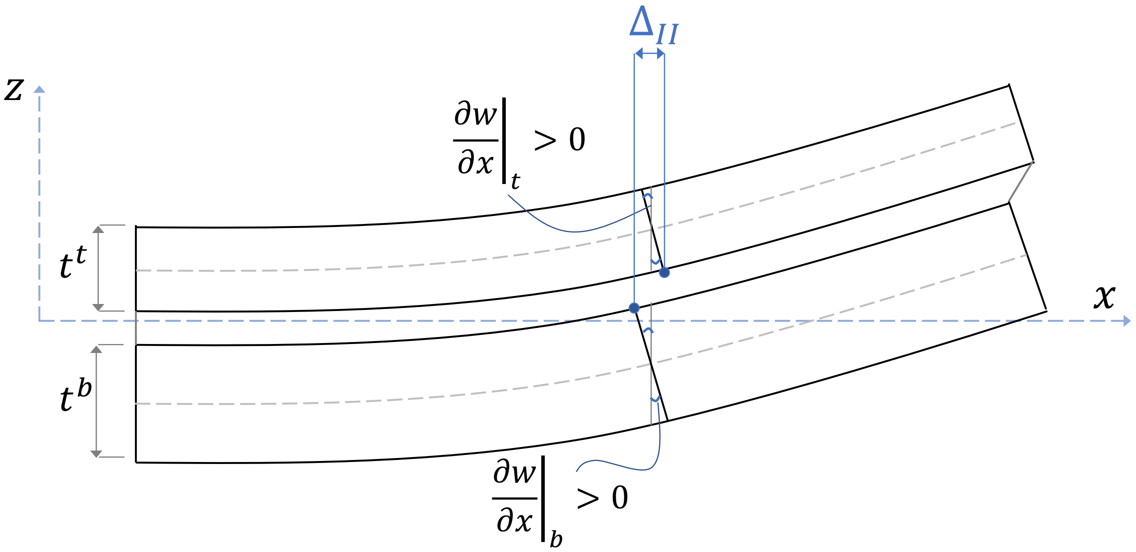

Figure 3.9: Mode II opening. The undeformed CE initially coincides with the x-axis.

A point of coordinates (x, y), or, equivalently, (L_1, L_2, L_3) is considered. Figure 3.8 shows that a rotation $\theta_x = -\partial w/\partial x$ contributes to the vertical displacement of the faces of the CE. However, in a 3D space, also a rotation along y influences w, therefore both angles have to be considered as components of a vector $\boldsymbol{\theta}$. The magnitude of $\boldsymbol{\theta}$ is obtained with the Pythagorean theorem

$$\theta = \sqrt{\theta_x^2 + \theta_y^2} = \sqrt{\left(\frac{\partial w}{\partial x}\right)^2 + \left(\frac{\partial w}{\partial y}\right)^2} \tag{3.53}$$

In the following passages, the indices CE^b, CE^t, p^b, p^t refer to quantities relative respectively to bottom and top CE faces and to the mid-planes of bottom and top plate. The terms t^b and t^t indicate the thicknesses of bottom and top plate. The mode I opening is, by definition

$$\Delta_I = -w_{CE^b} + w_{CE^t} \tag{3.54}$$

where

$$w_{CE^b} = \quad w_{p^b} - \tfrac{t^b}{2}(1 - \cos(\theta)) \tag{3.55}$$

$$w_{CE^t} = \quad w_{p^t} + \tfrac{t^t}{2}(1 - \cos(\theta)) \tag{3.56}$$

Geometrical non-linearities are not accounted for, thus displacements and rotations are assumed to be small. Approximating at the first order

$$1 - cos(\theta) \approx 0$$

The mode I opening is then generated only by the displacement of the substrates mid-planes, hence

$$\Delta_I = -w_{p^b} + w_{p^t} \tag{3.57}$$

Figure 3.9 shows the deformation of TUBA3-CE in pure mode II. Since the TUBA3 plate element only deforms in bending and does not have stretching degrees of freedom, opening in mode II is caused only by the rotations of bottom and top plates. Therefore

$$\Delta_{II} = -u_{CE^b} + u_{CE^t} \tag{3.58}$$

where

$$u_{CE^b} = \quad -\tfrac{t^b}{2}\sin\left(\frac{\partial w_{p^b}}{\partial x}\right) \tag{3.59}$$

$$u_{CE^t} = \quad \tfrac{t^t}{2}\sin\left(\frac{\partial w_{p^t}}{\partial x}\right) \tag{3.60}$$

Assuming small rotations, the sines can be approximated at the first order as

$$\sin\left(\frac{\partial w_{p^b}}{\partial x}\right) \approx \frac{\partial w_{p^b}}{\partial x}$$

$$\sin\left(\frac{\partial w_{p^t}}{\partial x}\right) \approx \frac{\partial w_{p^t}}{\partial x}$$

It follows that Δ_{II} is expressed as

$$\Delta_{II} = \frac{t^b}{2}\frac{\partial w_{p^b}}{\partial x} + \frac{t^t}{2}\frac{\partial w_{p^t}}{\partial x} \tag{3.61}$$

The mode III opening is found from analogous kinematics in the yz-plane. Hence

$$\Delta_{III} = \frac{t^b}{2}\frac{\partial w_{p^b}}{\partial y} + \frac{t^t}{2}\frac{\partial w_{p^t}}{\partial y} \tag{3.62}$$

Equations (3.57), (3.61) and (3.62) can be expressed in terms of the element DOFs. The vector of the degrees of freedom can be written in the form

$$\boldsymbol{U}^T = \begin{bmatrix} \boldsymbol{U}^{\boldsymbol{b}\,T} & \boldsymbol{U}^{\boldsymbol{t}\,T} \end{bmatrix}_{1\times 36} \tag{3.63}$$

which highlights the degrees of freedom belonging respectively to upper and lower face. Recalling Equations (3.34) and (3.57), the mode I opening becomes

$$\Delta_I = -\boldsymbol{N}^T\boldsymbol{U}^{\boldsymbol{b}} + \boldsymbol{N}^T\boldsymbol{U}^{\boldsymbol{t}} = \begin{bmatrix} -[N]^T_{1\times 18} & [N]^T_{1\times 18} \end{bmatrix}\boldsymbol{U} = \boldsymbol{B}_{\boldsymbol{I}}^T\boldsymbol{U} \tag{3.64}$$

The opening in mode II requires the x-derivatives of the shape functions, since

$$\frac{\partial w}{\partial x} = \left[\frac{\partial \boldsymbol{N}}{\partial x}\right]^T \boldsymbol{U} \tag{3.65}$$

The shape functions are expressed in the area coordinates L_1,L_2,L_3, thus the x and y derivatives are computed using the chain rule of differentiation. Recalling Equation (3.27),

$$\left[\frac{\partial \boldsymbol{N}}{\partial x}\right]^T_{1\times 18} = \frac{1}{2A}\begin{bmatrix} b_1 & b_2 & b_3 \end{bmatrix}\begin{bmatrix} \left[\frac{\partial \boldsymbol{N}}{\partial L_1}\right]^T_{1\times 18} \\ \left[\frac{\partial \boldsymbol{N}}{\partial L_2}\right]^T_{1\times 18} \\ \left[\frac{\partial \boldsymbol{N}}{\partial L_3}\right]^T_{1\times 18} \end{bmatrix} \tag{3.66}$$

Once the derivatives in Equation (3.66) are obtained, it is possible to express the mode II opening in terms of the degrees of freedom, as

$$\Delta_{II} = \begin{bmatrix} \frac{t^b}{2}\left[\frac{\partial \boldsymbol{N}}{\partial x}\right]^T & \frac{t^t}{2}\left[\frac{\partial \boldsymbol{N}}{\partial x}\right]^T \end{bmatrix}\boldsymbol{U} = \boldsymbol{B}_{\boldsymbol{II}}^T\boldsymbol{U} \tag{3.67}$$

Starting from eq. (3.62) and deriving with respect to y, the opening in mode III can be written as

$$\Delta_{III} = \begin{bmatrix} \frac{t^b}{2}\left[\frac{\partial \boldsymbol{N}}{\partial y}\right]^T & \frac{t^t}{2}\left[\frac{\partial \boldsymbol{N}}{\partial y}\right]^T \end{bmatrix}\boldsymbol{U} = \boldsymbol{B}_{\boldsymbol{III}}^T\boldsymbol{U} \tag{3.68}$$

where, this time

$$\left[\frac{\partial \boldsymbol{N}}{\partial y}\right]^T_{1\times 18} = \frac{1}{2A}\begin{bmatrix} c_1 & c_2 & c_3 \end{bmatrix}\begin{bmatrix} \left[\frac{\partial \boldsymbol{N}}{\partial L_1}\right]^T_{1\times 18} \\ \left[\frac{\partial \boldsymbol{N}}{\partial L_2}\right]^T_{1\times 18} \\ \left[\frac{\partial \boldsymbol{N}}{\partial L_3}\right]^T_{1\times 18} \end{bmatrix} \tag{3.69}$$

Equations (3.64), (3.67) and (3.68) can be finally assembled together to form the $\boldsymbol{B}$-matrix of TUBA3-CE

$$\begin{bmatrix} \Delta_1 \\ \Delta_2 \\ \Delta_3 \end{bmatrix} = \begin{bmatrix} \boldsymbol{B}_{\boldsymbol{I}}^T \\ \boldsymbol{B}_{\boldsymbol{II}}^T \\ \boldsymbol{B}_{\boldsymbol{III}}^T \end{bmatrix}_{3\times 36} \boldsymbol{U} = \boldsymbol{B}^T\boldsymbol{U} \tag{3.70}$$

3.4.2 TUBA3-CE: constitutive relation

The constitutive matrix of TUBA3-CE is based on of Turòn's model [22], described in Section 2.2.2, restricted, at present, only to mode I loading.

In pure mode I, no separation due to shear occurs between opposite faces of the CE, therefore

$$\Delta_{sh} = 0 \tag{3.71}$$

$$G_{II} = G_{III} = 0 \tag{3.72}$$

from which follows that the mode-mixity ratio B, as defined in Equation (2.18), is also equal to zero. Referring to Equation (2.19), the penalty stiffness K becomes simply

$$K = K_I = 50\frac{E_3}{t} \tag{3.73}$$

In mode I loading, the material damages only due to out-of-plane opening of the faces. Thus, using a bilinear cohesive law and the definitions in Equations (2.27) and (2.28), the damage variable simply is

$$d = \begin{cases} 0 & \text{if } \Delta_I < \Delta_I^0 \\ \frac{\Delta_I^f(\Delta_I - \Delta_I^0)}{\Delta_I(\Delta_I^f - \Delta_I^0)} & \text{if } \Delta_I^0 \leq \Delta_I < \Delta_I^f \\ 1 & \text{if } \Delta_I \geq \Delta_I^f \end{cases} \tag{3.74}$$

Upon substitution in Equation (2.33), Equations (3.73) and (3.74) fully define the constitutive matrix $\boldsymbol{D}$ for TUBA3-CE.

Damage update scheme

A few words are worth to be spent on the damage variable update during the FE analysis. At each call from the solver, user defined elements in Abaqus receive as input an array of state variables (defined as SVARS in the subroutine terminology), which has to be updated throughout the execution of the subroutine and returned as output. In the case of TUBA3-CE, the SVARS array contains the damage values of each integration point both at the last converged increment (LCI) and at the current iteration. In order to avoid a fictitious healing effect, the iterating damage is updated only if higher than the LCI damage. Whenever convergence of the increment is reached for a chosen tolerance, the increment changes and the damage at the last iteration of the previous increment becomes the LCI damage for the new one. Figure 3.10 summarizes the damage update scheme in a flowchart.

3.4.3 TUBA3-CE: stiffness matrix and residuals vector

The element stiffness matrix has the usual form seen in Equations (2.35) and (3.46). The parent domain of TUBA3-CE is the same flat triangle used for TUBA3, thus the two elements share the same coordinates mapping and Jacobian. Referring to the $\boldsymbol{B}$ and $\boldsymbol{D}$ matrices just derived, the matrix $\boldsymbol{K}$ for TUBA3-CE reads

$$\boldsymbol{K} = \int_0^1 \int_0^{1-L_1} \boldsymbol{B}\boldsymbol{D}\boldsymbol{B}^T \det(\boldsymbol{J_L})\, \mathrm{d}L_1\, \mathrm{d}L_2 \tag{3.75}$$

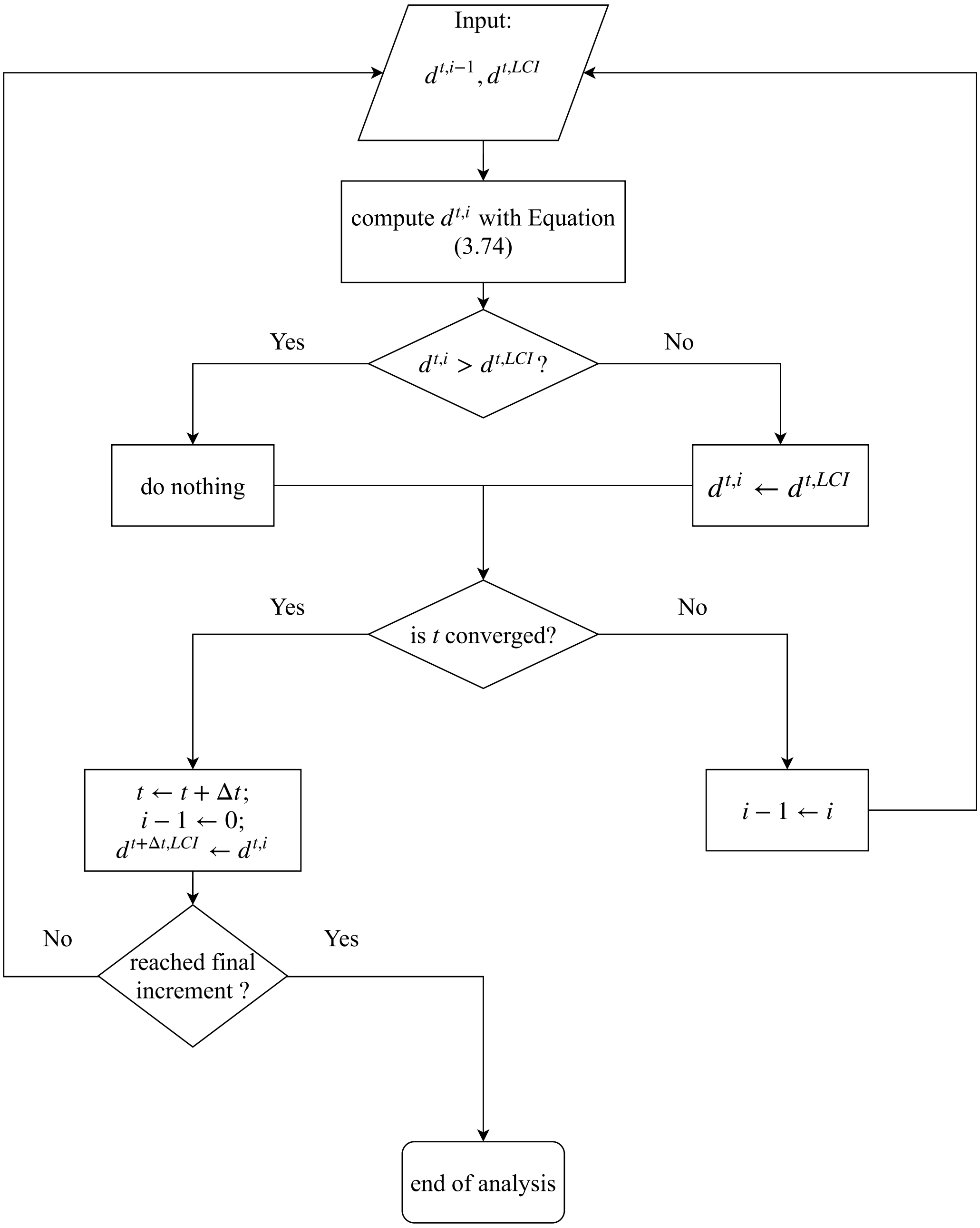

Figure 3.10: Flowchart of the damage update scheme. The index i refers to the iteration number, while t is the time at the current increment.

where

$$\det(\boldsymbol{J_L}) = 2A$$

As seen in Section 2.2.4, if no external loads are considered, the residual vector at every iteration is simply

$$\boldsymbol{f} = -\boldsymbol{KU} \tag{3.76}$$

For the TUBA3 plate element, the integral in Equation (3.75) could be solved analytically, using the Eisenberg-Malvern formula. The same does not always hold for TUBA3-CE. Since the damage variable can change throughout the element's domain, the cohesive element integration does not necessarily reduce to terms such as those in Equation (3.51). Although $\boldsymbol{K}$ could be integrated analytically when the damage is homogeneous, this would require to rewrite $\boldsymbol{B}$ in a form similar to Equation (3.37) and to isolate the Eisenberg-Malvern terms. This operation is error-prone and the final formulation hard to verify, therefore numerical integration was adopted for all TUBA3-CEs, regardless of their damage state. Gaussian quadrature was chosen over the Newton-Cotes scheme, as the former achieves equal degrees of accuracy with fewer integration points.

Numerical integration over triangular domains

Gaussian integration points and weights for 1D integrals can be found in large numbers by extracting the roots of the Legendre polynomial. These same values can be combined in a tensor-product fashion to obtain the IPs coordinates in a quadrilateral domain, where the integration limits for the two parent dimensions do not depend on each other.

Oppositely to lines and quadrilaterals, there is not, at present, an algorithm for determining coordinates and weights for Gaussian IPs over triangles. All the variables required for numerical integration on triangular domains are found on a case-by-case basis, depending on the degree of accuracy required.

The integral of a generic function $g(L_1, L_2)$, defined over the parent triangle $\mathcal{T}_L$, is approximated as [67, 68]

$$\iint_{\mathcal{T}_L} g(L_1,\, L_2)\, \mathrm{d}L_1\, \mathrm{d}L_2 \approx \frac{1}{2} \sum_{i=1}^{N_{IP}} w_i\, g(L_{1,i},\, L_{2,i}) \tag{3.77}$$

where N_{IP} is the overall number of integration points and w_i, $L_{1,i}$, $L_{2,i}$ are respectively the weight and area coordinates of the i^{th} integration point. If $g(L_1, L_2)$ is a polynomial of degree N and the equal sign holds for Equation (3.77), N is then the degree of accuracy of the quadrature formula. Weights and integration points are found imposing (3.77) exactly for each term of the basis of the polynomial space $\boldsymbol{\mathcal{P}}_N$, defined as

$$\boldsymbol{\mathcal{P}}_N = \mathbf{span}\{L_1^p\, L_2^q;\;\; p,\, q \geq 0,\; p + q \leq N\} \tag{3.78}$$

Since

$$\dim(\boldsymbol{\mathcal{P}}_N) = \frac{(N+1)(N+2)}{2}$$

the number of (coupled) equations to be solved rapidly increases for increasing degrees of accuracy.

In literature, several works focused on finding precise estimates of w_i, $L_{1,i}$, $L_{2,i}$ for Gaussian quadrature of degrees up to 20 [68–72]. The values used in this research were taken from the paper of Cowper [68].

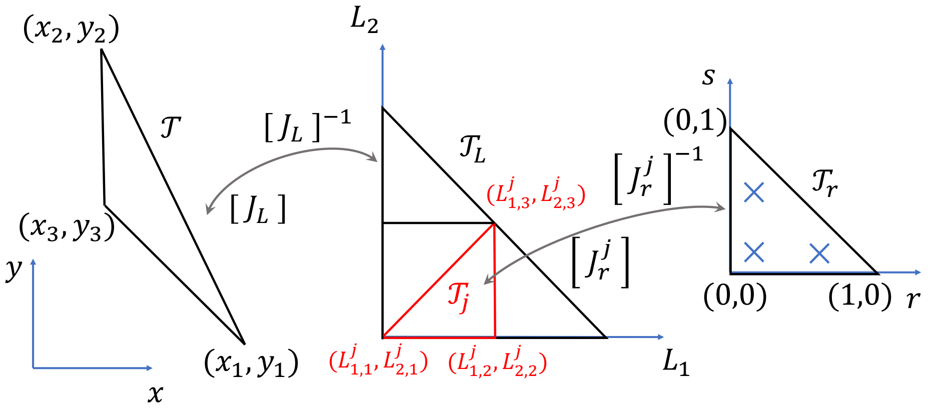

Figure 3.11: Different mappings between physical and parent domains. A function over each sub-triangle in the L-domain can be integrated through Gaussian quadrature in the r-domain. Generic IPs in the r-domain are highlighted.

Sub-domain integration

Large cohesive elements show highly non-linear stress and damage distributions, when crossed by the cohesive zone. If these elements are given an insufficient number of integration points, the FE solution can be sensitive to instabilities and the Newton-Raphson procedure may diverge.

An easy way to increase the density of IPs, that does not require the knowledge of formulas for high degrees of quadrature accuracy, is to use a sub-domain integration scheme. The idea is to split the integral over the parent domain of coordinates L_1, L_2, L_3 (from now on called the *L-domain*) in multiple integrals over N_{sd} sub-triangles. Each of these sub-triangles or sub-domains is then integrated with Gaussian quadrature over a third domain of coordinates r,s,t, named the *r-domain*. Figure 3.11 shows the three different domains (physical, L-domain, r-domain), the partition in sub-triangles and the location of three Gaussian IPs in the r-domain.

The additive property allows to write the integral over $\mathcal{T}_L$ as the sum of the integrals over a set of sub-triangles $\mathcal{T}_j$ as follows

$$\iint_{\mathcal{T}_L} g(L_1,\, L_2)\,\mathrm{d}L_1\,\mathrm{d}L_2 = \sum_{j=1}^{N_{sd}} \iint_{\mathcal{T}_j} g(L_1^j,\, L_2^j)\,\mathrm{d}L_1\,\mathrm{d}L_2 \tag{3.79}$$

The mapping between $\mathcal{T}_j$ and $\mathcal{T}_L$ is defined as

$$\begin{cases} L_1^j &= r\,L^j_{1,1} + s\,L^j_{1,2} + t\,L^j_{1,3} \\ L_2^j &= r\,L^j_{2,1} + s\,L^j_{2,2} + t\,L^j_{2,3} \\ 1 &= r + s + t \end{cases} \tag{3.80}$$

In Equation (3.80), the notation $L^j_{m,n}$ indicates the m^{th} area coordinate of the n^{th} vertex of the j^{th} sub-triangle in the L-domain. By comparison of Equations (3.26) and (3.80) it is evident how the above mapping is again a linear transformation in area coordinates, just like the one between the physical domain and the L-domain. It follows that the Jacobian for the $L - r$ mapping is

$$\boldsymbol{J^j_r} = \begin{bmatrix} \frac{\partial L^j_1}{\partial r} & \frac{\partial L^j_1}{\partial s} \\ \frac{\partial L^j_2}{\partial r} & \frac{\partial L^j_2}{\partial s} \end{bmatrix} = \begin{bmatrix} L^j_{1,1} - L^j_{1,3} & L^j_{1,2} - L^j_{1,3} \\ L^j_{2,1} - L^j_{2,3} & L^j_{2,2} - L^j_{2,3} \end{bmatrix} \tag{3.81}$$

The determinant of $\boldsymbol{J^j_r}$ is then

$$\det(\boldsymbol{J^j_r}) = (L^j_{1,1} - L^j_{1,3})(L^j_{2,2} - L^j_{2,3}) - (L^j_{2,1} - L^j_{2,3})(L^j_{1,2} - L^j_{1,3}) = 2A_{\mathcal{T}_j} \tag{3.82}$$

The integral over the triangle $\mathcal{T}_j$ can now be performed in the r-domain as

$$\iint_{\mathcal{T}_j} g(L^j_1,\, L^j_2)\,\mathrm{d}L_1\,\mathrm{d}L_2 = \iint_{\mathcal{T}_r} g(L^j_1(r,s),\, L^j_2(r,s))\det(\boldsymbol{J^j_r})\,\mathrm{d}s\,\mathrm{d}r \tag{3.83}$$

Equation (3.83) can be integrated numerically via Gaussian quadrature with N_{IP} integration points, hence

$$\iint_{\mathcal{T}_r} g(L^j_1(r,s),\, L^j_2(r,s))\det\boldsymbol{J^j_r}\,\mathrm{d}s\,\mathrm{d}r = \frac{1}{2}\sum_{i=1}^{N_{IP}} w_i\, g(L^j_1(r_i,s_i),\, L^j_2(r_i,s_i))\det(\boldsymbol{J^j_r}) \tag{3.84}$$

The integral over the entire parent triangle $\mathcal{T}_L$ is given by the contribution of all the sub-triangles $\mathcal{T}_j$ and reads

$$\iint_{\mathcal{T}_L} g(L_1,\, L_2)\,\mathrm{d}L_1\,\mathrm{d}L_2 = \frac{1}{2}\sum_{j=1}^{N_{sd}}\sum_{i=1}^{N_{IP}} w_i\, g(L^j_1(r_i,s_i),\, L^j_2(r_i,s_i))\det(\boldsymbol{J^j_r}) \tag{3.85}$$

It must be remembered that, although each sub-triangle is integrated with a Gaussian scheme over the r-domain, the overall set of $N_{sd} \times N_{IP}$ integration points over the L-domain is not Gaussian. Also, the above integration method must not be confused with the namesake devised by Yang *et al.* and presented in Section 2.3.2. Here, the domain is divided into a fixed number of sub-domains and the IPs weights and coordinates are fixed, while in Yang's scheme, the motion of the level set during the increments constantly redefines all these quantities.

Chapter 4

Verification

Before using the implemented elements in delamination analyses, these were verified with benchmark problems of known analytical solutions.

The TUBA3 plate was tested for some simple plate bending examples, keeping small displacements and rotations (linear kinematics). At first, a square plate of isotropic material was considered, constrained with different edge conditions and subject either to a uniform pressure or a point load. These verification examples were taken by the founding paper of Bell [57]. The analytical deflections and moments, used as references, were either derived or taken from the book of Timoshenko and Woinowsky-Krieger [73]. Afterwards, the TUBA3 element was assigned a unidirectional (UD) composite section and UD plates in cantilever and three-point-bending configurations were considered. Both these examples have geometries with large aspect ratios, so that, for verification purposes, the plate's deflection could be approximated with that of an Euler-Bernoulli beam, having the same composite section.

A cohesive element is generally verified by including it in models for pure and mixed mode loading conditions. This was done for mode I and the results are given in Chapter 5, discussing the method's validation. The present chapter discusses instead a simple uniaxial traction test of a single CE. The aim in this case was to check if the resulting stress-opening curve would match the bilinear cohesive law.

The contents of this chapter are organized as follows. First the TUBA3 plate verification is discussed, starting from the square isotropic plate examples and proceeding with the UD composite problems. A second section covers the testing of TUBA3-CE.

4.1 Plate element verification

Before digging into the verification cases proposed, a comment is necessary on the use of TUBA3 in finite element models. A sensitive aspect of all TUBA meshes is the enforcement of the boundary conditions (BCs). In contrast to conventional FE shells in fact, TUBA elements possess the second derivatives of w among their degrees of freedom, which may or

Material			
Young's modulus	E	71.7	GPa
Poisson's ratio	ν	0.3	
Geometry			
Edge length	L	150	mm
Thickness	t	10	mm

Table 4.1: Material and geometry data for the isotropic plate examples.

may not be constrained for edge nodes. For instance, in case of free edges, the moments acting along the axes of these edges have to be zero. In thin plate theory, the second derivatives of the displacement field correspond to the plate curvatures, on which the moments directly depend. It follows that appropriate relations between the $\partial^2 w/\partial x^2$, $\partial^2 w/\partial y^2$ and $\partial^2 w/\partial x\,\partial y$ degrees of freedom have to be imposed to enforce conditions such as the free edge one. Appendix C discusses the problem in more detail and reports the DOFs constrained for every TUBA3 example in this chapter.

4.1.1 Isotropic plate

For this set of analyses, a square plate with the geometrical and material properties reported in Table 4.1 was considered. All the cases discussed, shown in Figure 4.1, are symmetric in loading, geometry and boundary conditions (BCs). Therefore, the analyses could be restricted to only a quarter of the plate, provided that the symmetric BCs had been correctly imposed. Also, each problem was studied for a series of increasingly refined meshes (A1 to A4 and B), illustrated in Appendix C.

Simply supported plate with uniform pressure load

The transverse displacement w of a simply-supported plate subject to a uniform pressure load can be obtained with the Navier method. The idea is to write both $w(x, y)$ and the load $q(x, y)$ as eigenfunction series having the same basis terms, but different coefficients. Using the orthogonality of the sine and cosine functions, the load coefficients are obtained, which can be substituted in the equilibrium equation to solve for the coefficients of w. The bending and twisting moments are found by means of Equations (3.17) and (3.18).

Mesh convergence is studied monitoring the errors relative to the analytical solution for displacement, bending and twisting moments. The first two are probed at the center point of the plate, while the twisting moment is considered at the origin. The series expressions for the above quantities, in case of a square plate, are given by the followings

$$w\left(\frac{L}{2}, \frac{L}{2}\right) = \frac{16q}{\pi^6 D} \sum_{m=1}^{M} \sum_{n=1}^{N} \frac{1}{mn\left(\frac{m^2+n^2}{L^2}\right)^2} \sin\left(m\frac{\pi}{2}\right) \sin\left(n\frac{\pi}{2}\right) \tag{4.1}$$

$$M_{xx}\left(\frac{L}{2}, \frac{L}{2}\right) = M_{yy}\left(\frac{L}{2}, \frac{L}{2}\right) = \frac{16q}{\pi^4} \sum_{m=1}^{M} \sum_{n=1}^{N} \frac{\left(\frac{m^2+\nu n^2}{L^2}\right)}{mn\left(\frac{m^2+n^2}{L^2}\right)^2} \sin\left(m\frac{\pi}{2}\right) \sin\left(n\frac{\pi}{2}\right) \tag{4.2}$$

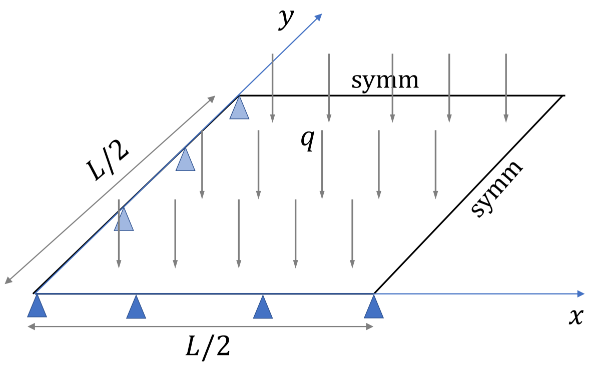

(a) Simply supported, uniform pressure load.

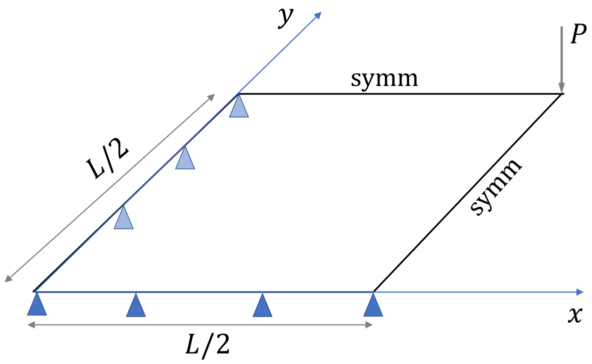

(b) Simply supported, point load.

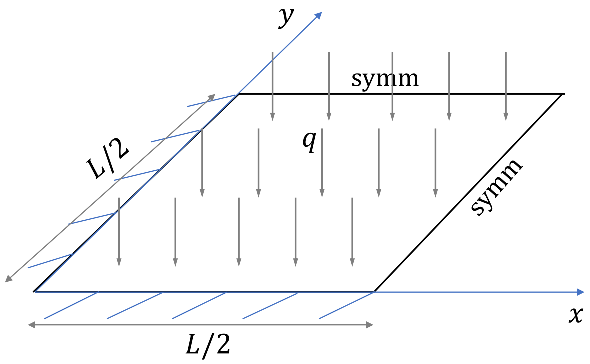

(c) Clamped, uniform pressure load.

Figure 4.1: Isotropic plate: loads and boundary conditions.

Mesh	$w\left(\frac{L}{2},\frac{L}{2}\right)$ (mm)	err%	$M_{xx}\left(\frac{L}{2},\frac{L}{2}\right)$ (Nmm/mm)	err%	$M_{xy}\left(0,0\right)$ (Nmm/mm)	err%
A1	-1.5776	0.74	-5.500E+03	2.09	3.467E+03	5.06
A2	-1.5663	0.01	-5.390E+03	0.04	3.604E+03	1.31
A3	-1.5661	0.00	-5.388E+03	0.00	3.631E+03	0.57
A4	-1.5661	0.00	-5.387E+03	0.00	3.641E+03	0.30
Analytical sol.	-1.5661		-5.388E+03		3.652E+03	

Table 4.2: Results and relative errors for the simply supported isotropic plate with uniform pressure load.

$$M_{xy}\left(0,0\right) = -\frac{16(1-\nu)q}{\pi^4 L^2}\sum_{m=1}^{M}\sum_{n=1}^{N}\frac{1}{\left(\frac{m^2+n^2}{L^2}\right)^2} \tag{4.3}$$

where q = -5 N/mm^2 is the load magnitude, m and n are the eigenfrequency indices and D is the plate's bending stiffness, expressed as

$$D = \frac{Et^3}{12(1-\nu^2)}$$

The analytical values for this benchmark case are presented in the last row of Table 4.2 and were found implementing Equations (4.1) to (4.3) as Matlab scripts and summing the first 15 terms of the series in both directions ($M = N = 15$).

Table 4.2 also reports the results for the four meshes considered. The relative percent error indicate good agreement with the analytical solution already from the two element mesh (A1). Moreover, the error in the center displacement monotonically decreases upon mesh refinement. It is interesting to notice how the twisting moment at the origin converges more slowly than the other quantities. Indicative in this sense is the comparison between TUBA3 and TUBA6 made by Bell in [57], where the same problem and meshes are studied. The convergence of M_{xy} for TUBA3 is not as rapid as for TUBA6 and this is likely due to the TUBA3 requirement of a cubic normal derivative along the edges. Because of this constraint the TUBA3 edges can deflect less than the inner region, thus coarse meshes can steer the displacement away from the mesh lines, causing spurious twisting stiffness or compliance.

Simply supported plate with center load

A simply supported plate is considered again, this time with a concentrated force applied at its center. The analytical center displacement can be found in [73] and reads

$$w\left(\frac{L}{2},\frac{L}{2}\right) = \alpha\frac{PL^2}{D} \tag{4.4}$$

where α = 0.0116 for a square plate and P = -30 kN is the applied load. According to the thin plate theory, in case a point load is applied, the moments become singular at the

Mesh	$w\left(\frac{L}{2},\frac{L}{2}\right)$ (mm)	err%	$M_{xy}(0,0)$ (Nmm/mm)	$M_{xy}(0,0)$ in [57] (Nmm/mm)	err%
A1	-1.15966	2.76	1.94726E+03	1.94730E+03	0.0021
A2	-1.18559	0.58	1.84546E+03	1.84560E+03	0.0076
A3	-1.18949	0.25	1.83105E+03	1.83120E+03	0.0082
A4	-1.19085	0.14	1.82930E+03	1.82910E+03	0.0109
B	-1.19212	0.03	1.82444E+03	1.82430E+03	0.0077
Analytical sol.	-1.19252				

Table 4.3: Results and relative errors for the simply supported isotropic plate with center load.

center of the plate and analytical expressions can be found only redistributing the load over a surrounding circular region. Due to the arbitrariness of such an approach, the center moments convergence was not studied. The origin twisting moments were instead computed for each mesh and compared with the values in [57].

Table 4.3 contains the TUBA3 results and analytical references for the two quantities analyzed. The center deflection converges again monotonically to the analytical value. In case the mesh is refined towards the plate's center, as with mesh B, the percent error becomes minimal. Close agreement is also reached between the M_{xy} values obtained and the reference ones. The small differences between the two sets of results are numerical and likely related to the fact that Bell's formulation of TUBA3 requires matrix inversion. This introduces a numerical error that does not affect the element implementation of this work.

Clamped plate with uniform pressure load

The isotropic rectangular clamped plate with uniform loading is discussed in [73], considering several aspect ratios. In case of edges of equal lengths, the expressions of the center deflection, bending moments at the plate's center and bending moments the edges midpoints are, respectively

$$w\left(\frac{L}{2},\frac{L}{2}\right) = 0.00126\frac{qL^4}{D} \tag{4.5}$$

$$M_{xx}\left(\frac{L}{2},\frac{L}{2}\right) = M_{yy}\left(\frac{L}{2},\frac{L}{2}\right) = 0.0231qL^4 \tag{4.6}$$

$$M_{xx}\left(0,\frac{L}{2}\right) = M_{yy}\left(\frac{L}{2},0\right) = -0.0513qL^4 \tag{4.7}$$

where q = -5 N/mm^2.

The analytical values from Equations (4.5) to (4.7) are compared with the TUBA3 results in Table 4.4. Considering the center displacement, the error is kept under 2% in all cases, except for the 2 element mesh (A1). The TUBA6 elements used in [57] for the same problem and mesh score a deviation of just 1.1%. This indicates again the TUBA3 requirement of a cubic normal derivative along the edges visibly affects the global deflection, if coarse meshes are used. Such an observation also explains why the edge bending moments are largely inaccurate for the A1 mesh case. The bending moment at the plate's center seem to deviate from the 'correct' value, when more elements are added. However, the analytical solutions in Table 4.4 derives from the truncation of a series expression and the authors of [73], from which these references are taken, state that they are up to 1% inaccurate, compared to a series expansion with more terms. It is then questionable whether the analytical solution considered can be used as reference below this threshold . Finally, for meshes A2 to A4, edge moments are all predicted with less than 2% deviation from the reference.

4.1.2 Unidirectional composite plate

Given that a DCB unidirectional composite specimen is studied for the model validation, it made sense to test a UD version of TUBA3 in a cantilever plate configuration. Moreover, inspired by the ENF test, a three point bending UD plate was also considered for verification purposes. Material properties and geometry for both examples were taken from [74] and, for the DCB case, they are the same as used in Chapter 5.

Changing the plate section from isotropic to UD composite required to modify the $\boldsymbol{D}$-matrix of TUBA3. In case of a unidirectional stacking sequence, the constitutive relation of each ply in laminate axes is the same regardless of the out-of-plane coordinate. This allows to write $\boldsymbol{D}$ as

$$\boldsymbol{D_{UD}} = \frac{1}{12} t^3 \boldsymbol{C_{ply}} \tag{4.8}$$

where $\boldsymbol{C_{ply}}$ is the stiffness matrix of a ply in a fibre-oriented reference frame and reads

$$\boldsymbol{C_{ply}} = \frac{1}{1-\nu_{xy}\,\nu_{yx}} \begin{bmatrix} E_x & \nu_{xy}\,E_y & 0 \\ \nu_{yx}\,E_x & E_y & 0 \\ 0 & 0 & G_{xy} \end{bmatrix} \tag{4.9}$$

In Equation (4.9), E_x and E_y are the Young's moduli parallel and perpendicular to the fibers and ν_{xy} is the Poisson's ratio expressing the strain in the y-direction due to a load in the x-direction. The coefficient ν_{yx} has opposite meaning than ν_{xy} and the two can be related by the Maxwell relation

$$\nu_{xy}\,E_y = \nu_{yx}\,E_x \tag{4.10}$$

from which follows the symmetry of $\boldsymbol{C_{ply}}$. G_{xy} is the in-plane shear modulus.

Mesh	$\boldsymbol{w\left(\frac{L}{2},\frac{L}{2}\right)}$ (mm)	**err%**	$\boldsymbol{M_{xx}\left(\frac{L}{2},\frac{L}{2}\right)}$ (Nmm/mm)	**err%**	$\boldsymbol{M_{xx}\left(0,\frac{L}{2}\right)}$ (Nmm/mm)	**err%**
A1	-4.5226E-01	6.893	-2.575E+03	0.897	4.546E+03	21.226
A2	-4.9312E-01	1.518	-2.599E+03	0.003	5.677E+03	1.631
A3	-4.9022E-01	0.921	-2.585E+03	0.530	5.880E+03	1.881
A4	-4.8891E-01	0.651	-2.580E+03	0.712	5.8462E+03	1.299
Analytical sol.	-4.86E-01		-2.599E+03		5.771E+03	

Table 4.4: Results and relative errors for the clamped isotropic plate with uniform pressure load.

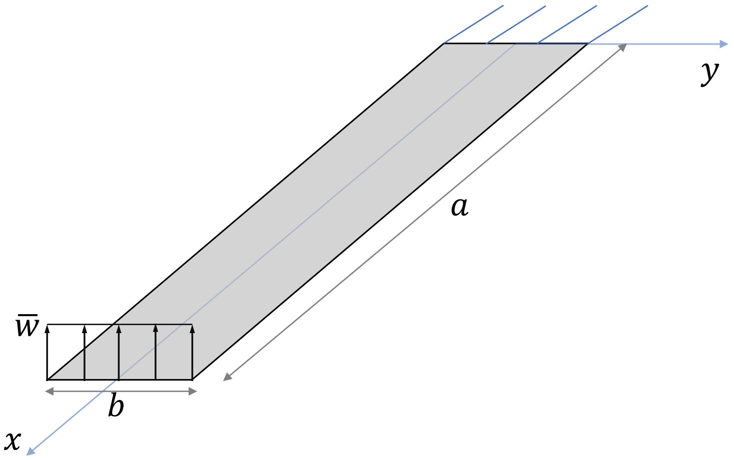

Figure 4.2: Cantilever UD composite plate with imposed displacement at the tip.

Material		T300/1076	
Young's modulus, x-direction	E_{xx}	139.4	GPa
Young's modulus, y-direction	E_{yy}	10.16	GPa
Poisson's ratio	ν_{xy}	0.3	
In-plane shear modulus	G_{xy}	4.6	GPa
Geometry			
Length	a	150	mm
Width	b	10	mm
Thickness	t	3	mm

Table 4.5: Material and geometry data for the cantilever UD plate example.

The reference values for these tests were obtained by approximating the deflection of the UD plate with that of an Euler-Bernoulli beam. This simplification was justified by the geometry of the specimens considered, which show an order of magnitude difference between length and width. Plate's thickness and width were used as beam section dimensions and E_x as the longitudinal modulus.

Cantilever plate

A representation of the problem is given in Figure 4.2, while the material and geometrical properties are reported in Table 4.5. The specimen is symmetric with respect to the x axis, so only half of it is considered for the numerical model. Loading is performed in displacement control.

The reference solution for this problem is obtained considering a cantilever beam of length a and moment of inertia

$$I_b = \frac{1}{12} b\, t^3$$

and bending modulus

$$E_b = E_{xx}$$

Mesh	**Total force at $x = a$** (N)	**err%**
A1	12.540	0.323
A2	12.531	0.250
A3	12.527	0.216
A4	12.528	0.227
Analytical sol.	12.500	

Table 4.6: Results and relative errors for the cantilever UD plate example.

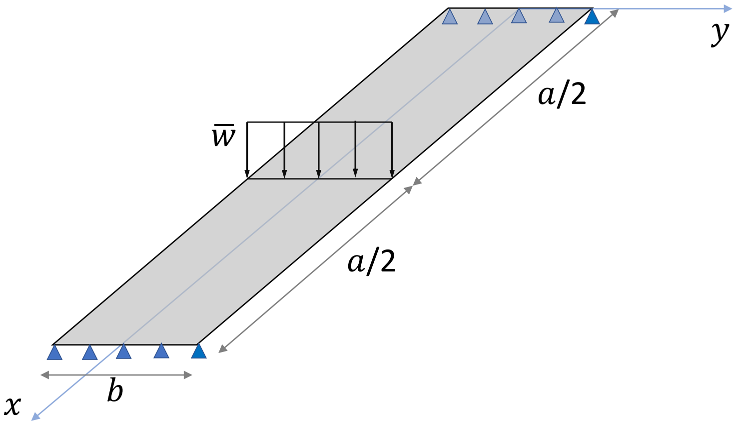

Figure 4.3: UD composite plate in three point bending loading with imposed displacement.

Given an imposed displacement $\overline{w}$ = 3.587 mm at the free tip, the beam's reaction force at the same location is

$$F_b = \frac{3E_b I_b}{a^3} \overline{w} = 25 \text{ N} \tag{4.11}$$

Table 4.6 contains the tip reaction forces obtained with meshes of increasing elements density. Both numerical results and analytical reference are reported as half of the total values, since only half of the problem is considered. Looking at the percent relative deviations, it is evident that all the meshes examined provide results in close agreement with the analytical solution.

Three point bending plate

The three point bending setup is shown in Figure 4.3, while Table 4.7 presents the material and geometrical data. The problem presents two symmetries, with respect to the x-axis and to a plane orthogonal to x, cutting the plate at half of its length. This allows to consider only a quarter of the specimen. Also in this case, the structure is loaded by an imposed displacement ($\overline{w}$).

The Euler-Bernoulli beam theory provides again the analytical reference. Considering the expressions for I_b and E_b used in the previous example and an applied deflection $\overline{w}$ = -0.179

Material		IM7/8852	
Young's modulus, x-direction	E_{xx}	161.0	GPa
Young's modulus, y-direction	E_{yy}	11.38	GPa
Poisson's ratio	ν_{xy}	0.32	
In-plane shear modulus	G_{xy}	5.2	GPa
Geometry			
Length	a	101.6	mm
Width	b	25.4	mm
Thickness	t	4.5	mm

Table 4.7: Material and geometry data for the three point bending UD plate example.

Mesh	**Total force at $x = \frac{a}{2}$** (N)	**err%**
A1	-63.640	0.220
A2	-63.558	0.091
A3	-63.522	0.035
A4	-63.847	0.547
Analytical sol.	-63.500	

Table 4.8: Results for the three point bending UD plate example.

mm, the reaction force at $x = a/2$ is

$$F_b = \frac{48 E_b \, I_b}{a^3} \, \overline{w} = \text{-254 N} \tag{4.12}$$

The total reaction forces obtained with TUBA3 elements are reported in Table 4.8, together with the reference solution and the relative deviations. All the force values are $\frac{1}{4}$ of the actual ones, as the double symmetry of the problem allowed to analyze only the reduced model. Also for the three point bending case, the errors relative to the analytical value are all less than 1%. Interesting is, however, the increase in percent deviation in the last refinement step. Whereas going from mesh A1 to A3, elements were increased only along the longitudinal direction, A4 was built adding a nodal line along the width. This allowed the TUBA3 mesh to deform more like a plate than in the other cases, increasing the discrepancy with respect to the beam idealization.

4.2 Cohesive element verification

Testing of TUBA3-CE was done performing a simple analysis, involving just one element. The boundary conditions and loading are schematized in Figure 4.4. The cohesive element was loaded uniaxially and all the degrees of freedom were constrained, except for the out-of-plane displacement w of nodes 4,5 and 6. A velocity of 0.0113 mm/s was applied for a total step time of 1 s, resulting in an overall displacement $\bar{w} = 0.0113$ mm. This value corresponds

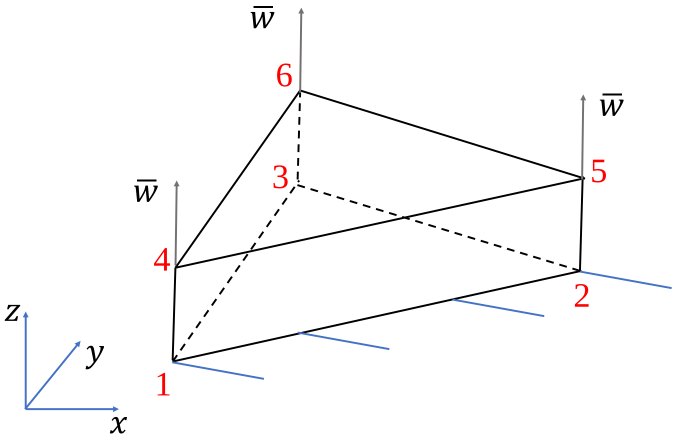

Figure 4.4: TUBA3-CE subject to uniaxial loading along z.

Material		T300/1076	
Young's modulus, z-direction	E_{zz}	139.4	GPa
Fracture toughness	$G_{I,c}$	0.170	kJ/m^2
Material strength	τ_I^0	30	MPa
Penalty stiffness	K	169333	MPa/mm

Table 4.9: Material data for the cohesive element under uniaxial loading.

to the failure opening for an interface loaded in pure mode I, as found by using the bilinear law relation

$$\bar{w} = \Delta_I^f = \frac{2G_{I,c}}{\tau_I^0}$$

The incremental-iterative analysis was performed using the Full Newton-Raphson method. Stiffness, strength and fracture toughness of the material are reported in Table 4.9, along with the penalty stiffness used. Observing Figure 4.5, it is noticed how the stress distribution from the analysis correctly reproduces the cohesive law. Figure 4.6 shows instead the damage values for an increasing opening Δ_I. From the TUBA3-CE analysis, the value of the opening at damage onset (Δ_I^0) was found to be between $1.60 \cdot 10^{-4}$ mm and $2.46 \cdot 10^{-4}$ mm, in agreement with the analytical value of $1.77 \cdot 10^{-4}$ mm, given by Equation (2.27).

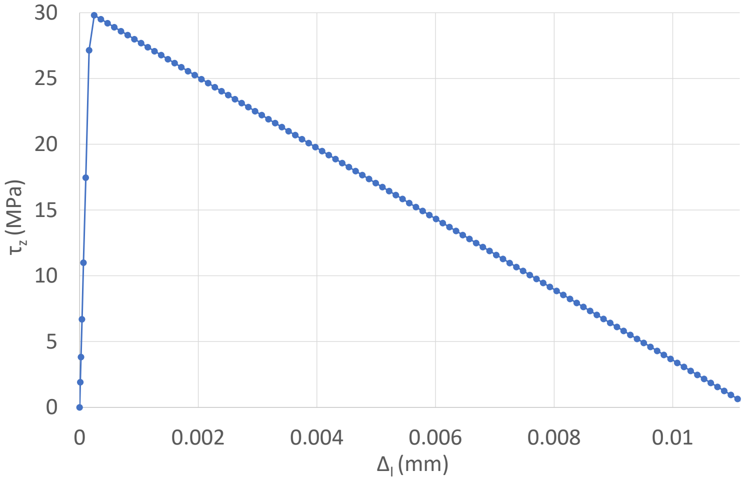

Figure 4.5: Out-of-plane stress vs. mode I opening for the TUBA3-CE uniaxial test.

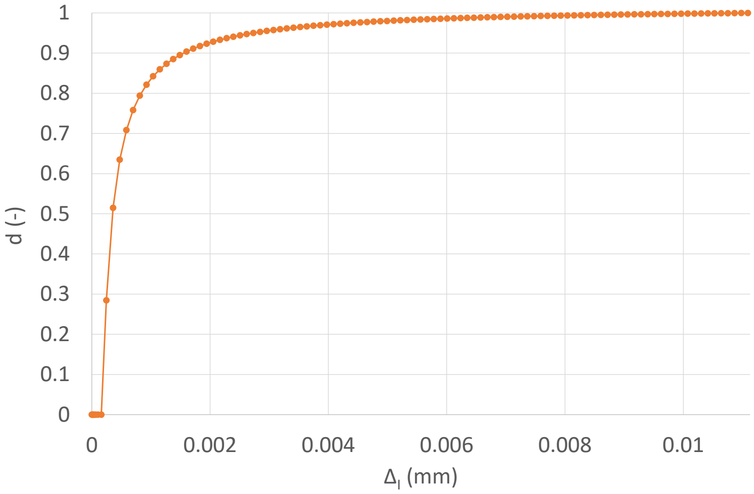

Figure 4.6: Damage vs. mode I opening for the TUBA3-CE uniaxial test.

Chapter 5

Validation

In order to assess the accuracy and performance of the proposed method, the assembly of TUBA3 and TUBA3-CE was tested in a classical fracture mechanics experiment. This was chosen to be the mode I DCB specimen suggested by Kreuger in [74]. The benchmark solution provided in this work and the analytical curve obtained with the Corrected Beam Theory were used as references for the numerical results in this chapter.

Up to present, the TUBA3 framework for delamination modelling has been tested for mode I fracture only. The reason for this is twofold. First, mode I loading usually introduces cohesive zones smaller than those of other mode mixities. Consequently, this scenario is the most critical in terms of limit element size. Also, the TUBA3 method has yet to be extended to mode II and mixed mode. The reason for this will be given in more detail in Chapter 6. For now it suffices to say that an extension beyond mode I requires the implementation of geometrical non-linear kinematics for the CE and the introduction of membrane DOFs for both TUBA3 and TUBA3-CE.

This chapter provides the results of the validation tests and comments them in detail. Initially, the benchmark DCB specimen is described and its geometrical and material data are given. Afterwards, the Abaqus model used for comparison is detailed and its output shown and discussed, emphasizing the element size required to achieve the converged reference solution. Finally the results of the TUBA3 simulations in terms of load-displacement curves, stress and damage distributions are presented and compared with the reference.

5.1 Benchmark problem

The DCB specimen is portrayed in Figure 5.1 in its undeformed configuration. The dimensions of the specimen and the initial crack size are shown, as well as the boundary conditions and applied loading velocity of the numerical model. The laminate is unidirectional with 24 plies of T300/1076 graphite-epoxy prepreg. Table 5.1 summarizes the values of geometrical and material quantities.

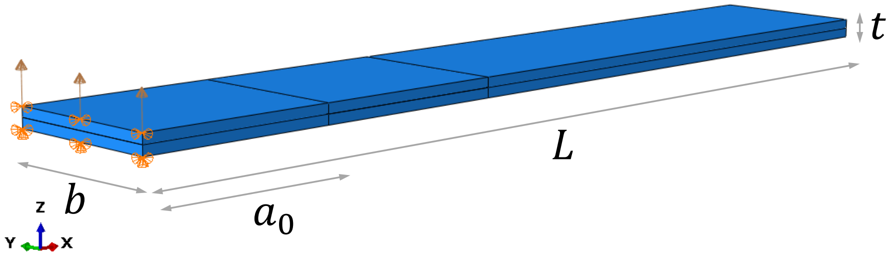

Figure 5.1: DCB specimen: geometry, loading and boundary conditions.

Material		T300/1076	
Young's moduli	E_{xx}	139.4	GPa
	E_{yy}	10.16	GPa
	E_{zz}	10.16	GPa
Poisson's ratios	ν_{xy}	0.3	
	ν_{xz}	0.3	
	ν_{yz}	0.436	
Shear moduli	G_{xy}	4.6	GPa
	G_{xz}	4.6	GPa
	G_{yz}	3.54	GPa
Fracture toughnesses	$G_{I,c}$	0.170	kJ/m^2
	$G_{II,c}$	0.494	kJ/m^2
Material strengths	τ_I^0	30	MPa
	τ_{II}^0	50	MPa
B-K coefficient	η	1.62	
Geometry			
Length	L	150	mm
Width	b	25	mm
Thickness	t	3	mm
Precrack length	a_0	30.5	mm

Table 5.1: DCB specimen: geometry and material data.

Knowing thickness and material parameters, it is possible to use Equations (2.38) and (2.40) to estimate the cohesive zone length. In the assumption of an infinite and slender body respectively, the analytical CZL values are

$$l_{cz,I}^{\infty} = \frac{E_{zz}\, G_{I,c}}{(\tau_I^0)^2} = 1.92 \text{ mm} \tag{5.1}$$

$$l_{cz,I}^{0} = (l_{cz,I}^{\infty})^{\frac{1}{4}} \left(\frac{t}{2}\right)^{\frac{3}{4}} = 1.60 \text{ mm} \tag{5.2}$$

where M_I^{∞} and M_I^0 are taken equal to one.

A more accurate estimate of the CZL was found from an Abaqus analysis using standard cohesive contact and a very fine mesh in the crack propagation region. For this sake, a 2D model could be extracted as the middle section of the specimen along the x-direction, as the fibers are all oriented along this axis. 2D incompatible mode plane strain elements (Abaqus CPE4I) were used for the substrates. The stress and damage profiles obtained from the simulation have been shown in Figure 2.11, when discussing the mesh density constraint. In particular, identification of the x-coordinates bounding the values of the damage variable between 0 and 1 allowed to obtain the following CZL estimate:

$$l_{cz,I}^{num} = 0.875 \text{ mm} \tag{5.3}$$

This value will be referred to as the *numerical cohesive zone length* in the discussion to follow.

5.2 Reference solution

The creation of a reference for validation purposes required two distinct phases. The first one, common to all FE procedures, was to create the numerical model or *preprocessing*, setting all the analysis parameters. After that, a mesh sensitivity study was performed, until convergence of the load-displacement curve. The results obtained with the converged mesh were used as reference for validating the proposed mehtod.

5.2.1 Description of the numerical model

The following gives an overview of the main modeling choices and features adopted in building the Abaqus reference model. This description does not mean to be complete and the full set of parameters used is given in Appendix D.

The entire preprocessing phase was carried out in Abaqus CAE. The model consists of two parts, corresponding to the two sublaminates. Only the bottom part/sublaminate was modelled directly, while the top one was created as an exact copy. The two parts were then stacked together at the assembly level. A partition as shown in Figure 5.1 was done to isolate the crack propagation region, which required a mesh finer than for the rest of the specimen. The substrates were assigned a composite layup property with the material data provided in Table 5.1. Since the laminate is unidirectional, a single ply with half the laminate's thickness could be assigned to be the layup of each part. The element type was chosen as the linearly interpolated brick element with incompatible modes or C3D8I, in Abaqus nomenclature.

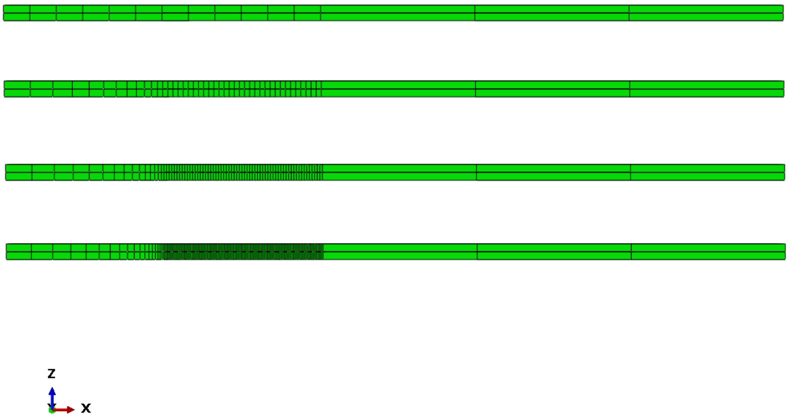

Figure 5.2: Four meshes of different element sizes in the crack propagation region. The lengths are, from top to bottom: 5mm, 1 mm, 0.5 mm and 0.25 mm.

The cohesive interface was modeled by defining cohesive contact between the two adjacent substrate surfaces, that extend from the end of the precrack to the end of the specimen. If the interface is thin and can be defined in terms only of a traction-separation law, CC can be used in place of CEs and it usually offers improved computational performances [75]. The quadratic criterion [76] was used for damage initiation and the B-K relation as crack propagation condition. In order to avoid numerical instabilities during the fracture process, a viscosity coefficient η_v was determined and set equal to 10^{-5} s. This value was found sufficient for a stable solution and small enough not to pollute it with spurious damping.

All the analyses were run with a Full Newton Raphson method for a total time of 2 s. The boundary conditions for the reference analyses constrained the translations in all directions for the bottom left edge of the specimen and in the x and y directions for the top left one, as presented in Figure 5.1. Loading of the specimen was done imposing a velocity of 2mm/s on the top left edge.

5.2.2 Mesh convergence study

Using the model just detailed, four different mesh sizes were studied. These are represented in Figure 5.2 for a section view in the xz-plane. In all three cases, 1 element was used along the thickness direction and 25 elements covered the width. The meshes differed only for the elements size used in the fracture region, respectively of 5, 1, 0.5 and 0.25 mm.

Figure 5.3 shows the load-displacement curves for the four meshes discussed. These are plotted together with the analytical solution derived from the Corrected Beam Theory (CBT), summarized in Appendix E. The coarsest mesh of 5 mm misses the limit point completely, as no material damage occurs before reaching a load of 160 N. When the element size is reduced to 1 mm, the peak force is still overpredicted by 15% the CBT value. The overshoot reduces to 2.6% when the 0.5 mm case is considered, although this mesh is not yet converged, as seen from the spurious unstable crack growth phase after the limit load. The finest mesh

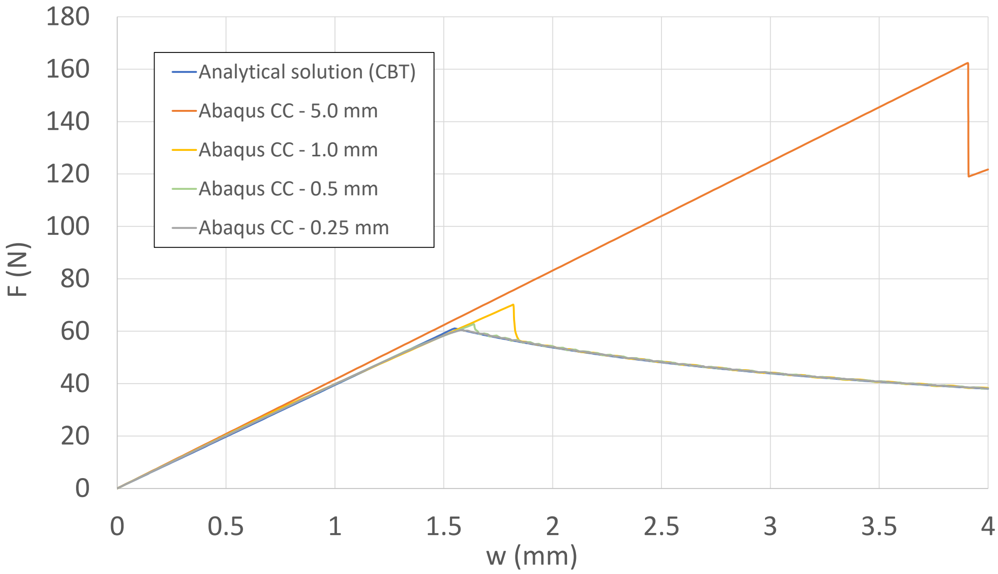

Figure 5.3: DCB test results obtained using the Abaqus reference model for four different mesh sizes. The Corrected Beam Theory solution is also plotted.

of 0.25 mm does not show any fictitious load release at the critical point and practically overlaps the analytical curve. The critical load and displacement for this element size are respectively 60.5 N and 1.59 mm and are in close agreement with the values presented in [74] for the same DCB specimen. Therefore the 0.25 mm mesh for the Abaqus CC model can be considered converged, reason why it was taken as the reference solution for the subsequent model validation.

5.3 Comparison with proposed method

The TUBA3 models were generated following a different approach with respect to the Abaqus CC ones. First, a planar shell in a 3D space, corresponding to the bottom arm of the specimen, was created in Abaqus CAE and meshed for the required element size. An incomplete input file was produced and read from a Matlab program implemented by the author, that would write nodal coordinates and connectivity for both top arm and cohesive elements.

The scripts for computing the stiffness matrix and residuals vector for both TUBA3 and TUBA3-CE had to be included in a single element subroutine, which could execute the code for the correct element based on a key passed by the Abaqus processor. The user element properties for each of the elements included the material data, thickness, and, in case of TUBA3-CE a binary flag variable, indicating whether the cohesive element had been placed or not in the precracked region. In the former case, the pertaining damage variable was set equal to one, else equal to zero.

Referring to Figure 5.4, the left edge of the bottom plate was simply supported, thus the out-of-plane displacement and the derivative along the edge were constrained. The latter

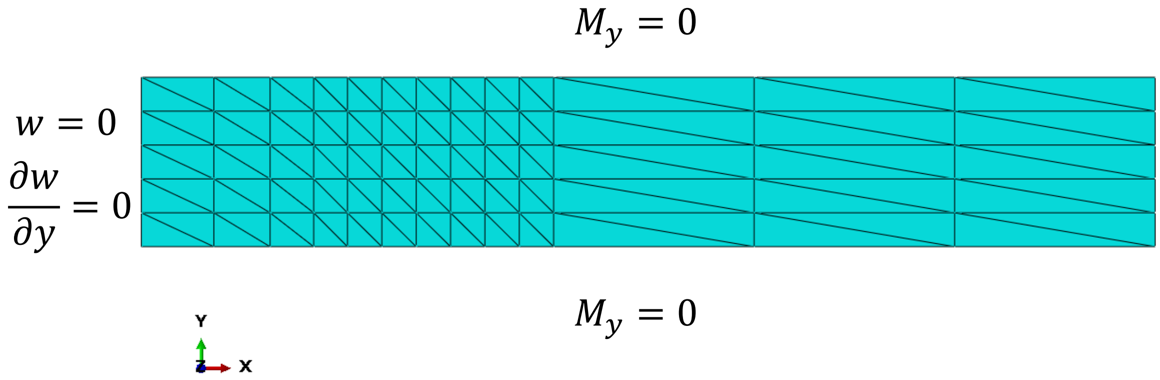

Figure 5.4: TUBA3 mesh and boundary conditions of the DCB bottom substrate.

variable was set to zero also for the left edge of the top plate, so to keep the edge straight during deformation. Also, the free edge condition ($M_y = 0$) was enforced on the nodes of both longitudinal edges for bottom and top plate.

As did in the CC models, the analyses were carried out with the Full Newton-Raphson method for a total time of 2 s, during which a velocity of 2 mm/s was kept on the top left edge of the specimen.

5.3.1 Load-displacement curves

Figure 5.5 shows the DCB load-displacement curves obtained from the TUBA3 simulations. Results for four different element lengths are plotted together with the Abaqus reference solution. The simulations for mesh dimensions of 1, 2 and 5 mm achieved convergence and produced results in close agreement with the reference ones throughout the entire loading. Moreover, despite the quite severe oscillations during propagation, also the 10 mm mesh predicted the critical load and displacement with reasonable accuracy.

To assess the presence of the mesh density constraint, the ratio between element size and cohesive zone length is considered. In case of a 10 mm mesh, the elements in the crack propagation region are more than 5 times larger than the analytical CZL values in Section 5.1 and the ratio increases to 11 upon comparison with the numerical CZL. This suggests an almost insensitivity of the TUBA3 elements to the MDC, as they can accurately reproduce the curvatures of the thin sublaminates even with lengths much higher than the CZL.

More quantitative measures of the accuracy reached with the new elements are given in Table 5.2. The 1, 2 and 5 mm meshes all managed to predict the critical load with at most 3% error and the coarsest mesh model did not go over a 5.47% deviation. Slightly worse precision

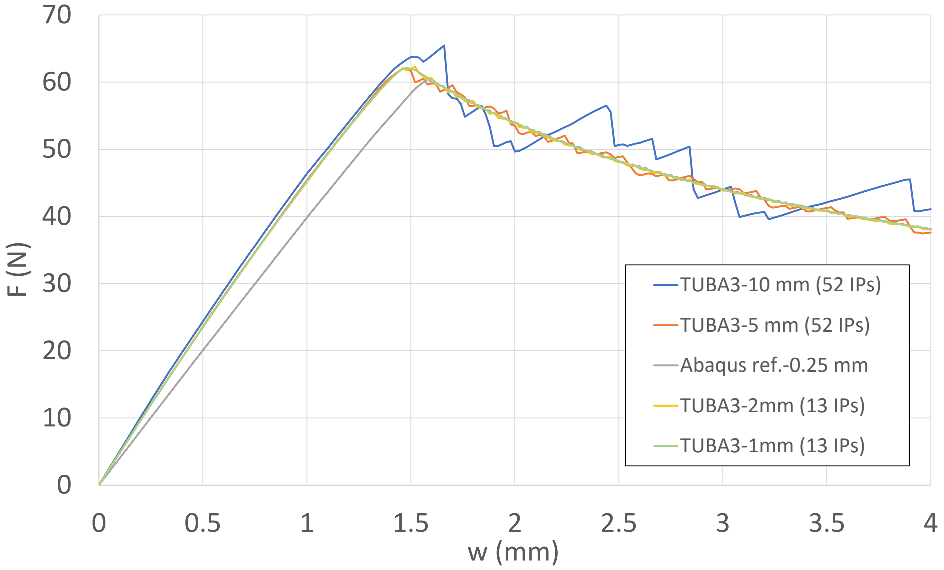

Figure 5.5: DCB load-displacement curves obtained with TUBA3 elements. Results for four different mesh sizes are plotted.

Model	F_c (N)	**err%**	w_c (mm)	**err%**
1 mm, 13 IPs	62.13	2.73	1.48	6.62
2 mm, 13 IPs	62.31	3.02	1.52	4.10
5 mm, 52 IPs	61.97	2.47	1.46	7.89
10 mm, 52 IPs	63.78	5.47	1.52	4.10
Abaqus ref.	60.48		1.59	

Table 5.2: Critical loads and displacements for TUBA3 DCB models of different mesh sizes. Abaqus reference solution and relative deviations are also reported.

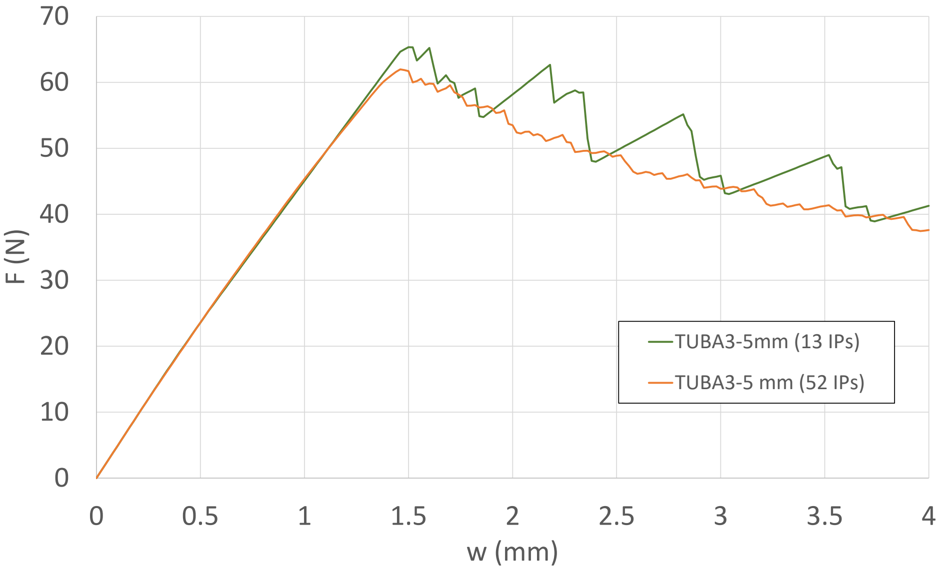

Figure 5.6: DCB load-displacement curves obtained with 5 mm TUBA3 elements. Curves for two different numbers of integration points are plotted.

was obtained on the critical displacements, whose error ranges from 4% to almost 8%. This discrepancy is linked to the difference in the initial stiffness between the TUBA3 and reference models, observed in Figure 5.5. It must be remembered in fact, that TUBA3 elements can only work in bending, whereas the C3D8I elements used for the reference can also shear in the xz, yz-planes and deform out of plane. Therefore during elastic loading, before opening of the cohesive interface, the TUBA3 solution is stiffer than the C3D8I model, as the latter displaces further due to transverse shearing of the substrates. Also, the lack of out-of-plane straining for plates translates in a premature opening of the CE, since all the bending stresses transmitted through the interface work to open it, without any stretching of the sublaminates. This means that the limit opening will be reached prior than when continuum elements (s.a. C3D8I) are used.

The discrepancies just described would likely become more evident for larger substrate thicknesses. In this case the linear stiffness mismatch would increase since the Kirchhoff assumption neglects the even bigger transverse shear deformations. Also, the limit point would shift, as thicker substrates would mean higher out-of-plane elongations, still not captured by a plate model.

A further point of attention concerns the number of integration points necessary to avoid instabilities or loss of convergence after damage. Figure 5.6 compares the load-displacement curves for two meshes of 5 mm element length in the fracture region. The CEs were given 13 integration points in one case and 52 in the other one. The subdomain integration procedure described in Section 3.4.3 easily allowed to increase the number of IPs for each TUBA3-CE. Most noticeably, the curve corresponding to the lower IPs density results in spurious oscillations when the crack front is propagating. In fact, at every iteration of the analysis some of the integration points transition from an intact to a debonded state, removing part of the total stiffness. If few integration points are present, the failure of one of them causes a large stiffness loss, explaining the staggered profile in Figure 5.6. Moreover, if the first line of integration points is too distant from the precrack front, these reach the failure opening Δ_I^f at a higher applied load than that found using more IPs. As observed in Figure 5.6, the limit force is in fact higher in the 13 IPs case than when 52 IPs are used. In quantitative terms, the 52 IPs solution overpredicts the critical load by 2.47% its reference value, while the 13 IPs one misses it by more than 8%.

It could be argued that reducing the number of cohesive elements at the cost of adding integration points would hinder the efficiency of the method. However, an increase in elements ultimately enlarges the dimensions of the FE linear system of equations and the global stiffness matrix requires more processing time to be inverted. On the opposite, using more IPs only results in a higher number of iterations of the code portions that build the element stiffness matrix and residual vector. This phase of the analysis can be made less computationally involved through a lean programming practice and seldom requires the processing effort introduced by large models. A more quantitative discussion on the computational performances is offered in Section 5.3.4, which compares the CPU times of TUBA3 and reference models.

5.3.2 Stress and damage profiles

The out-of-plane stresses and damage for the DCB specimen obtained with the 2 mm and 1 mm TUBA3 meshes are reported in Figures 5.7 and 5.8. Both these variables were computed for the CEs in the cohesive zone length at 4 mm opening of the specimen arms. The plots were produced with a Python program that would read the values of τ_I and d at the barycentric integration point of a line of triangles. In particular the elements were chosen as equidistant from the specimen's longitudinal sides, in order to avoid edge effects.

Both graphs show the characteristic trends observed in the crack front region of a DCB specimen. From left to right, the interface is initially fully separated, hence no tractions are present and $d = 1$. Proceeding further, the stresses increase and the damage variable decreases, identifying the beginning of the cohesive zone. The value of the material strength (30 MPa) is reached at the crack tip, where the material is intact. Immediately ahead of this region, negative stresses first arise to restore the interface equilibrium and then further assess to a zero plateau, where both arms of the specimen are still undeformed.

Figures 5.9 and 5.10 compare stresses and damage in three different cases. Two of the curves plotted were obtained with 2D and 3D Abaqus CC models, respectively with 0.0125 and 0.25 mm element lengths, while the third one refers to the 1 mm TUBA3 model. Again, in order to avoid the edges influence, damage and stresses in Abaqus CC case were sampled in a succession of nodes equidistant from the longitudinal sides of the specimen.

It is evident that the 0.25 mm Abaqus solution can be considered converged also in terms of stresses and damage, since the two fields match almost entirely the ones from the 2D analysis. The same does not hold for the TUBA3 models, which show visible deviations from the Abaqus CC results. As previously discussed, in fact, when plate elements are used as substrates, the out-of-plane stresses at the interface can only deform the cohesive elements, which will open more than if they were included between solid elements. This explains why stress and damage start departing sooner from their plateau in the TUBA3 case than for the CC models, when going from an entirely damaged state to an intact one. As a consequence,

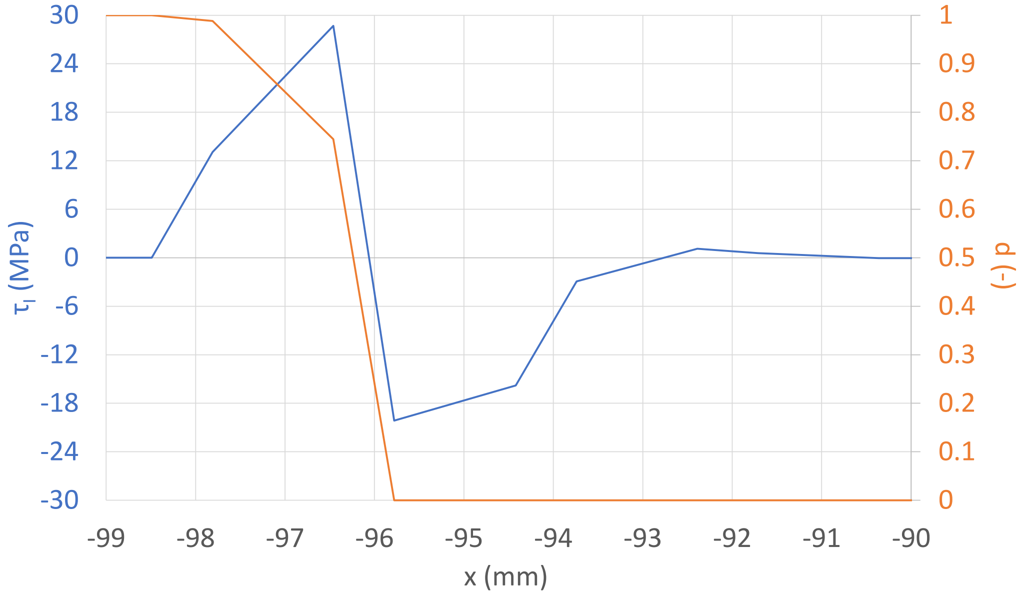

Figure 5.7: Stress and damage profiles in the cohesive zone of the DCB specimen. TUBA3 and TUBA3-CEs are used with a 2 mm size in the crack region and 13 integration points per element.

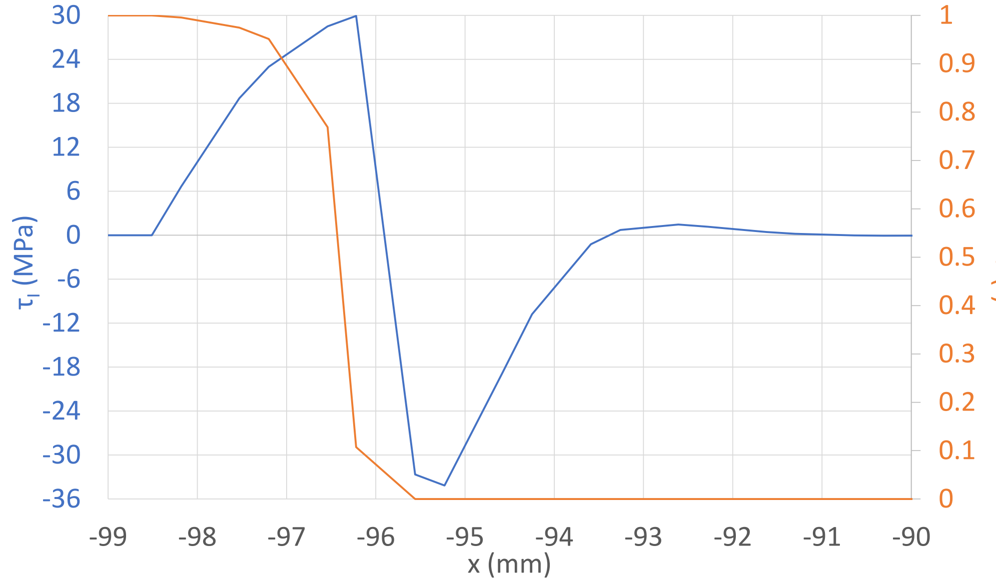

Figure 5.8: Stress and damage profiles in the cohesive zone of the DCB specimen. TUBA3 and TUBA3-CEs are used with 1 mm size in the crack region and 13 integration points per element.

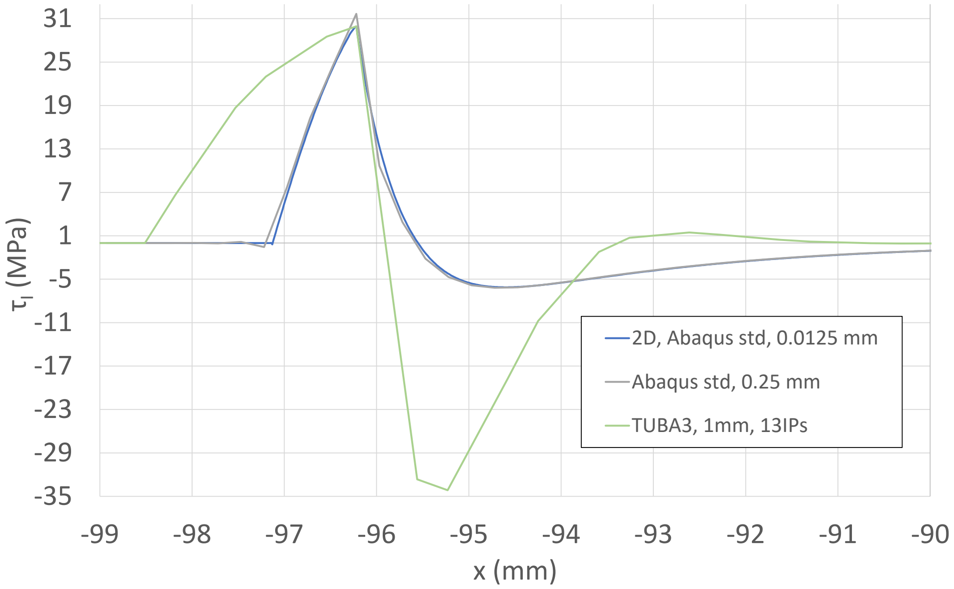

Figure 5.9: Comparison of stress profiles for different models and mesh sizes.

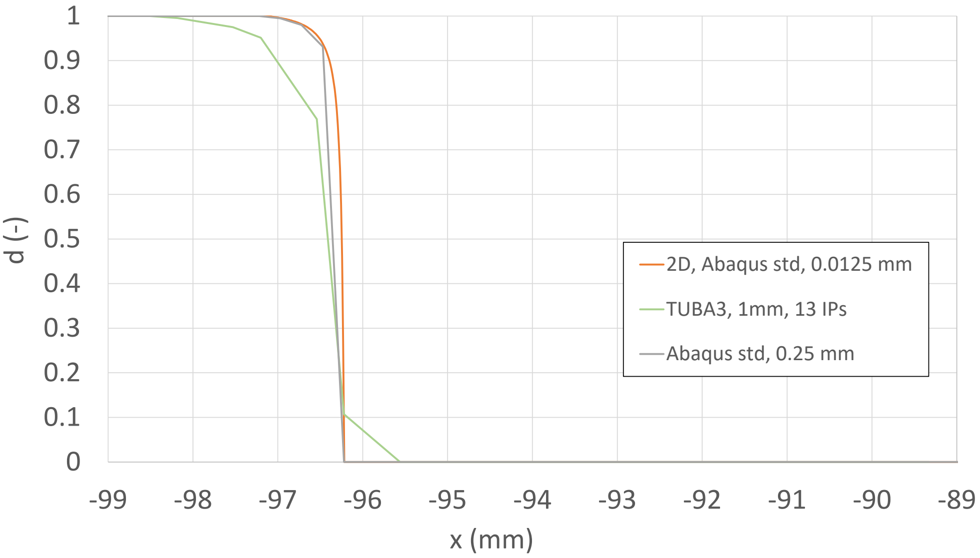

Figure 5.10: Comparison of damage profiles for different models and mesh sizes.

the length of the cohesive zone predicted in case of plate substrates is larger than the reference numerical value in Equation (5.3). In the 1 mm TUBA3 case, the CZL value is found to be

$$l_{cz,I}^{TUBA3} = 1.96 \text{ mm} \tag{5.4}$$

Although the value in Equation (5.4) would probably change using a finer mesh or sampling the damage variable in more integration points, it is likely that big variations from this measure would not be observed. In fact, stress and damage profiles of TUBA3-CEs are affected by the systematic error introduced by the kinematics of the plate substrates. The relative insensitivity of the CZL estimate to the element's size can be observed comparing Figure 5.7 for the 2 mm mesh case and Figure 5.8 for 1 mm. The region in which the damage variable ranges between 0 and 1 has nearly the same length for both meshes.

Again looking at Figure 5.9, another relevant difference between Abaqus CC and TUBA3 is the extent of the compression region and the stress magnitudes therein. Also in this case the discrepancy is due to the impossibility of plate elements to deform along their thickness. As soon as the crack is closed and the material is intact, the mid-planes of the plates come in contact and try to interpenetrate. This is almost entirely prevented by the large penalty stiffness, at the cost of generating high negative stresses. No alleviation of this effect comes from the compression of the substrates along their thickness, oppositely to what happens with solid elements. The reduced length of the compressive region in the TUBA3 model, as well as the mild positive stresses generating afterwards are necessary to maintain the overall equilibrium of the interface to vertical translation and rotation.

Despite the differences in stress and damage profiles between solid and plate-compatible CEs, even very fine meshes of solid elements cannot reproduce the real stress distribution. The numerical stresses depend in fact on the choice of the cohesive law that, although being shaped by experimental material parameters and physical considerations, is ultimately a choice of the analyst.

5.3.3 Damage maps

The 2D interface damage distribution at final separation of the specimen's arms is shown in Figure 5.11. This plot was obtained from the Abaqus CC model with 0.25 mm mesh. Looking at the cohesive zone (green to white coloured) it is clear how small this is with respect to the structural dimensions. It can be noticed how the crack front, represented by the transition between the failed material (red) and the intact one (blue) appears straight for almost the entire width of the specimen, except at its edges. This characteristic shape, known as 'thumb nail', is a well-known feature of pure mode I fracture observed both experimentally and numerically. During bending, the bonded surfaces of the substrates are both under tension, thus the Poisson's effect induces their compression in the direction orthogonal to the propagation one. This induces opposite curvatures for the two surfaces, closing the interface at the edges and delaying damage in these regions.

The damage maps for the TUBA3 models could also be produced by postprocessing the FE results with a Python program. The results are shown in Figures 5.12 to 5.15 for the same element sizes and number of IPs previously discussed. It is evident how finer meshes and higher number of integration points can smooth the damage distribution. The thumbnail shape becomes evident in the 1 mm and 2 mm cases and it can be compared with

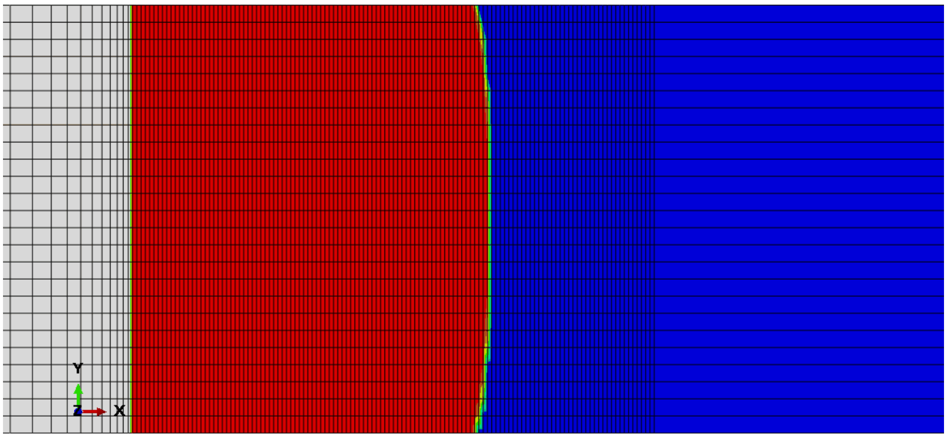

Figure 5.11: Damage distribution for the Abaqus CC model with 0.25 mm mesh at 4.0 mm opening of the DCB loaded edge.

the reference in Figure 5.11. Moreover, besides differences in graphical interpolations, the damage distributions for standard CEs or CC appear staggered in the cohesive zone. In this case in fact, the elements cannot be partially debonded, since they are integrated with four Newton-Cotes nodes at the corners of their parent domain [13]. TUBA3-CEs do not suffer from this limitation, since they can completely contain the cohesive zone, hence be only partially damaged. This feature allows for more continuous transition regions between intact and debonded material.

A numerical anomaly is noticed in the 10 mm case. The damage map for this mesh shows 'damage spots' ahead of the crack front, where instead the material should be intact. A possible explanation is found observing the crack fronts for the meshes presented. All the damage maps show some 'crests' in the variation of d along y. The repetition of these crests seems periodic, with the period depending on the element's y-dimension. As previously discussed, the TUBA3 plate is allowed less deflection at its edges than in the rest of its domain (see Section 3.3.1). In case of large elements, this feature alters the stiffness of the structure depending on the directionality of the mesh. However, coarse meshes can still provide accurate damage maps if a large number of integration points is used. In this case the damage would still be sampled finely, reducing the magnitude of the crests. This is confirmed by comparison of the damage map for 5 mm and 52 IPs (Figure 5.13) and that for the same mesh size and 13 IPs (Figure 5.16).

5.3.4 Computational performances

The final comparison between the TUBA3 models and the Abaqus CC solution concerns the performance parameters for the DCB simulations, reported in Table 5.3. It is evident how even the most involved TUBA3 simulation manages to cut the CPU times of Abaqus CC of by an order of magnitude. Particularly impressive from a computational effort perspective is the saving obtained by running the 5 mm, 52 IPs simulation, still 97% accurate on the limit load, as compared to the Abaqus CC, 0.25 mm case. The TUBA3 model achieves a 94.3% reduction of the CPU time, an improvement similar to that scored by Russo in [44,56] for the

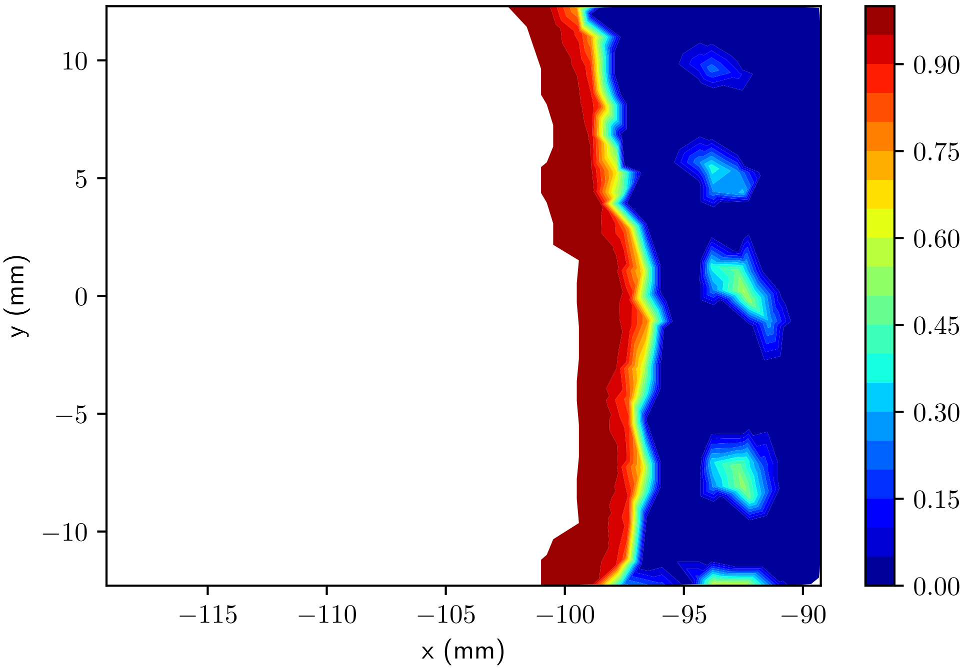

Figure 5.12: TUBA3 model: damage distribution at 4.0 mm opening. Mesh size: 10 mm, 52 integration points.

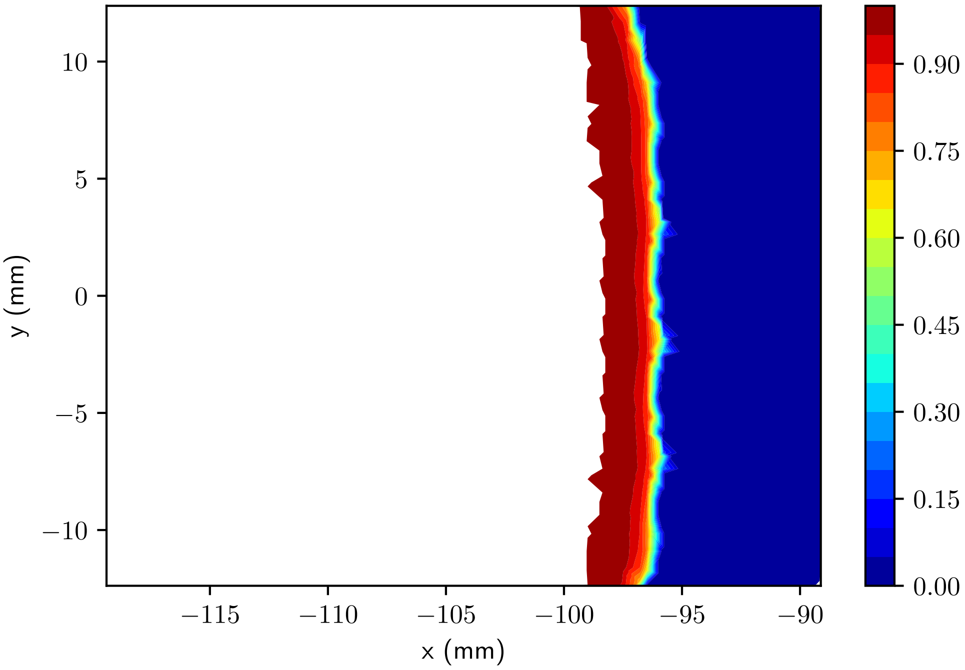

Figure 5.13: TUBA3 model: damage distribution at 4.0 mm opening. Mesh size: 5 mm, 52 integration points.

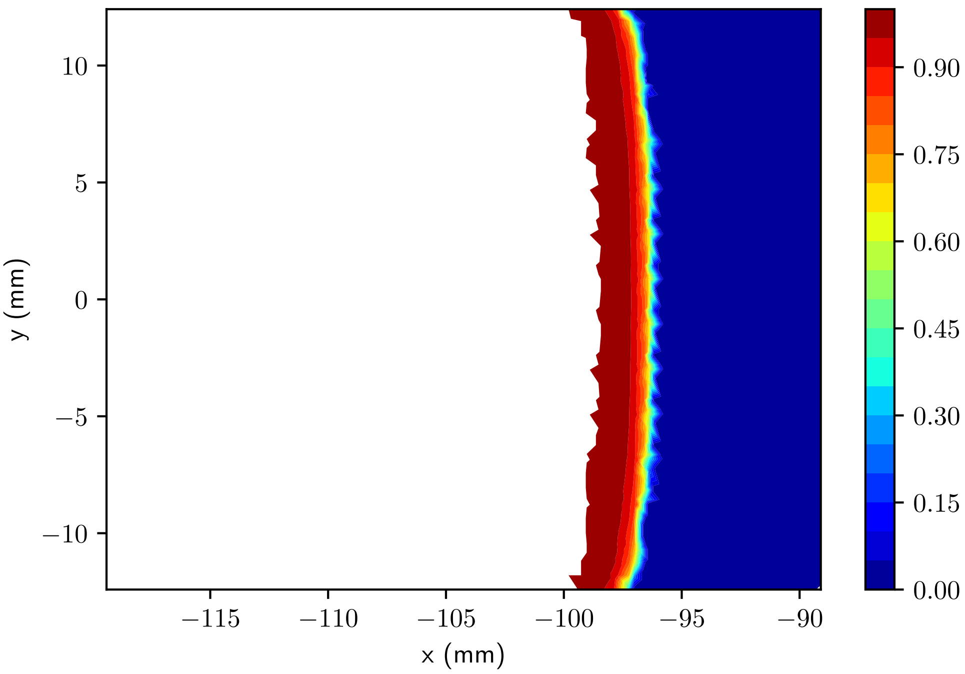

Figure 5.14: TUBA3 model: damage distribution at 4.0 mm opening. Mesh size: 2 mm, 13 integration points.

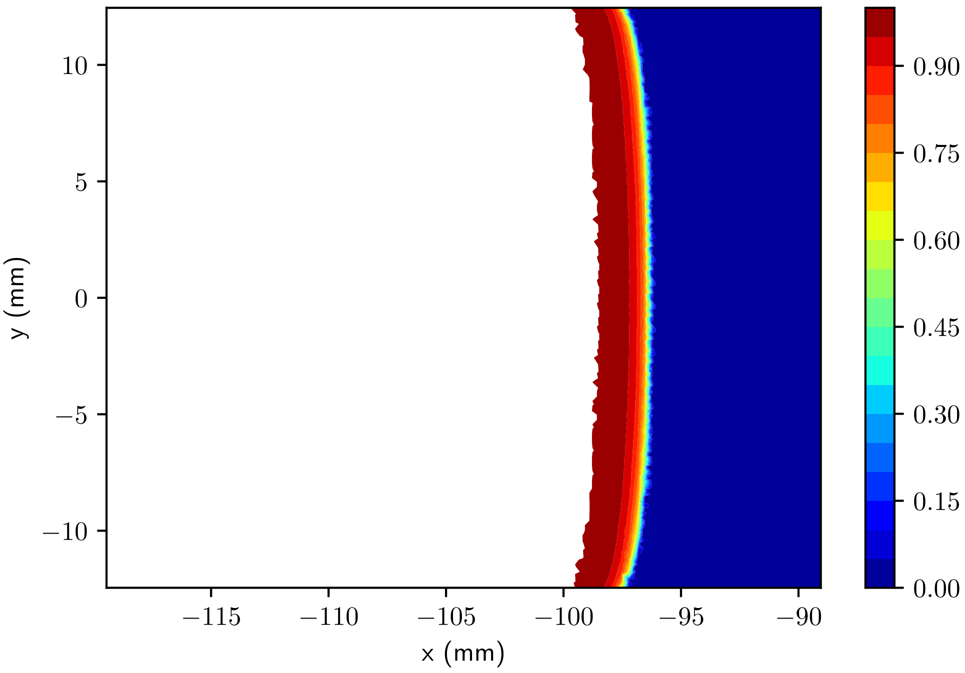

Figure 5.15: TUBA3 model: damage distribution at 4.0 mm opening. Mesh size: 1 mm, 13 integration points.

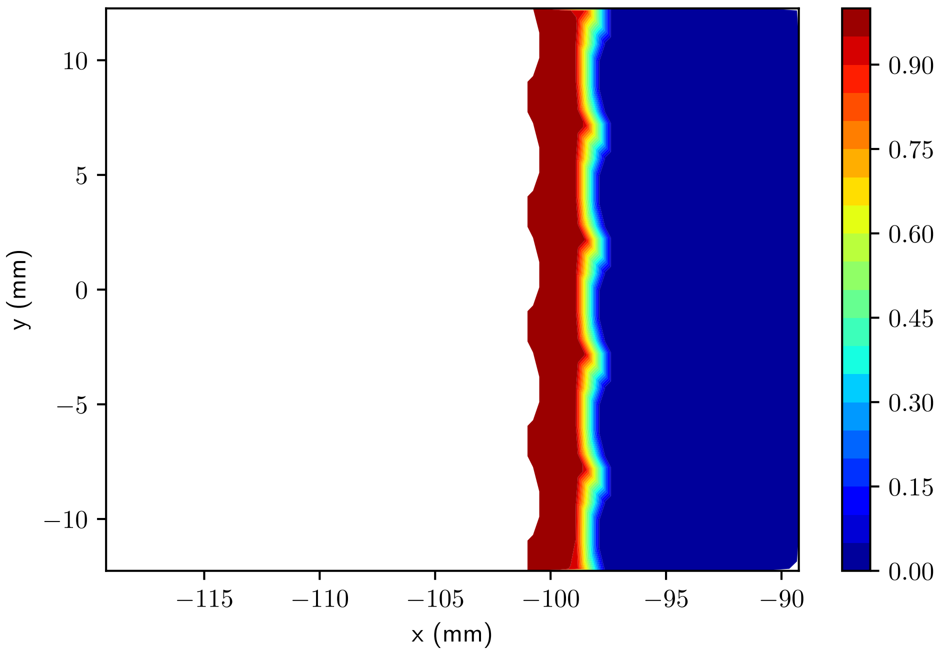

Figure 5.16: TUBA3 model: damage distribution at 4.0 mm opening. Mesh size: 5 mm, 13 integration points.

2D case. This figure should anyway be considered with a margin, since this TUBA3 model was built with a 5 mm nodal distance also along the width of the specimen, against the 1 mm separation used for Abaqus CC. No sensitivity study with respect to the number of nodes along the width was performed in this research. Anyway, even considering the TUBA3, 1 mm case, with 1 mm nodal separation also along the width, there is an 87.5 % CPU time reduction compared to Abaqus CC, remarking the potential of a C^1 FE model.

Still mainly indicative are the amounts of degrees of freedom and elements required by the different models, which anyway point out that less degrees of freedom are needed with TUBA3 discretizations. More interesting however, is that all TUBA3 simulations show an higher iterations count than the Abaqus CC one. This difference makes sense considering that viscous regularization is used only for Abaqus CC analyses. Allowing for small time increments, damage increase at an integration point can be slowed down by tuning a damage stabilization parameter. If this parameter is chosen appropriately, the material tangent stiffness matrix becomes positive definite and equilibrium is found after few iterations. However if viscous regularization is removed, Abaqus CC simulations do not converge, as demonstrated by Figure 5.17. Here the analysis stops before the specimen reaches the 4 mm opening. On the contrary, TUBA3 models do not require viscous regularization to reach convergence. Although the tangent stiffness matrix remains negative definite during degradation, the relatively high number of Gaussian integration points still ensures a gradual interface degradation.

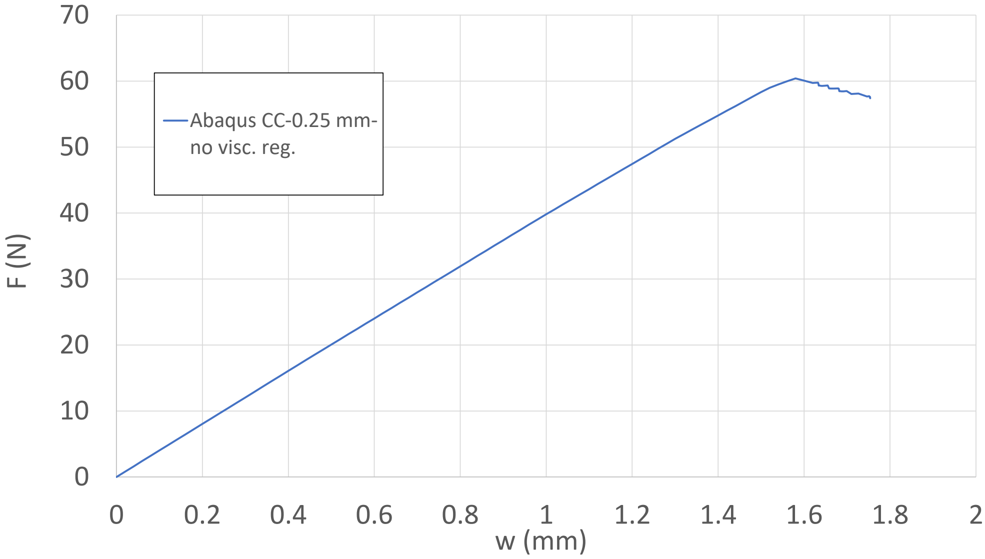

Figure 5.17: DCB load-displacement curve for the Abaqus CC, 0.25 mm mesh model with zero damage stabilization.

	Abaqus CC 0.25 mm	**TUBA3** 1 mm, 13 IPs	**TUBA3** 2 mm, 13 IPs	**TUBA3** 5 mm, 52 IPs	**TUBA3** 10 mm, 52 IPs
CPU time	12582 s	1577.9 s	1470.6 s	718.24 s	216.05 s
No. DoFs	181728	14664	4200	1656	480
No. elements	21496	6900	1872	660	144
No. iterations	2040	2249	7722	11091	5522

Table 5.3: Computational performance parameters of the DCB specimen simulations for both Abaqus CC and TUBA3 models.

Chapter 6

Conclusions and Future Work

The research work discussed had the driving objective of studying a novel approach to delamination numerical analysis, by developing C^1 thin plate and compatible cohesive elements and by testing them for the most limiting aspect of cohesive elements, namely the mesh density constraint

The approach developed confirmed the potential of modeling a delaminating composite through thin, highly regular structural elements. The key aspects and achievements of the method developed are evident when going through the set of fundamental questions asked in this research, hereby restated and answered.

1. What is a suitable triangular thin plate element which ensures a C^1 displacement field?

A very interesting candidate in this sense is the TUBA3 thin plate element or Bell triangle, described in Chapter 3. This element ensures the C^1 continuity of its shape functions, object of investigation of this work and has a triangular support, which is optimal to model complex geometrical features. Also, unlike many elements of the TUBA family, TUBA3 only has nodes at its corners, which allow to retain the banded structure of the global FE stiffness matrix. The complete formulation of the Bell triangle was outlined, going from the description of its degrees of freedom and shape functions to the step-by-step construction of the element's fundamental arrays.

2. What is the formulation of a cohesive element compatible with the plate element developed and able to capture pure-mode delamination?

A cohesive element is compatible with the substrate ones, if they share the same shape functions and have equal degrees of freedom at the common nodes. Starting from this consideration, TUBA3-CE was detailed in Chapter 3. The openings in the three modal directions were derived, while stating the adopted assumption and the peculiarities of a plate-compatible CE. In particular, oppositely to standard cohesive elements, the openings of TUBA3-CE have to include the plates' rotations and their thickness. The description of the stiffness matrix was completed with both the constitutive relation for mode I damage and the discussion of the sub-domain integration scheme developed.

3. Is the implementation of the above elements correct and what series of tests can assess this?

Both TUBA3 and TUBA3-CE required an answer to this question. For this purpose, a series of simple verification tests of known analytical solutions was considered. The plate element showed relative errors below 1% on the quantities examined and this for almost all the problems analyzed and both in its isotropic and UD composite version. The cohesive element did not undergo an actual verification until the model validation, but it was shown how it could exactly replicate the mode I cohesive law.

4. Is the final model accurate and does it improve in terms of mesh size and CPU times, when compared to the current standard in delamination modeling?

This is rightfully the pivotal research question of this work and its answer delivers the ultimate conclusions of the present research. A classic benchmark case for mode-I delamination analysis was chosen and described. The reference for this validation process was obtained by performing analyses for different mesh sizes of the delaminating region until mesh convergence was reached. Afterwards, the analyses with TUBA3 and TUBA3-CE were carried out and the raw data post-processed to obtained load-displacement curves, stress and damage profiles, cohesive zone lengths and damage maps. Impressively, the load displacement curves showed errors below 6% of the limit load, using elements 11 times larger than the numerical CZL. In terms of computational performance, models of the same mesh density achieved a 94% CPU time saving. However, despite the global behaviour of the structure was captured in a precise and efficient way, this came at the cost of less realistic predictions at the local level. In fact, due to the kinematic assumptions made by the classical plate theory, the out of plane straining of the substrates could not be reproduced. This led to inaccuracies in the stress and damage profiles and to an overprediction of the cohesive zone length.

Since the correct estimate of damage follows by accurately capturing the openings of the cohesive elements, a C^1-continuous plate model is optimally suited for predicting the structural limit load and loss of load carrying capability, using low element densities. However, in its current form, the work delivers only a proof of concept and not yet a tool usable in the FE industrial practice. The steps necessary to make the proposed C^1-continuous model a valid alternative to the current standard define the future work suggested for this project.

The indications for further development can be classified in terms of priority of the milestones to be achieved.

Pure shear mode loading Attempts at the end of the project to use TUBA3 and TUBA3-CE in a pure mode II ENF specimen showed that the onset of damage and the limit load were reached erroneously at the first increment, regardless of its magnitude. It was deduced that the model is very sensitive to mode-II openings and that small errors in their estimation could completely change the damage state of an integration point. The origin of this error likely has two origins: the impossibility for TUBA3 to deform as a membrane and the linear formulation of the kinematics of TUBA3-CE. The first limitation could be overcome by doing an extension of TUBA3 from plate to flat shell element, obtained by superimposing a plane stress element to the current TUBA3 formulation. For each node, the in-plane degrees of freedom could be added and interpolated with trilinear shape functions in area coordinates. The openings of TUBA3-CE should be then modified accordingly. Although C^1-continuity would not hold for membrane displacements, the extension suggested could already improve the mode II behaviour, as observed in the work of Russo [44], who used beam elements, which are linearly interpolated for the axial deformation.

Moreover, neglecting the geometrical non-linearities in the kinematics of TUBA3-CE could result in spurious damaging of this element. In fact, even though the small displacement range would justify to consider the deformed configuration as coincident to the initial one, the variations in Δ_{II} or Δ_{III} due to the change in configuration could make the difference between intact and damaged states. A meaningful way to account for geometrical non-linear effects would be to describe the deformation with a co-rotational scheme. This formulation could be applied to a 3D cohesive element in the following way. Each integration point of the CE mid-surface is given a triad of orthogonal vectors, two in the tangent plane and one normal to it, defining the co-rotated system. The openings in the initial configuration can be rotated by the local orientation of the co-rotated axes, in order to obtain the openings in the co-rotated reference. These can be used to write the principle of virtual work in the last converged configuration, from which the CE stiffness matrix and residual vector are found.

Mixed mode loading Once the elements will be able to deform in mode II, the constitutive relation of TUBA3-CE should be enhanced to account for the generic mode mixity of fracture. This improvement would be of simple implementation, as it only requires to change the expressions for the critical and failure openings, respectively Δ^0 and Δ^f. The formula for the damage variable and the constitutive matrix would remain unchanged and the same damage update mechanism could be kept. A useful reference at this stage would be the model of Turòn [22], summarized in Chapter 2.

Adaptive sub-domain integration As seen from the delamination results in Chapter 5, the CE integration is critical, especially when using large elements. The strategy adopted in this work was to increase the number of integration points for all the cohesive elements in the mesh, regardless of their proximity or not to the moving cohesive zone. This method stabilizes the analysis, but it is not efficient, since only the elements which are partially damaged show strongly non-linear integrands of their stiffness matrix. A smart turnaround to a global increase in the IPs number was proposed in two dimensions by Russo [44]. The method consists in an adaptive integration procedure, meaning that large numbers of integration points are used only for the elements in the cohesive zone or close to it. All the remaining CEs were integrated with much less integration points.

An adaptive integration technique technique could be adopted also with TUBA3-CEs, monitoring the damage state of the cohesive elements per iteration and increasing the number of IPs only in the partially damaged elements. However, when moving to 3D problems the options for adaptivity increase. Having big elements, it makes sense to use more IPs not on

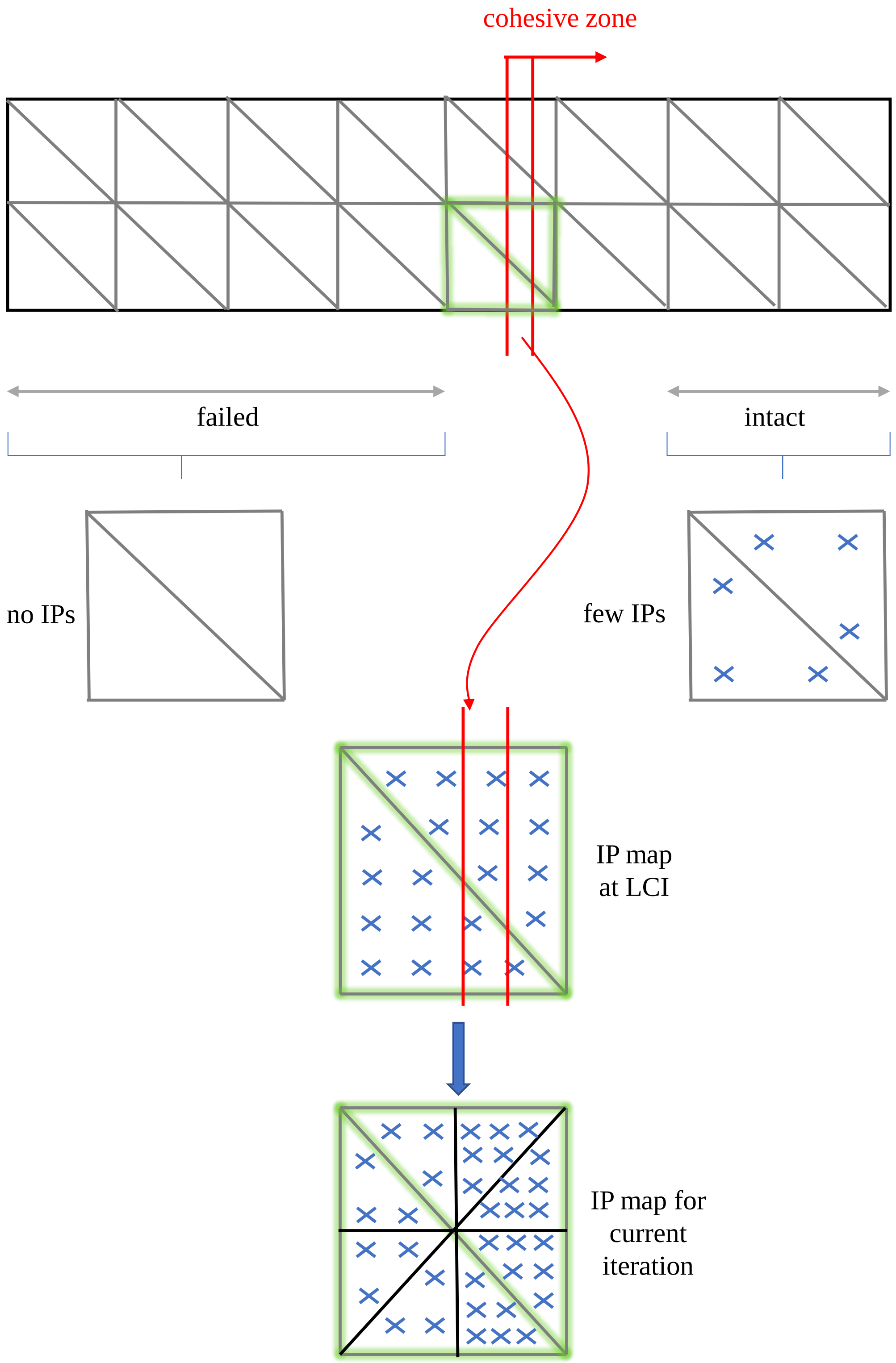

Figure 6.1: Adaptive sub-domain integration technique.

the entire element domain but only on the portions that contain the damage/stress gradients. Yang's scheme seen in Section 2.3.2 would fit the purpose, but has the inconvenience of recomputing the level set and IPs coordinates at each iteration. The subdomain integration scheme developed in this work offers an easier alternative. Suppose that the cohesive zone is moving from left to right in the plate in Figure 6.1. Initially, elements where the delamination is expected to grow should have enough IPs to detect the debonding as soon they are reached from the crack. Far field elements can instead be given few IPs. Upon cracking, the damage at the last converged increment is probed. The elements which are only partially damaged can be divided in subdomains and the IPs are increased only in those subdomains that are in or close to the cohesve zone. Once an element is totally failed, it no longer needs integration and all the IPs are removed. In this way, the amount of integration points used is optimized, without having a to find the moving subdomain and the IPs coordinates at each iteration.

Geometrically exact shell A complete framework for geometrically exact models will require to extend the TUBA3 flat shell to its curved version. The generalization of the TUBA family to 3D solid shells was carried out by Ivannikov, Tiago and Pimenta [77]. Implementing this modification in TUBA3 and TUBA3-CE could allow their use for modeling delaminations in actual engineering structures. However, some configurations will inevitably bring an increased complexity of the boundaries and careful should be used in translating them in the correct DOFs constraints. This task may be non-trivial, considering the unconventional degrees of freedom proper of TUBA elements (i.e. the nodal curvatures)

Combined matrix cracks and delaminations Composites laminates are seldom unidirectional in practical applications and their fracture often propagates through both delaminations and matrix cracks, among others. A cohesive element for plate bending, as the one presented, is not suitable for modelling in-plane types of damage. After implementing the membrane kinematics of the TUBA3 shell, matrix cracks could be reproduced by including CEs between elements of the same ply. Cohesive elements should be placed in all those mesh regions where the matrix cracks are expected to occur. However, this method could lead to very large dimensions of the FE problem. In fact, unless the crack path is known *a priori*, prediction of complex crack networks would require CEs to be inserted at all interfaces of the bulk elements.

A more meaningful way of extending TUBA3/TUBA3-CE to complex crack networks would be to enrich their set of degrees of freedom either using the Extended Finite Element Method (XFEM) [6], the Phantom Node Method (PNM) [78] or the Floating Node Method (FNM) [48]. In particular, FNM revealed to be an extremely versatile tool in representing complex structural entities and in predicting intricate damage patterns with the use of simple meshes. Also FNM has the additional advantage over XFEM and PNM of not requiring integration on parts of the domain described by the crack path.

An interesting concept, based on [79], would be the implementation of a TUBA3 floating-node laminate element. Figure 6.2 illustrates the idea for a stack of two plies. The composite panel can be represented by a 2D mesh of triangular elements, which is the element set seen by the solver during the analysis. Each triangle has associated a set of master nodes (blue circles in figure), defined during preprocessing and a set of floating nodes (triangles). Some of the floating nodes (blue triangles) are activated at the beginning of the analysis and

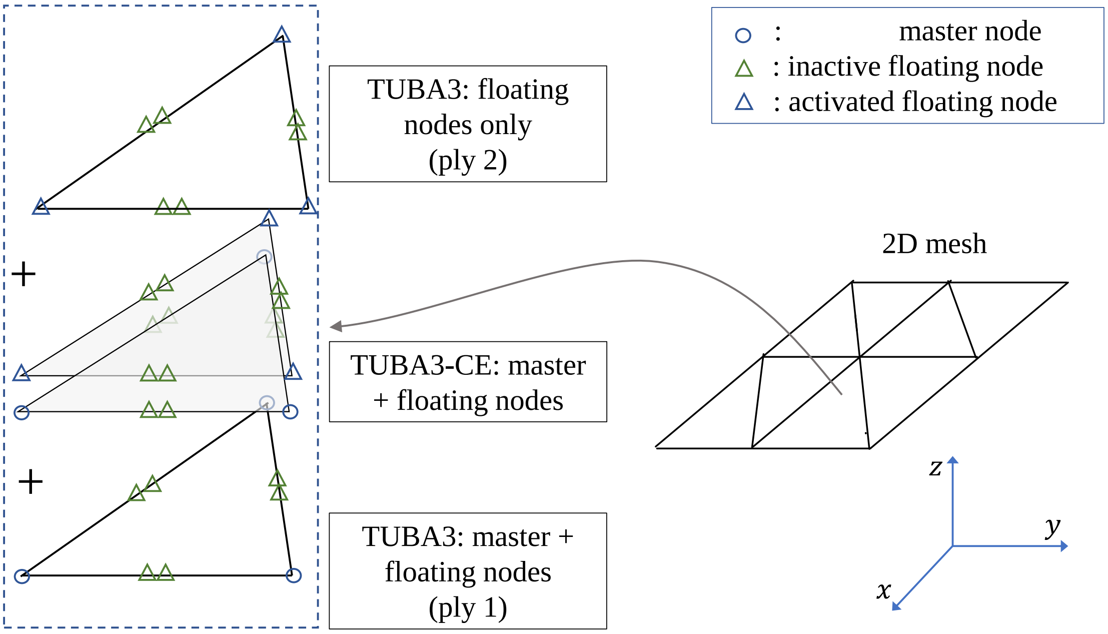

Figure 6.2: TUBA3 floating-node laminate element.

are used in triples to define additional TUBA3 plies stacked on top of the 'master TUBA3'. The remaining floating nodes (green triangles) remain inactive until a planar crack splits the element. TUBA3-CEs can then be inserted between master and floating nodes of different TUBA3 plies to open in case of delamination. When a matrix crack crosses the element, the floating nodes belonging to the edges involved are activated to form new laminate elements for each crack side. Two configurations can be conceived after planar cracking of the original element, as seen in Figure 6.3. If only TUBA3 elements are used (right case in figure), three triangular laminate elements would result, one separated by a strong discontinuity (crack) and other two still assembled together. However a 2 element configuration is also possible by using a floating node quadrilateral laminate element (left case). Also this element should be at least C^1 to maintain the advantages of high regularity in delamination. No on-the-shelf implementation is available for such an element in commercial FE software. However, the Bogner-Fox-Schmit quadrilateral [80] is a good candidate for a C^1 rectangular plate and could be brought to the TUBA3/TUBA3-CE current stage by following the same steps done in this work.

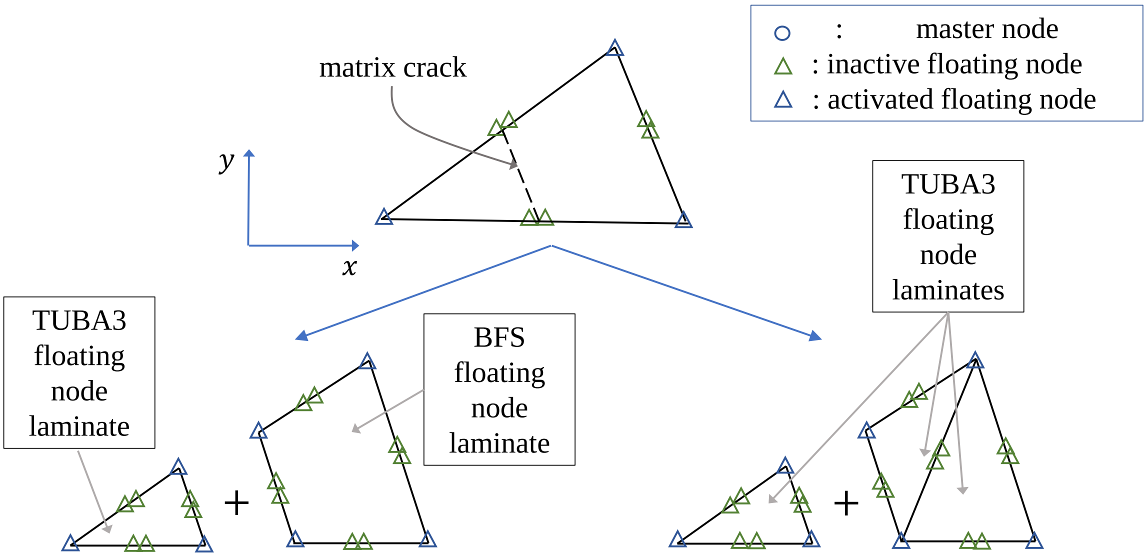

Figure 6.3: Splitting of TUBA3 floating-node laminate element upon in-plane cracking.

References

[1] Application of aerospace durability and damage tolerance approaches to wind blade design. `https://energyworkshops.sandia.gov/wp-content/uploads/2018/10/Sandia_Blade_Workshop_NSE_Composites_toSandia.pdf`.

[2] P.W. Harper and S. R. Hallett. Cohesive zone length in numerical simulations of composite delamination. *Engineering Fracture Mechanics*, 75:4774–4792, 2008.

[3] P. Camanho, C.G. Dávila, and M.F. de Moura. Mixed-Mode Decohesion Finite Elements in for the Simulation Composite of Delamination Materials. *Journal of Composite Materials*, 37(16):1415–1438, 2002.

[4] P. Camanho and C.G. Dávila. Mixed-Mode Decohesion Finite Elements in for the Simulation Composite of Delamination Materials, 2002.

[5] Q. Yang and B. Cox. Cohesive models for damage evolution in laminated composites. *International Journal of Fracture*, 133(2):107–137, 2005.

[6] N. Moës and T. Belytschko. Extended finite element method for cohesive crack growth. *Engineering Fracture Mechanics*, 69(7):813–833, 2002.

[7] A. A. Griffith. The phenomena of rupture and flow in solids. *Philosophical Transactions of the Royal Society A*, 221:163–198, 1921.

[8] G. R. Irwin. Analysis of stresses and strains near the end of a crack traversing a plate. *Journal of Applied Mechanics*, 24:361–364, 1957.

[9] E. Rybicki and M.F. Kanninen. A finite element calculation of stress intensity factors by a modified crack closure integral. *Engineering Fracture Mechanics*, 9:931–938, 12 1977.

[10] D. Carolan, A. Ivankovic, A. Kinloch, S. Sprenger, and A. Taylor. Toughened carbon fibre reinforced polymer composites with nanoparticle modified epoxy matrices. *Journal of Materials Science*, 52:1767–1788, 01 2017.

[11] D. S. Dugdale. Yielding of steel sheets containing slits. *Journal of the Mechanics and Physics of Solids*, 8(2):100–104, 1960.

[12] G. I. Barenblatt. The Mathematical Theory of Equilibrium of Crack in Brittle Fracture. *Adv. Appl. Mech.*, 7:55–129, 1962.

[13] Michael Smith. *ABAQUS/Standard User's Manual, Version 6.9.* Simulia, 2009.

[14] X.P. Xu and A. Needleman. Void nucleation by inclusion debonding in a crystal matrix. *Modelling and Simulation in Materials Science and Engineering*, 1:111–132, 1993.

[15] G. T. Camacho and M. Ortiz. Computational modelling of impact damage in brittle materials. *International Journal of Solids and Structures*, 33(20-22):2899–2938, 1996.

[16] V. Tvergaard and J. W. Hutchinson. The relation between crack growth resistance and fracture process parameters in elastic-plastic solids. *Journal of the Mechanics and Physics of Solids*, 40(6):1377–1397, 1992.

[17] N. Chandra, H. Li, C. Shet, and H. Ghonem. Some issues in the application of cohesive zone models for metal-ceramic interfaces. *International Journal of Solids and Structures*, 39(10):2827–2855, 2002.

[18] C. Shet and N. Chandra. Effect of the shape of T-δ cohesive zone curves on the fracture response. *Mechanics of Advanced Materials and Structures*, 11(3):249–275, 2004.

[19] A. Turòn, C. G. Dávila, P. P. Camanho, and J. Costa. An engineering solution for mesh size effects in the simulation of delamination using cohesive zone models. *Engineering Fracture Mechanics*, 74(10):1665–1682, 2007.

[20] A. Turòn, P.P. Camanho, J. Costa, and J. Renart. Accurate simulation of delamination growth under mixed-mode loading using cohesive elements: Definition of interlaminar strengths and elastic stiffness. *Composite Structures*, 92(8):1857 – 1864, 2010.

[21] A. Turòn, E. González, C. Sarrado, G. Guillamet, and P. Maimí. Accurate simulation of delamination under mixed-mode loading using a cohesive model with a mode-dependent penalty stiffness. *Composite Structures*, 184, 10 2017.

[22] A. Turòn, P. P. Camanho, J. Costa, and C. G. Dávila. A damage model for the simulation of delamination in advanced composites under variable-mode loading. *Mechanics of Materials*, 38(11):1072–1089, 2006.

[23] M .L. Benzeggagh and M. Kenane. Measurement of mixed mode delamination fracture toughness of unidirectional glass/epoxy composites with mixed mode bending apparatus. *Composite Science and Technology*, 56:439–449, 1996.

[24] J.C.J. Schellekens and R. De Borst. On the numerical modelling of edge delamination in composites. volume 120 of *Key Engineering Materials*, pages 131–160, 5 1996.

[25] C. G. Dàvila, P. P. Camanho, and A. Turòn. Effective simulation of delamination in aeronautical structures using shells and cohesive elements. *Journal of Aircraft*, 45(2):663–672, 2008.

[26] Q. D. Yang, X.J. Fang, J.X. Shi, and J. Lua. An improved cohesive element for shell delamination analyses. *International Journal for Numerical Methods in Engineering*, 83(March 2010):611–641, 2010.

[27] R. Russo and B. Chen. Overcoming the cohesive zone limit in composites delamination: modelling with C^1 continuous cohesive elements and higher-order adaptive integration. (private communication, manuscript in preparation).

[28] A. Soto, E. V. González, P. Maimí, A. Turòn, J. R. Sainz de Aja, and F. M. de la Escalera. Cohesive zone length of orthotropic materials undergoing delamination. *Engineering Fracture Mechanics*, 159:174–188, 2016.

[29] C. Y. Hui, A. Jagota, S. J. Bennison, and J. D. Londono. Crack blunting and the strength of soft elastic solids. *Proceedings of the Royal Society A: Mathematical, Physical and Engineering Sciences*, 459(2034):1489–1516, 2003.

[30] J. R. Rice. The mechanics of earthquake rupture. *Physics of the Earth's Interior*, pages 555–649, 1980.

[31] M.L. Falk, A. Needleman, and J.R. Rice. A critical evaluation of dynamic fracture simulations using cohesive surfaces. *Journal de Physique IV*, 5:43–50, 2001.

[32] A. Hillerborg, M. Modéer, and P. E. Petersson. Analysis of crack formation and crack growth in concrete by means of fracture mechanics and finite elements. *Cement and Concrete Research*, 6(6):773–781, 1976.

[33] E. Smith. The failure of a strain-softening material: I. Analytical approach for a double cantilever beam specimen. *Theoretical and Applied Fracture Mechanics*, 11(1):59–64, 1989.

[34] R. Massabò and B.N. Cox. Concepts for bridged Mode II delamination cracks. *Journal of the Mechanics and Physics of Solids*, 47(6):1265–1300, 1999.

[35] A. Turòn, J. Costa, P. P. Camanho, and P. Maimí. Analytical and numerical investigation of the length of the cohesive zone in delaminated composite materials. In *Mechanical response of composite. Computational Methods in Applied Sciences, vol 10.*, pages 77–97. Springer, Dordrecht, 2007.

[36] I. Guiamatsia, J.K. Ankersen, G.A.O. Davies, and L. Iannucci. Decohesion finite element with enriched basis functions for delamination. *Composites Science and Technology*, 69(15):2616 – 2624, 2009.

[37] I. Guiamatsia, G.A.O. Davies, J.K. Ankersen, and L. Iannucci. A framework for cohesive element enrichment. *Composite Structures*, 92(2):454 – 459, 2010.

[38] J.M. Melenk and I. Babuška. The partition of unity finite element method: Basic theory and applications. *Computer Methods in Applied Mechanics and Engineering*, 139(1):289 – 314, 1996.

[39] M. Samimi, Van Dommelen J.A.W., and M.G.D. Geers. An enriched cohesive zone model for delamination in brittle interfaces. *International Journal for Numerical Methods in Engineering*, 80(5):609–630, 2009.

[40] M. Samimi, J.A.W. Van Dommelen, and M.G.D. Geers. A self-adaptive finite element approach for simulation of mixed-mode delamination using cohesive zone models. *Engineering Fracture Mechanics*, 78(10):2202–2219, 2011.

[41] M. Samimi, J.A.W. Van Dommelen, and M.G.D. Geers. A three-dimensional self-adaptive cohesive zone model for interfacial delamination. *Computer Methods in Applied Mechanics and Engineering*, 200(49-52):3540–3553, 2011.

[42] B.C. Do, W. Liu, Q.D. Yang, and X.Y. Su. Improved cohesive stress integration schemes for cohesive zone elements. *Engineering Fracture Mechanics*, 107:14–28, 2013.

[43] D. Álvarez, B.R.K. Blackman, F. J. Guild, and A. J. Kinloch. Mode I fracture in adhesively-bonded joints: A mesh-size independent modelling approach using cohesive elements. *Engineering Fracture Mechanics*, 115:73–95, 2014.

[44] R. Russo. High order adaptively integrated cohesive elements. Master's thesis, Delft University of Technology, 2018.

[45] M. Latifi, F. P. van der Meer, and L. J. Sluys. An interface thick level set model for simulating delamination in composites. *International Journal for Numerical Methods in Engineering*, 111(4):303–324, 2017.

[46] F.P. van der Meer, N. Moës, and L.J. Sluys. A level set model for delamination - Modeling crack growth without cohesive zone or stress singularity. *Engineering Fracture Mechanics*, 79:191 – 212, 2012.

[47] X. Lu, B.Y. Chen, V.B.C. Tan, and T.E. Tay. Adaptive floating node method for modelling cohesive fracture of composite materials. *Engineering Fracture Mechanics*, 194:240 – 261, 2018.

[48] B.Y. Chen, S.T. Pinho, N.V. De Carvalho, P.M. Baiz, and T.E. Tay. A floating node method for the modelling of discontinuities in composites. *Engineering Fracture Mechanics*, 127:104 – 134, 2014.

[49] T.J.R. Hughes, J. A. Cottrell, and Y. Bazilevs. Isogeometric analysis: CAD, finite elements, NURBS, exact geometry and mesh refinement. *Computer Methods in Applied Mechanics and Engineering*, 194(39-41):4135–4195, 2005.

[50] J.A. Cottrell, T.J.R. Hughes, and Y. Bazilevs. *Isogeometric Analysis*. John Wiley & Sons Ltd, 2009.

[51] M.J. Borden, M.A. Scott, J.A. Evans, and T. J.R. Hughes. Isogeometric finite element data structures based on Bézier extraction of NURBS. *International Journal for Numerical Methods in Engineering*, 87(August 2010):15–47, 2011.

[52] M.A. Scott, M.J. Borden, C.V. Verhoosel, T.W. Sederberg, and T. J.R. Hughes. Isogeometric finite element data structures based on Bézier extraction of T-splines. *International Journal for Numerical Methods in Engineering*, 88(March 2011):126–156, 2011.

[53] F. Irzal, J. J. C. Remmers, C.V. Verhoosel, and R. de Borst. An isogeometric analysis Bézier interface element for mechanical and poromechanical fracture problems. *International Journal for Numerical Methods in Engineering*, 97(December 2013):608–628, 2014.

[54] V.P. Nguyen, P. Kerfriden, and S.P.A. Bordas. Two- and three-dimensional isogeometric cohesive elements for composite delamination analysis. *Composites Part B: Engineering*, 60:193–212, 2014.

[55] S. Hosseini, J. J.C. Remmers, C.V. Verhoosel, and R. de Borst. Propagation of delamination in composite materials with isogeometric continuum shell elements. *International Journal for Numerical Methods in Engineering*, 102(3-4):159–179, 2015.

[56] R. Russo and B.Y. Chen. Higher Order Adaptively Integrated Cohesive Element. In *18th European Conference on Composite Materials*, number June, pages 24–28, 2018.

[57] K. Bell. A refined triangular plate bending finite element. *International Journal for Numerical Methods in Engineering*, 1(1):101–122, 1969.

[58] O. C. Zienkiewicz, R. Taylor, and J.Z. Zhu. *The Finite Element Method: Its Basis and Fundamentals*. Butterworth-Heinemann, 2013.

[59] MSC Nastran product information & documentation. `https://simcompanion.mscsoftware.com/infocenter/index?page=content&id=DOC9282`.

[60] Ansys mechanical APDL documentation. `https://www.sharcnet.ca/Software/Ansys/16.2.3/en-us/help/ai_sinfo/ans_intro.html`.

[61] J.L. Batoz, K.J. Bathe, and L.W. Ho. A study of three-node triangular plate bending elements. *International Journal for Numerical Methods in Engineering*, 15(12):1771–1812, 12 1980.

[62] LS-Dyna manuals. `https://www.dynasupport.com/manuals`.

[63] Introduction to isogeometric elements in LS-Dyna. `https://www.dynamore.de/de/download/papers/forum11/entwicklerforum-2011/hartmann.pdf`.

[64] J.H. Argyris, I. Fried, and D.W. Scharpf. The TUBA family of plate elements for the matrix displacement method. *The Aeronautical Journal*, 72(692):701–709, 1968.

[65] S. Dasgupta and D. Sengupta. A higher-order triangular plate bending element revisited. *International Journal for Numerical Methods in Engineering*, 30(3):419–430, 1990.

[66] M.A. Eisenberg and L.E. Malvern. On finite element integration in natural co-ordinates. *International Journal for Numerical Methods in Engineering*, 7(4):574–575, 1973.

[67] Quadrature formulas in two dimensions, online lecture notes. `http://math2.uncc.edu/~{}shaodeng/TEACHING/math5172/Lectures/Lect_15.pdf`, 2010.

[68] G.R. Cowper. Gaussian quadrature formulas for triangles. *International Journal for Numerical Methods in Engineering*, 7(3):405–408, 1973.

[69] P.C. Hammer, O.J. Marlowe, and A.H. Stroud. Numerical integration over simplexes and cones. *Mathematical Tables and Other Aids to Computation*, 10(55):130–137, 1956.

[70] B.M. Irons. Engineering applications of numerical integration in stiffness methods. *AIAA journal*, 4(11):2035–2037, 1966.

[71] C.A. Felippa. *Refined finite element analysis of linear and nonlinear two-dimensional structures.* PhD thesis, 1968.

[72] D.A. Dunavant. High degree efficient symmetrical gaussian quadrature rules for the triangle. *International Journal for Numerical Methods in Engineering*, 21(6):1129–1148, 1985.

[73] S. Timoshenko and S. Woinowsky-Krieger. *Theory of plates and shells.* Engineering societies monographs. McGraw-Hill, 1959.

[74] R. Krueger. A summary of benchmark examples to assess the performance of quasi-static delamination propagation prediction capabilities in finite element codes. *Journal of Composite Materials*, 49(26):3297–3316, 2015.

[75] J. Zhang and X. Zhang. Simulating low-velocity impact induced delamination in composites by a quasi-static load model with surface-based cohesive contact. *Composite Structures*, 125:51–57, 2015.

[76] W.C. Cui, M.R. Wisnom, and M. Jones. A comparison of failure criteria to predict delamination of unidirectional glass/epoxy specimens waisted through the thickness. *Composites*, 23(3):158 – 166, 1992.

[77] V. Ivannikov, C. Tiago, and P. Pimenta. Generalization of the C1 TUBA plate finite elements to the geometrically exact Kirchhoff–Love shell model. *Computer Methods in Applied Mechanics and Engineering*, 294:210–244, 09 2015.

[78] A. Hansbo and P. Hansbo. A finite element method for the simulation of strong and weak discontinuities in solid mechanics. *Computer Methods in Applied Mechanics and Engineering*, 193(33):3523 – 3540, 2004.

[79] B.Y. Chen, T.E. Tay, S.T. Pinho, and V.B.C. Tan. Modelling delamination migration in angle-ply laminates. *Composites Science and Technology*, 142:145 – 155, 2017.

[80] F.K. Bogner, R.L. Fox, and L.A. Schmit. The generation of interelement compatible stiffness and mass matrices by the use of interpolation formulas. In *Proceedings of the Conference on Matrix Methods in Structural Mechanics*, number October, pages 863–886, 1965.

[81] J.G. Williams. The fracture mechanics of delamination tests. *The Journal of Strain Analysis for Engineering Design*, 24(4):207–214, 1989.

[82] J.R. Reeder, K. Demarco, and K.S. Whitley. The use of doubler reinforcement in delamination toughness testing. *Composites Part A: Applied Science and Manufacturing*, 35(11):1337 – 1344, 2004.

Appendix A

TUBA3 shape functions

A planar triangle is considered, of vertices (x_1, y_1), (x_2, y_2) and (x_3, y_3). The following quantities can be defined

$$\begin{cases} a_i = & x_j y_k - x_k y_j \\ b_i = & y_j - y_k \\ c_i = & x_k - x_j \end{cases} \tag{A.1}$$

$$r_{ij} = -\frac{b_i b_j + c_i c_j}{b_i^2 + c_i^2} \tag{A.2}$$

where i,j,k are cyclic permutations of 1,2,3.

Using the definitions in Equations (A.1) and (A.2), the first six shape functions of the TUBA3 triangle, as reported in [65], are

$$\begin{aligned}
N_1(L_1, L_2, L_3) =& L_1^5 + 5L_1^4 L_2 + 5L_1^4 L_3 + 10L_1^3 L_2^2 + 10L_1^3 L_3^2 + 20L_1^3 L_2 L_3 \\
& + 30r_{21} L_1^2 L_2 L_3^2 + 30r_{31} L_1^2 L_2^2 L_3 \\
N_2(L_1, L_2, L_3) =& c_3 L_1^4 L_2 - c_2 L_1^4 L_3 + 4c_3 L_1^3 L_2^2 - 4c_2 L_1^3 L_3^2 + 4(c_3 - c_2) L_1^3 L_2 L_3 \\
& - (3c_1 + 15r_2 1c_2) L_1^2 L_2 L_3^2 + (3c_1 + 15r_{31} c_3) L_1^2 L_2^2 L_3 \\
N_3(L_1, L_2, L_3) =& - b_3 L_1^4 L_2 + b_2 L_1^4 L_3 - 4b_3 L_1^3 L_2^2 + 4b_2 L_1^3 L_3^2 + 4(b_2 - b_3) L_1^3 L_2 L_3 \\
& + (3b_1 + 15r_{21} b_2) L_1^2 L_2 L_3^2 - (3b_1 + 15r_{31} b_3) L_1^2 L_2^2 L_3 \\
N_4(L_1, L_2, L_3) =& \frac{c_3^2}{2} L_1^3 L_2^2 + \frac{c_2^2}{2} L_1^3 L_3^2 - c_2 c_3 L_1^3 L_2 L_3 + \left(c_1 c_2 + \frac{5}{2} r_{21} c_2^2 \right) L_1^2 L_2 L_3^2 \\
& + \left(c_1 c_3 + \frac{5}{2} r_{31} c_3^2 \right) L_1^2 L_2^2 L_3 \\
N_5(L_1, L_2, L_3) =& - b_3 c_3 L_1^3 L_2^2 - b_2 c_2 L_1^3 L_3^2 + (b_2 c_3 + b_3 c_2) L_1^3 L_2 L_3 \\
& - (b_1 c_2 + b_2 c_1 + 5r_{21} b_2 c_2) L_1^2 L_2 L_3^2 - (b_1 c_3 + b_3 c_1 + 5r_{31} b_3 c_3) L_1^2 L_2^2 L_3
\end{aligned}$$

$$
\begin{aligned}
N_6(L_1, L_2, L_3) = & \frac{b_3^2}{2} L_1^3 L_2^2 + \frac{b_2^2}{2} L_1^3 L_3^2 - b_2 b_3 L_1^3 L_2 L_3 + \left(b_1 b_2 + \frac{5}{2} r_{21} b_2^2 \right) L_1^2 L_2 L_3^2 \\
& + \left(b_1 b_3 + \frac{5}{2} r_{31} b_3^2 \right) L_1^2 L_2^2 L_3
\end{aligned}
$$

where L_1,L_2 and L_3 are the triangle's area coordinates.

The remaining shape functions (N_7 to N_{18}) are defined in sets of six, by cyclically permuting the indices 1,2 and 3.

Appendix B

FORTRAN95 code for $[Q]$

The source code to follow is the FORTRAN95 adaptation of the FORTRAN77 code in the paper by Dasgupta and Sengupta [65].

```fortran
include 'globals/parameter_module.f90'
! Module for double precision numbers, logical parameters and strings for
! error messages
!--------------------------------------------------------------------------------

module Qform_env

use parameter_module, only: DP, ZERO, HALF, STAT_SUCCESS, STAT_FAILURE, MSGLENGTH
! DP:           parameter used to define double precision kind numbers
! ZERO,HALF:         double precision numbers
! STAT_SUCCESS, STAT_FAILURE: integer for successful/failed status value
! MSGLENGTH:         integer for length of error message string

implicit none

!  List of element-dependent parameters
integer, parameter,public   :: NDIM=3
integer, parameter,public   :: NNODE=3
integer, parameter,public   :: NDOF=18



contains



subroutine Qform(coord_nod,area,QXX,QYY,QXY,istat,emsg)
! Purpose:
! Forms the matrices Qxx, Qyy, Qxy for TUBA3 element, as from appendix
! of the article 'A higher order triangular plate bending element
! revisited' by S. Dasgupta and D. Sengupta
```

```
!
! Record of revision:
!     Date       Programmer              Description of change
!    ========   ====================    ========================================
!  28/11/18  G. Tosti Balducci      Conversion original .f->.f90


!    Declaration
! I/O
 real(DP), intent(in) :: coord_nod(NDIM,NNODE)
 real(DP), intent(out) ::  area
 real(DP), intent(out) ::  QXX(30,NDOF), QYY(30,NDOF), QXY(30,NDOF)
 integer,  intent(out)    :: istat
 character(len=MSGLENGTH), intent(out)    :: emsg
! LOCAL variables
 integer, parameter  :: NDEST(NDOF)=(/4,5,6,8,7,9,7,6,9,4,8,5,8,9,&
           &5,7,4,6/)
 real(DP)     ::  XT(NNODE), YT(NNODE)
 real(DP)     :: B(NNODE), C(NNODE)
 real(DP)     ::  TWOD, AR
 real(DP)     ::  P(NNODE)
 real(DP)     ::  R(NNODE,NNODE)
! counters
 integer      :: I,J,M,IND,JC,JJ,MM,K,IPER,NR

! Initialization
 area=ZERO
 QXX=ZERO
 QYY=ZERO
 QXY=ZERO
 istat=STAT_SUCCESS
 emsg=''
 XT=coord_nod(1,:)
 YT=coord_nod(2,:)
 B=ZERO
 C=ZERO
 TWOD=ZERO
 AR=ZERO
 P=ZERO
 R=ZERO

! Preliminaries
 B(1)=YT(2)-YT(3)
 B(2)=YT(3)-YT(1)
 B(3)=YT(1)-YT(2)
 C(1)=XT(3)-XT(2)
 C(2)=XT(1)-XT(3)
 C(3)=XT(2)-XT(1)
 TWOD=B(1)*C(2)-B(2)*C(1)
 AR=HALF*TWOD
 P(1)=B(2)*C(3)+B(3)*C(2)
 P(2)=B(3)*C(1)+B(1)*C(3)
 P(3)=B(1)*C(2)+B(2)*C(1)
 do I=1,NNODE
  do J=1,NNODE
   R(I,J)=-(B(I)*B(J)+C(I)*C(J))/(B(I)*B(I)+C(I)*C(I))
  end do
```

```
 end do
 IND=0

! Main calculations
 main_loop: do I=1,NNODE
  JC=(I-1)*6
  QXX(I,JC+4)=TWOD**2
     QYY(I,JC+6)=TWOD**2
     QXY(I,JC+5)=2._DP*TWOD**2
  J=I+1
     IF(J>3) J=J-3
  M=J+1
     IF(M>3) M=M-3
     JJ=J
     MM=M
  QXX(10,JC+1)=120._DP*(B(I)*B(I)+2._DP*B(I)*(R(J,I)*B(M)+R(M,I)*B(J)))
     QXX(10,JC+2)=-48._DP*B(I)*TWOD-120._DP*B(I)*(R(J,I)*B(M)*C(J)-R(M,I)*&
        &B(J)*C(M))
  QXX(10,JC+3)=120._DP*B(I)*B(J)*B(M)*(R(J,I)-R(M,I))
     QXX(10,JC+4)=-6._DP*B(I)*B(I)*C(J)*C(M)+8._DP*B(I)*C(I)*P(I)+20._DP*&
  &B(I)*(R(J,I)*B(M)*C(J)*C(J)+R(M,I)*B(J)*C(M)*C(M))
  QXX(10,JC+5)=-2._DP*B(I)*B(I)*P(I)-B(I)*B(J)*B(M)*(16._DP*C(I)+&
  &40._DP*(R(J,I)*C(J)+R(M,I)*C(M)))
  QXX(10,JC+6)=10._DP*B(I)*B(I)*B(J)*B(M)+20._DP*B(I)*B(M)*B(J)*&
  &(R(J,I)*B(J)+R(M,I)*B(M))
!
!
  QYY(10,JC+1)=120._DP*(C(I)*C(I)+2._DP*C(I)*(R(J,I)*C(M)+R(M,I)*C(J)))
  QYY(10,JC+2)=120._DP*C(I)*C(J)*C(M)*(R(M,I)-R(J,I))
  QYY(10,JC+3)=-48._DP*C(I)*TWOD+120._DP*C(I)*(R(J,I)*C(M)*B(J)-&
  &R(M,I)*C(J)*B(M))
  QYY(10,JC+4)=10._DP*C(I)*C(I)*C(J)*C(M)+20._DP*C(I)*C(J)*C(M)*&
  &(R(J,I)*C(J)+R(M,I)*C(M))
  QYY(10,JC+5)=-2._DP*C(I)*C(I)*P(I)-C(I)*C(J)*C(M)*(16._DP*B(I)+40._DP*&
  &(R(J,I)*B(J)+R(M,I)*B(M)))
  QYY(10,JC+6)=-6._DP*C(I)*C(I)*B(J)*B(M)+8._DP*C(I)*B(I)*P(I)+&
  &20._DP*C(I)*(R(J,I)*C(M)*B(J)**2+R(M,I)*C(J)*B(M)**2)
!
!
  QXY(10,JC+1)=240._DP*(B(I)*C(I)+R(J,I)*P(J)+R(M,I)*P(M))
  QXY(10,JC+2)=-48._DP*C(I)*TWOD-120._DP*(R(J,I)*C(J)*P(J)-R(M,I)*&
  &C(M)*P(M))
  QXY(10,JC+3)=-48._DP*B(I)*TWOD+120._DP*(R(J,I)*B(J)*P(J)-&
  &R(M,I)*B(M)*P(M))
  QXY(10,JC+4)=4._DP*B(I)*C(I)*C(J)*C(M)+8._DP*C(I)*C(I)*P(I)+&
  &20._DP*(R(J,I)*C(J)*C(J)*P(J)+R(M,I)*C(M)*C(M)*P(M))
  QXY(10,JC+5)=12._DP*B(I)*C(I)*P(I)-16._DP*P(J)*P(M)-40._DP*(R(J,I)*&
  &B(J)*C(J)*P(J)+R(M,I)*B(M)*C(M)*P(M))
  QXY(10,JC+6)=4._DP*C(I)*B(I)*B(J)*B(M)+8._DP*B(I)*B(I)*P(I)+20._DP*&
  &(R(J,I)*B(J)*B(J)*P(J)+R(M,I)*B(M)*B(M)*P(M))

!
!
  row_selec_loop: do K=1,3
   iper_loop : do IPER=1,2
    select case (IPER)
    case(1)
```

```fortran
     J=JJ
     M=MM
    case(2)
     J=MM
     M=JJ
    case default
     istat=STAT_FAILURE
     emsg='IPER is diff. from 1 or 2, Qform, &
     & element_module'
     QXX=ZERO; QYY=ZERO; QXY=ZERO
     return
    end select
    IND=IND+1
    NR=NDEST(IND)
    select case (K)
    case(1)
     QXX(NR,JC+1)=60._DP*(-B(I)*B(I)+R(J,I)*B(M)*B(M)+2._DP*R(M,I)*B(J)*&
     &B(M))
     QXX(NR,JC+2)=12._DP*B(I)*TWOD+(-1._DP)**IPER*(24._DP*B(I)*B(I)*C(M)+18._DP*&
     &B(M)*B(M)*C(I)+30._DP*R(J,I)*B(M)*B(M)*C(J)-60._DP*R(M,I)*B(J)*B(M)*&
     &C(M))
     QXX(NR,JC+3)=-(-1._DP)**IPER*(24._DP*B(I)*B(I)*B(M)+18._DP*B(M)*B(M)*B(I)&
     &+30._DP*R(J,I)*B(M)*B(M)*B(J)-60._DP*R(M,I)*B(M)*B(M)*B(J))
     QXX(NR,JC+4)=-(-1._DP)**IPER*6._DP*B(I)*C(M)*TWOD+2._DP*B(M)*B(M)*C(I)*&
     &C(J)+4._DP*B(J)*B(M)*C(M)*C(I)+5._DP*R(J,I)*B(M)*B(M)*C(J)*C(J)+&
     &10._DP*R(M,I)*B(J)*B(M)*C(M)*C(M)
     QXX(NR,JC+5)=(-1._DP)**IPER*10._DP*B(I)*B(M)*TWOD-6._DP*B(M)*B(M)*P(M)-&
     &10._DP*R(J,I)*B(M)*B(M)*B(J)*C(J)-20._DP*R(M,I)*B(M)*B(M)*B(J)*C(M)
     QXX(NR,JC+6)=6._DP*B(I)*B(J)*B(M)*B(M)+5._DP*R(J,I)*B(J)*B(J)*B(M)*&
     &B(M)+10._DP*R(M,I)*B(J)*B(M)*B(M)*B(M)
!
!
     QYY(NR,JC+1)=60._DP*(-C(I)*C(I)+R(J,I)*C(M)*C(M)+2._DP*R(M,I)*C(J)*&
     &C(M))
     QYY(NR,JC+2)=(-1._DP)**IPER*(24._DP*C(I)*C(I)*C(M)+18._DP*C(M)*C(M)*C(I)&
     &+30._DP*R(J,I)*C(M)*C(M)*C(J)-60._DP*R(M,I)*C(M)*C(M)*C(J))
     QYY(NR,JC+3)=12._DP*C(I)*TWOD-(-1._DP)**IPER*(24._DP*C(I)*C(I)*B(M)+&
     &18._DP*C(M)*C(M)*B(I)+30._DP*R(J,I)*C(M)*C(M)*B(J)-60._DP*R(M,I)*C(J)*&
     &C(M)*B(M))
     QYY(NR,JC+4)=6._DP*C(I)*C(J)*C(M)*C(M)+5._DP*R(J,I)*C(J)*C(J)*C(M)*&
     &C(M)+10._DP*R(M,I)*C(J)*C(M)**3
     QYY(NR,JC+5)=-(-1._DP)**IPER*10._DP*C(I)*C(M)*TWOD-6._DP*C(M)*C(M)*&
     &P(M)-10._DP*R(J,I)*C(M)*C(M)*C(J)*B(J)-20._DP*R(M,I)*C(M)*C(M)*&
     &C(J)*B(M)
     QYY(NR,JC+6)=(-1._DP)**IPER*6._DP*C(I)*B(M)*TWOD+2._DP*C(M)*C(M)*B(I)*&
     &B(J)+4._DP*C(J)*C(M)*B(M)*B(I)+5._DP*R(J,I)*C(M)*C(M)*B(J)*B(J)+&
     &10._DP*R(M,I)*C(J)*C(M)*B(M)*B(M)
!
!
     QXY(NR,JC+1)=120._DP*(-B(I)*C(I)+R(J,I)*B(M)*C(M)+R(M,I)*P(I))
     QXY(NR,JC+2)=12._DP*C(I)*TWOD+(-1._DP)**IPER*(48._DP*B(I)*C(I)*C(M)+&
     &36._DP*B(M)*C(M)*C(I)+60._DP*R(J,I)*B(M)*C(M)*C(J)-60._DP*R(M,I)*&
     &C(M)*P(I))
     QXY(NR,JC+3)=12._DP*B(I)*TWOD-(-1._DP)**IPER*(48._DP*C(I)*B(I)*B(M)+&
     &36._DP*C(M)*B(M)*B(I)+60._DP*R(J,I)*C(M)*B(M)*B(J)-60._DP*R(M,I)*&
     &B(M)*P(I))
     QXY(NR,JC+4)=10._DP*C(I)*B(J)*C(M)*C(M)+2._DP*C(I)*C(J)*B(M)*C(M)+&
```

```
       &10._DP*R(J,I)*C(J)*C(J)*B(M)*C(M)+10._DP*R(M,I)*C(M)*C(M)*P(I)
       QXY(NR,JC+5)=-16._DP*B(M)*C(M)*P(M)+2._DP*P(I)*P(J)-20._DP*R(J,I)*B(J)*&
       &C(J)*B(M)*C(M)-20._DP*R(M,I)*B(M)*C(M)*P(I)
       QXY(NR,JC+6)=10._DP*B(I)*C(J)*B(M)*B(M)+2._DP*B(I)*B(J)*C(M)*B(M)+&
       &10._DP*R(J,I)*B(J)*B(J)*C(M)*B(M)+10._DP*R(M,I)*B(M)*B(M)*P(I)
!
!
      case(2)
       QXX(NR,JC+1)=60._DP*(B(I)*B(I)+2._DP*R(M,I)*B(M)*B(I))
       QXX(NR,JC+2)=12._DP*B(I)*TWOD-(-1._DP)**IPER*(36._DP*B(I)*B(I)*C(M)+&
       &60._DP*R(M,I)*B(M)*B(I)*C(M))
       QXX(NR,JC+3)=(-1._DP)**IPER*(36._DP*B(I)*B(I)*B(M)+60._DP*R(M,I)*&
       &B(M)*B(M)*B(I))
       QXX(NR,JC+4)=3._DP*B(I)*B(I)*C(M)*C(M)+4._DP*B(I)*B(M)*C(I)*C(M)+&
       &10._DP*R(M,I)*B(I)*B(M)*C(M)*C(M)
       QXX(NR,JC+5)=-10._DP*B(I)*B(I)*C(M)*B(M)-4._DP*B(M)*B(M)*C(I)*B(I)&
       &-20._DP*R(M,I)*B(M)*B(M)*B(I)*C(M)
       QXX(NR,JC+6)=7._DP*B(I)*B(I)*B(M)*B(M)+10._DP*R(M,I)*B(I)*B(M)**3
!
!
       QYY(NR,JC+1)=60._DP*(C(I)*C(I)+2._DP*R(M,I)*C(M)*C(I))
       QYY(NR,JC+2)=-(-1._DP)**IPER*(36._DP*C(I)*C(I)*C(M)+60._DP*R(M,I)*&
       &C(M)*C(M)*C(I))
       QYY(NR,JC+3)=12._DP*C(I)*TWOD+(-1._DP)**IPER*(36._DP*C(I)*C(I)*B(M)+60._DP&
       &*R(M,I)*C(M)*C(I)*B(M))
       QYY(NR,JC+4)=7._DP*C(I)*C(I)*C(M)*C(M)+10._DP*R(M,I)*C(I)*C(M)**3
       QYY(NR,JC+5)=-10._DP*C(I)*C(I)*B(M)*C(M)-4._DP*C(M)*C(M)*B(I)*C(I)-&
       &20._DP*R(M,I)*C(M)*C(M)*C(I)*B(M)
       QYY(NR,JC+6)=3._DP*C(I)*C(I)*B(M)*B(M)+4._DP*C(I)*C(M)*B(I)*B(M)+&
       &10._DP*R(M,I)*C(I)*C(M)*B(M)*B(M)
!
!
       QXY(NR,JC+1)=120._DP*(B(I)*C(I)+R(M,I)*P(J))
       QXY(NR,JC+2)=12._DP*C(I)*TWOD-(-1._DP)**IPER*(72._DP*B(I)*C(I)*C(M)+&
       &60._DP*R(M,I)*C(M)*P(J))
       QXY(NR,JC+3)=12._DP*B(I)*TWOD+(-1._DP)**IPER*(72._DP*C(I)*B(I)*B(M)+60._DP*&
       &R(M,I)*B(M)*P(J))
       QXY(NR,JC+4)=10._DP*C(I)*B(I)*C(M)*C(M)+4._DP*C(I)*C(I)*B(M)*C(M)+&
       &10._DP*R(M,I)*C(M)*C(M)*P(J)
       QXY(NR,JC+5)=-12._DP*B(I)*C(I)*B(M)*C(M)-4._DP*P(J)*P(J)-20._DP*R(M,I)*&
       &B(M)*C(M)*P(J)
       QXY(NR,JC+6)=10._DP*B(I)*C(I)*B(M)*B(M)+4._DP*B(I)*B(I)*C(M)*B(M)+&
       &10._DP*R(M,I)*B(M)*B(M)*P(J)
!
!
      case(3)
       QXX(NR,JC+1)=60._DP*R(M,I)*B(I)*B(I)
       QXX(NR,JC+2)=-(-1._DP)**IPER*(6._DP*B(I)*B(I)*C(I)+30._DP*R(M,I)*B(I)*&
       &B(I)*C(M))
       QXX(NR,JC+3)=(-1._DP)**IPER*(6._DP*B(I)*B(I)*B(I)+30._DP*R(M,I)*B(I)*&
       &B(I)*B(M))
       QXX(NR,JC+4)=2._DP*B(I)*B(I)*C(I)*C(M)+5._DP*R(M,I)*B(I)*B(I)*&
       &C(M)*C(M)
       QXX(NR,JC+5)=-2._DP*B(I)*B(I)*(P(J)+5._DP*R(M,I)*B(M)*C(M))
       QXX(NR,JC+6)=2._DP*B(I)*B(I)*B(I)*B(M)+5._DP*R(M,I)*B(I)*B(I)*B(M)*B(M)
!
!
```

```fortran
     QYY(NR,JC+1)=60._DP*R(M,I)*C(I)*C(I)
     QYY(NR,JC+2)=-(-1._DP)**IPER*(6._DP*C(I)**3+30._DP*R(M,I)*C(I)*C(I)*C(M))
     QYY(NR,JC+3)=(-1._DP)**IPER*(6._DP*C(I)*C(I)*B(I)+30._DP*R(M,I)*C(I)*&
     &C(I)*B(M))
     QYY(NR,JC+4)=2._DP*C(I)*C(I)*C(I)*C(M)+5._DP*R(M,I)*C(I)*C(I)*C(M)*&
     &C(M)
     QYY(NR,JC+5)=-2._DP*C(I)*C(I)*(P(J)+5._DP*R(M,I)*C(M)*B(M))
     QYY(NR,JC+6)=2._DP*C(I)*C(I)*B(I)*B(M)+5._DP*R(M,I)*C(I)*C(I)*B(M)*&
     &B(M)
!
!
     QXY(NR,JC+1)=120._DP*R(M,I)*B(I)*C(I)
     QXY(NR,JC+2)=-(-1._DP)**IPER*(12._DP*B(I)*C(I)*C(I)+60._DP*R(M,I)*B(I)*&
     &C(I)*C(M))
     QXY(NR,JC+3)=(-1._DP)**IPER*(12._DP*C(I)*B(I)*B(I)+60._DP*R(M,I)*C(I)*&
     &B(I)*B(M))
     QXY(NR,JC+4)=4._DP*C(I)*C(I)*B(I)*C(M)+10._DP*R(M,I)*C(M)*C(M)*B(I)*&
     &C(I)
     QXY(NR,JC+5)=-4._DP*B(I)*C(I)*P(J)-20._DP*R(M,I)*B(I)*C(I)*B(M)*C(M)
     QXY(NR,JC+6)=4._DP*B(I)*B(I)*C(I)*B(M)+10._DP*R(M,I)*B(M)*B(M)*C(I)*&
     &B(I)
    case default
     istat=STAT_FAILURE
     emsg='K is diff. from 1,2 or 3, Qform, &
     & element_module'
     QXX=ZERO; QYY=ZERO; QXY=ZERO
     return
    end select
   end do iper_loop
  end do row_selec_loop

 end do main_loop



end subroutine Qform

end module Qform_env
```

Appendix C

TUBA3 verification: meshes and boundary conditions

The plate analyses were performed using either some or all the meshes shown in Figures C.1, C.2 and C.3. Edge numbers are used in Tables C.1, C.2, C.3 and C.4 to specify the constrained degrees of freedom.

In case of a free or simply supported edge, no moments work for rotations around the edge axis. If this is oriented respectively in the x and y directions and the plate is isotropic, the followings must hold

$$M_y = \frac{E\,t^3}{12(1-\nu^2)}\left(\nu\,\frac{\partial^2 w}{\partial x^2} + \frac{\partial^2 w}{\partial y^2}\right) = 0 \tag{C.1}$$

$$M_x = \frac{E\,t^3}{12(1-\nu^2)}\left(\frac{\partial^2 w}{\partial x^2} + \nu\,\frac{\partial^2 w}{\partial y^2}\right) = 0 \tag{C.2}$$

which reduce to

$$\nu\,\frac{\partial^2 w}{\partial x^2} + \frac{\partial^2 w}{\partial y^2} = 0 \tag{C.3}$$

$$\frac{\partial^2 w}{\partial x^2} + \nu\,\frac{\partial^2 w}{\partial y^2} = 0 \tag{C.4}$$

For a UD composite plate, the analogous conditions are

$$\nu_{xy}\,\frac{\partial^2 w}{\partial x^2} + \frac{\partial^2 w}{\partial y^2} = 0 \tag{C.5}$$

$$\frac{\partial^2 w}{\partial x^2} + \nu_{yx}\,\frac{\partial^2 w}{\partial y^2} = 0 \tag{C.6}$$

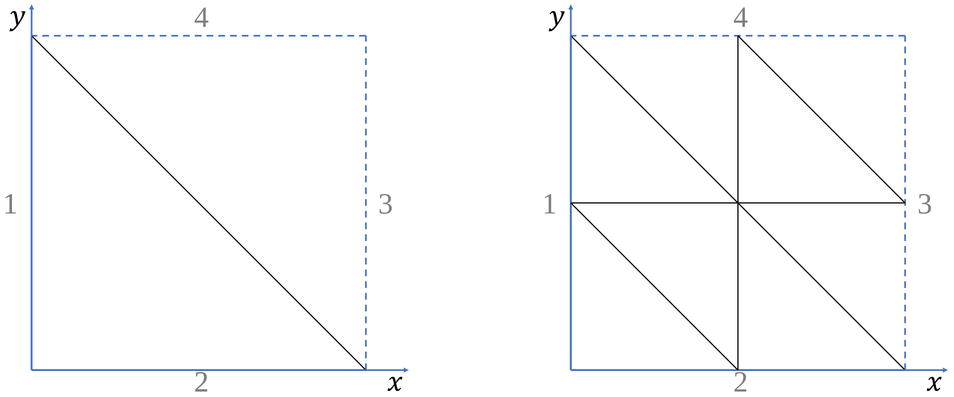

(a) A1 **(b)** A2

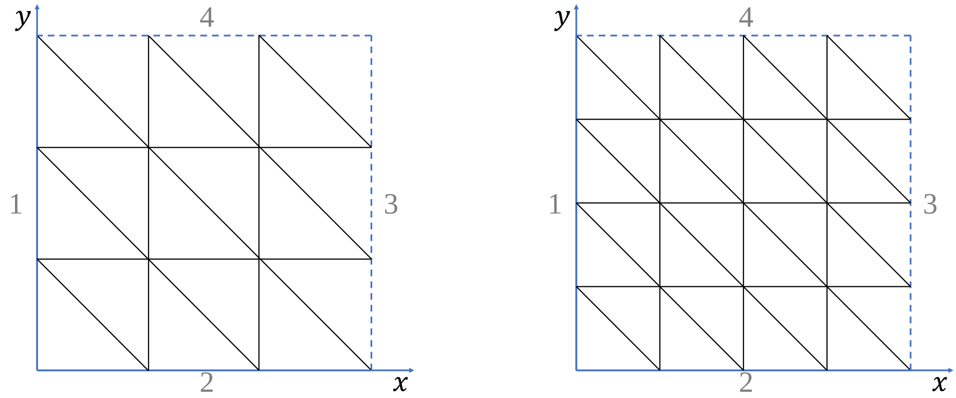

(c) A3 **(d)** A4

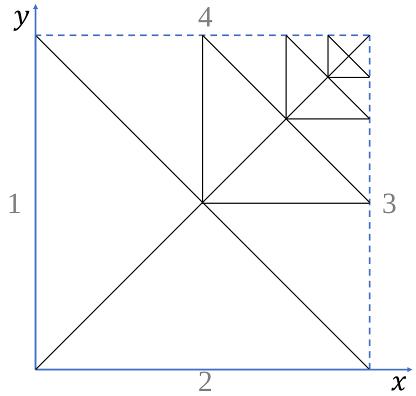

(e) B1

Figure C.1: Isotropic plate: meshes.

Edge	Type	Boundary conditions
1	simply supported	$w = 0,\ \frac{\partial w}{\partial y} = 0$ $\frac{\partial^2 w}{\partial x^2} + \nu\,\frac{\partial^2 w}{\partial y^2} = 0$
2	simply supported	$w = 0,\ \frac{\partial w}{\partial x} = 0$ $\nu\,\frac{\partial^2 w}{\partial x^2} + \frac{\partial^2 w}{\partial y^2} = 0$
3	y-symmetry	$\frac{\partial w}{\partial x} = 0,\ \frac{\partial^2 w}{\partial x \partial y} = 0$
4	x-symmetry	$\frac{\partial w}{\partial y} = 0,\ \frac{\partial^2 w}{\partial x \partial y} = 0$

Table C.1: Boundary conditions for the simply supported isotropic plate.

Edge	Type	Boundary conditions
1	clamped	$w = 0,\ \frac{\partial w}{\partial y} = 0,\ \frac{\partial w}{\partial x} = 0$
2	clamped	$w = 0,\ \frac{\partial w}{\partial x} = 0,\ \frac{\partial w}{\partial y} = 0$
3	y-symmetry	$\frac{\partial w}{\partial x} = 0,\ \frac{\partial^2 w}{\partial x \partial y} = 0$
4	x-symmetry	$\frac{\partial w}{\partial y} = 0,\ \frac{\partial^2 w}{\partial x \partial y} = 0$

Table C.2: Boundary conditions for the clamped isotropic plate.

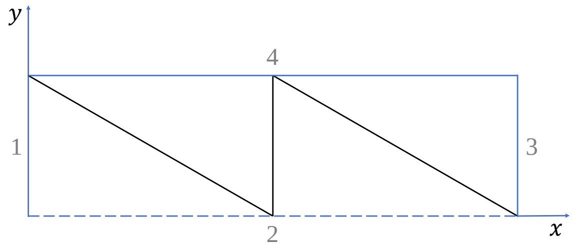

(a) A1

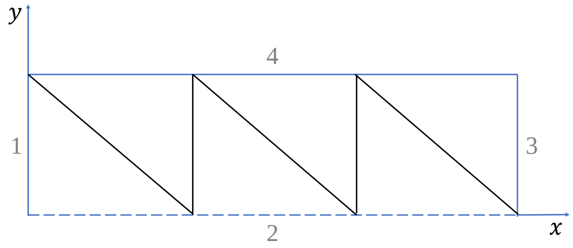

(b) A2

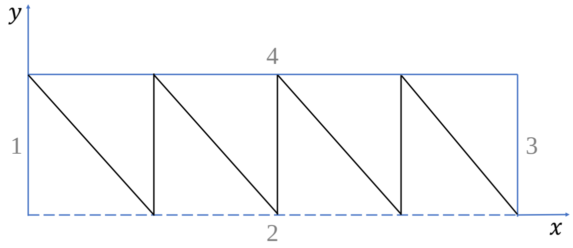

(c) A3

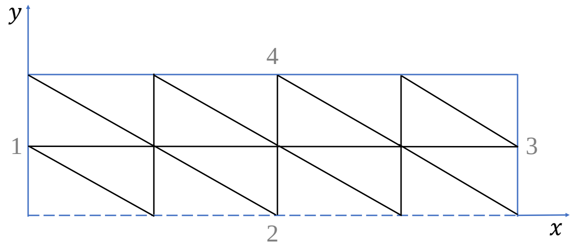

(d) A4

Figure C.2: Cantilever UD composite plate: meshes.

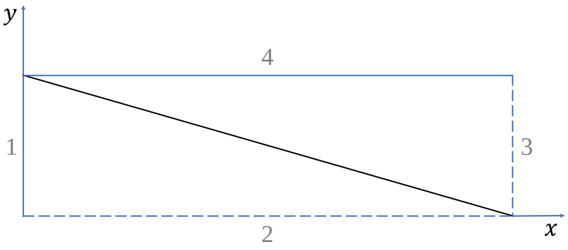

(a) A1

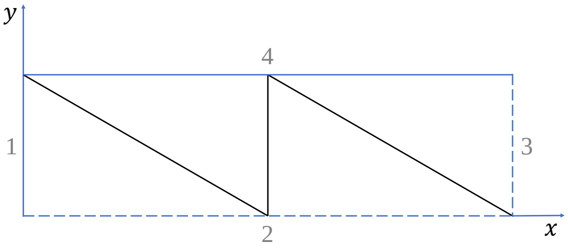

(b) A2

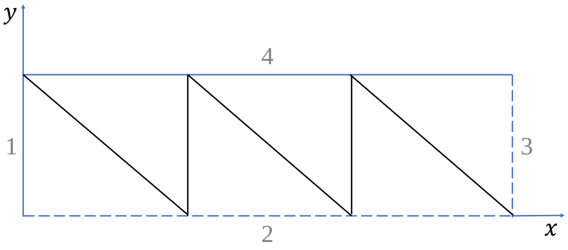

(c) A3

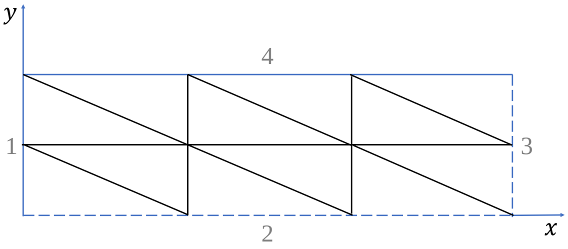

(d) A4

Figure C.3: 3-point-bending UD composite plate: meshes.

Edge	Type	Boundary conditions
1	clamped	$w = 0,\ \frac{\partial w}{\partial y} = 0,\ \frac{\partial w}{\partial y} = 0$
2	x-symmetry	$\frac{\partial w}{\partial y} = 0,\ \frac{\partial^2 w}{\partial x \partial y} = 0$
3	free	$\frac{\partial^2 w}{\partial x^2} + \nu_{yx}\,\frac{\partial^2 w}{\partial y^2} = 0$
4	free	$\nu_{xy}\,\frac{\partial^2 w}{\partial x^2} + \frac{\partial^2 w}{\partial y^2} = 0$

Table C.3: Boundary conditions for the cantilever UD composite plate.

Edge	Type	Boundary conditions
1	simply supported	$w = 0,\ \frac{\partial w}{\partial y} = 0$ $\frac{\partial^2 w}{\partial x^2} + \nu_{yx}\,\frac{\partial^2 w}{\partial y^2} = 0$
2	x-symmetry	$\frac{\partial w}{\partial y} = 0,\ \frac{\partial^2 w}{\partial x \partial y} = 0$
3	y-symmetry	$\frac{\partial w}{\partial x} = 0,\ \frac{\partial^2 w}{\partial x \partial y} = 0$
4	free	$\nu_{xy}\,\frac{\partial^2 w}{\partial x^2} + \frac{\partial^2 w}{\partial y^2} = 0$

Table C.4: Boundary conditions for the 3-point-bending UD composite plate.

Appendix D

Abaqus input file parameters for DCB reference analyses

Following, an excerpt of an Abaqus input file is reported, used for reference analyses with C3D8I elements and cohesive contact. Parameters for the definition of material, interaction, step and solution control are made available.

```
*Heading
** Job name: BenchmarkDCB_JOB_M3 Model name: BenchmarkDCB
** Generated by: Abaqus/CAE 2017
*Preprint, echo=NO, model=NO, history=NO, contact=NO
**
** PARTS
**
*Part, name=BottomPart
...
...
...
**
** MATERIALS
**
*Material, name=CompositeUD
*Elastic, type=ENGINEERING CONSTANTS
139400.,10160.,10160.,   0.3,   0.3, 0.436, 4600., 4600.
 3540.,
**
** INTERACTION PROPERTIES
**
```

```
*Surface Interaction, name=CohesiveContact
1.,
*Cohesive Behavior
169333., 76666.7, 76666.7
*Damage Initiation, criterion=QUADS
30.,50.,50.
*Damage Evolution, type=ENERGY, mixed mode behavior=BK, power=1.62
 0.17, 0.494, 0.494
*Damage Stabilization
1.772e-05
**
** BOUNDARY CONDITIONS
**
** Name: Fixed_BottomLeftCorner Type: Symmetry/Antisymmetry/Encastre
*Boundary
BottomLeftCorner, PINNED
** Name: XYPlanar_TopLeftCorner Type: Displacement/Rotation
*Boundary
Set-2, 1, 1
Set-2, 2, 2
**
** INTERACTIONS
**
** Interaction: Contact
*Contact
*Contact Inclusions
BottomPart-1.BottomPart_TopSurf , TopPart-1.TopPart_BottomSurf
*Contact Property Assignment
 ,  , CohesiveContact
** ----------------------------------------------------------------
**
** STEP: Loading
**
*Step, name=Loading, nlgeom=NO, extrapolation=NO, inc=1000
*Static
1e-2, 2., 1e-07, 1e-2
**
** BOUNDARY CONDITIONS
**
** Name: UpwVelocity_TopLeft Type: Velocity/Angular velocity
*Boundary, type=VELOCITY
_PickedSet8, 3, 3, 2.
**
** CONTROLS
**
*Controls, reset
*Controls, parameters=time incrementation
```

```
, , , , , , , 10, , ,
**
** OUTPUT REQUESTS
**
*Restart, write, frequency=0
...
...
...
*End Step
```

Appendix E

Analytical solution for mode I delamination

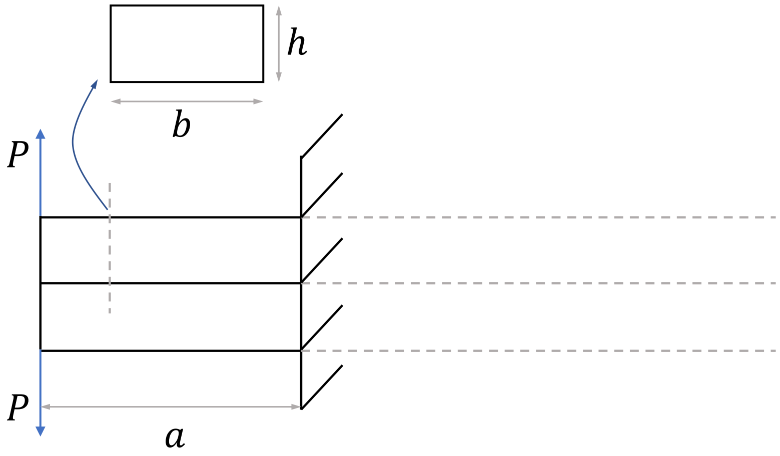

Figure E.1: Double cantilever beam with precrack length a

The analytical solution for DCB delamination is composed of two distinguished curves corresponding to initial linear loading and crack propagation. In both cases a system of two cantilever beams is considered, having length equal to the crack extension a, width b and thickness h (Figure E.1).

The first branch of the curve considers $a = a_0$, hence the beams are as long as the precrack. The tip separation Δ_I can be described by the Corrected Beam Theory (CBT) [81], which is an extension of the Euler-Bernoulli model that accounts for transverse shearing and rotations at the crack tip.

$$\Delta_I = \frac{2P(a + \chi h)^3}{3E_{xx}I} \tag{E.1}$$

where P is the tip force, E_{xx} the longitudinal modulus and I the section's moment of inertia. The correction parameter χ reads

$$\chi = \sqrt{\frac{E_{xx}}{11G_{xz}}\left[3 - 2\left(\frac{\Gamma}{1+\Gamma}\right)^2\right]} \tag{E.2}$$

with G_{xz} the transverse shear modulus and

$$\Gamma = 1.18\frac{\sqrt{E_{xx}E_{yy}}}{G_{xz}} \tag{E.3}$$

Propagation occurs when the energy release rate reaches the mode I fracture toughness, hence when

$$G_I = G_{I,c} \tag{E.4}$$

Following [82], the mode I energy release rate is expressed as

$$G_I = \frac{P}{2b}\frac{\partial \Delta_I}{\partial a}\bigg|_{P=const} \tag{E.5}$$

Thus, differentiating Equation (E.1) by a and combining Equations (E.4) and (E.5), the crack length can be expressed as function of the applied load P as

$$a = \frac{\sqrt{b\,E_{xx}I\,G_{I,c}}}{P} - \chi h \tag{E.6}$$

Substituting Equation (E.6) into Equation (E.1), the mode I opening during crack propagation is found as

$$\Delta_I = \frac{2\sqrt{b^3E_{xx}I\,G_{I,c}^3}}{3P^2} \tag{E.7}$$

Equations (E.1) and (E.7) are ultimately the analytical solutions for the DCB specimen loading and fracture.